

**SOLUTION OF ELECTROMAGNETIC SCATTERING  
PROBLEMS INVOLVING CURVED SURFACES**

**A THESIS**

**SUBMITTED TO THE DEPARTMENT OF ELECTRICAL AND  
ELECTRONICS ENGINEERING  
AND THE INSTITUTE OF ENGINEERING AND SCIENCES  
OF BILKENT UNIVERSITY  
IN PARTIAL FULFILLMENT OF THE REQUIREMENTS  
FOR THE DEGREE OF  
MASTER OF SCIENCE**

**By**

**Kubilay Sertel**

**June 1997**

THESIS  
QC  
665  
.53  
S47  
1997

SOLUTION OF ELECTROMAGNETIC SCATTERING  
PROBLEMS INVOLVING CURVED SURFACES

A THESIS

SUBMITTED TO THE DEPARTMENT OF ELECTRICAL AND  
ELECTRONICS ENGINEERING

AND THE INSTITUTE OF ENGINEERING AND SCIENCES  
OF BILKENT UNIVERSITY

IN PARTIAL FULFILLMENT OF THE REQUIREMENTS  
FOR THE DEGREE OF  
MASTER OF SCIENCE

*Kubilay Sertel.*

*isr@fenix.bogaziciuni.edu.tr*

By

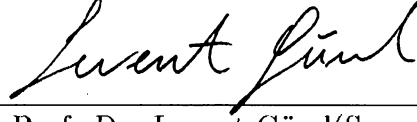
Kubilay Sertel

June 1997

QC  
665  
.S3  
.G47  
1937

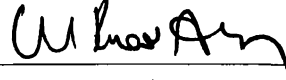
8038252

I certify that I have read this thesis and that in my opinion it is fully adequate,  
in scope and in quality, as a thesis for the degree of Master of Science.



Asst. Prof. Dr. Levent Gürel(Supervisor)

I certify that I have read this thesis and that in my opinion it is fully adequate,  
in scope and in quality, as a thesis for the degree of Master of Science.



Assoc. Prof. Dr. M. İrşadi Aksun

I certify that I have read this thesis and that in my opinion it is fully adequate,  
in scope and in quality, as a thesis for the degree of Master of Science.



Prof. Dr. Ayhan Altıntaş

Approved for the Institute of Engineering and Sciences:



Prof. Dr. Mehmet Baray  
Director of Institute of Engineering and Sciences

## ABSTRACT

# SOLUTION OF ELECTROMAGNETIC SCATTERING PROBLEMS INVOLVING CURVED SURFACES

Kubilay Sertel

M.S. in Electrical and Electronics Engineering

Supervisor: Asst. Prof. Dr. Levent Gürel

June 1997

The method of moments (MoM) is an efficient technique for the solution of electromagnetic scattering problems. Problems encountered in real-life applications are often three dimensional and involve electrically large scatterers with complicated geometries. When the MoM is employed for the solution of these problems, the size of the resulting matrix equation is usually large. It is possible to reduce the size of the system of equations by improving the geometry modeling technique in the MoM algorithm. Another way of improving the efficiency of the MoM is the fast multipole method (FMM). The FMM reduces the computational complexity of the conventional MoM. The FMM has also lower memory-requirement complexity than the MoM. This facilitates the solution of larger problems on a given hardware in a shorter period of time. The combination of the FMM and the higher-order geometry modeling techniques is proposed for the efficient solution of large electromagnetic scattering problems involving three-dimensional, arbitrarily shaped, conducting surface scatterers.

## ÖZET

### EĞRİ YÜZEYLER İÇEREN ELEKTROMANYETİK SAÇINIM PROBLEMLERİNİN ÇÖZÜMÜ

Kubilay Sertel

Elektrik ve Elektronik Mühendisliği Bölümü Yüksek Lisans

Tez Yöneticisi: Y. Doç. Dr. Levent Gürel

Haziran 1997

Moment metodu (MoM) elektromanyetik saçınım problemlerinin çözümü için etkili bir yöntemdir. Günlük hayatta karşılaşılan saçınım problemleri çoğunlukla üç boyutludurlar ve elektriksel olarak büyük, karmaşık geometrili saçıcılar içerirler. Bu problemlerin çözümünde MoM kullanıldığında elde edilen matrisin boyutu genellikle büyüktür. Bu denklem sisteminin boyutunu MoM algoritmasındaki geometri modellemesini iyileştirerek düşürmek mümkündür. MoM'un etkinliğini arttırmanın başka bir yolu da hızlı multipol metodudur (FMM). FMM bildik MoM'un işlemsel karmaşıklığını düşürür. FMM için gereken bellek miktarının karmaşıklığı da MoM için gerekenden düşüktür. Bu, verilen bir donanım üzerinde daha büyük boyutlu problemlerin daha kısa zamanda çözülebilmesini olanaklı kılar. FMM ve yüksek dereceli geometri modelleme tekniklerinin birleştirilmesi üç boyutlu, rastgele şekilli, iletken yüzey saçıcılarının bulunduğu büyük elektromanyetik problemlerinin etkili çözümü için önerilmiştir.

## ACKNOWLEDGMENTS

I would like to express my deepest gratitude to my supervisor Asst. Prof. Dr. Levent Gürel for his guidance, suggestions, and invaluable encouragement throughout the development of this thesis. I would like to thank to Assoc. Prof. Dr. M. İrşadi Aksun and Prof. Dr. Ayhan Altıntaş for reading and commenting on my thesis.

Special thanks go to İ. Kürşat Şendur for his invaluable discussions and help in every step of this thesis. I would also like to thank to him, to Ertem Tuncel and to Uğur Oğuz for sharing hard times, day and night, in the office.

# TABLE OF CONTENTS

|          |  |           |
|----------|--|-----------|
| <b>1</b> | <b>Introduction</b>                                    | <b>1</b>  |
| <b>2</b> | <b>MoM and FMM</b>                                     | <b>4</b>  |
| 2.1      | The Electric-Field Integral Equation                   | 5         |
| 2.2      | Method of Moments                                      | 6         |
| 2.3      | Multipole Expansions and FMM Formulation               | 9         |
| 2.3.1    | Formulations for the FMM . . . . .                     | 11        |
| 2.3.2    | Description of the FMM Algorithm . . . . .             | 12        |
| 2.3.3    | Required Number of Multipoles and Directions . . . . . | 15        |
| 2.3.4    | Memory Requirements and Computational Complexity .     | 16        |
| <b>3</b> | <b>Geometry-Modeling Techniques</b>                    | <b>18</b> |
| 3.1      | Parametric Space Curves . . . . .                      | 19        |
| 3.2      | Exact Parametric Models . . . . .                      | 23        |



|          |  |           |
|----------|--|-----------|
| 3.3      | Polynomial Interpolation Surfaces . . . . .              | 23        |
| 3.3.1    | Staircase Approximation . . . . .                        | 23        |
| 3.3.2    | Flat Triangulations . . . . .                            | 24        |
| 3.3.3    | Quadratic Triangulations . . . . .                       | 25        |
| 3.3.4    | Biquadratic Approximations . . . . .                     | 26        |
| 3.4      | Free-Form Surfaces . . . . .                             | 27        |
| 3.4.1    | Bézier Patches . . . . .                                 | 28        |
| 3.4.2    | B-spline Surfaces . . . . .                              | 30        |
| 3.4.3    | Nonuniform Rational B-Spline (NURBS) Surfaces . . . . .  | 32        |
| <b>4</b> | <b>Basis Functions</b>                                   | <b>34</b> |
| 4.1      | Rooftop (RT) Basis Functions . . . . .                   | 35        |
| 4.2      | Rao-Wilton-Glisson (RWG) Basis Functions . . . . .       | 36        |
| 4.3      | Curved Rooftop (CRT) Basis Functions . . . . .           | 36        |
| 4.4      | Curved RWG (CRWG) Basis Functions . . . . .              | 41        |
| 4.5      | First-Order RT Basis Functions . . . . .                 | 44        |
| <b>5</b> | <b>Scattering from Canonical and Complicated Targets</b> | <b>47</b> |
| 5.1      | Flat Patch . . . . .                                     | 48        |

|          |   |            |
|----------|---|------------|
| 5.2      | Sphere . . . . .  | 69         |
| 5.2.1    | Flat Triangulation with RWG BFs . . . . .                 | 70         |
| 5.2.2    | Exact Model with CRWG BFs . . . . .                       | 71         |
| 5.2.3    | Exact Model with CRT BFs . . . . .                        | 74         |
| 5.2.4    | Quadratic Triangulation with CRWG BFs . . . . .           | 77         |
| 5.2.5    | Bezier-Patch Model with CRT BFs . . . . .                 | 83         |
| 5.2.6    | Comparison of Different Modeling Schemes . . . . .        | 86         |
| 5.3      | Missile . . . . .   | 94         |
| <b>6</b> | <b>Conclusions</b>  | <b>100</b> |
| <b>A</b> | <b>Evaluation of the MoM Matrix Elements</b>              | <b>103</b> |
| A.1      | Singular Integrals Appearing in the Formulation . . . . . | 104        |
| A.2      | Techniques to Annihilate the Singularity . . . . .        | 107        |
| A.2.1    | For Triangular Subdomains . . . . .                       | 108        |
| A.2.2    | For Square Subdomains . . . . .                           | 114        |
| A.3      | Numerical Integration . . . . .                           | 122        |

## LIST OF FIGURES

|     |  |    |
|-----|--|----|
| 2.1 | The basic geometry illustrating the relationship between $\mathbf{x}, \mathbf{x}'$ , $r$ , and $d$ . . . . .                                   | 10 |
| 2.2 | The geometry construction used in FMM formulations, illustrating the relation between source point, field point and the group centers. . . . . | 11 |
| 2.3 | Illustration of the FMM strategy. . . . .  | 14 |
| 3.1 | A parametric space curve is a vector function of a parameter $u$ . . . . .   | 19 |
| 3.2 | A generic Bézier curve and its defining polygon. . . . .   | 21 |
| 3.3 | An aircraft approximated by a mesh of rectangular cells. (Reproduced from [18].) . . . . .   | 24 |
| 3.4 | Sphere approximated by a mesh of flat triangles. The triangulation is performed by MSC/ARIES. . . . .  | 25 |
| 3.5 | Sphere approximated by a mesh of 6-point quadratic triangles. The triangulation is performed by MSC/ARIES. . . . .                             | 26 |

|     |  |    |
|-----|--|----|
| 3.6 | Sphere approximated by a mesh of 9-point biquadratic rectangular patches. Reproduced from . . . . .  | 27 |
| 3.7 | Tensor product Bézier surface and its defining polygon net. . . .  | 30 |
| 3.8 | A yacht hull defined as a B-spline surface, the defining polygon net and the parametric representation. (Reproduced from [16].)  | 31 |
| 3.9 | Sphere generated as a rational B-spline surface. (a) Offset circle and defining polygon; (b) circle of revolution and defining polygon; (c) defining polygon net and sphere. (Reproduced from [16].) | 33 |
| 4.1 | Rooftop basis function defined a pair of flat rectangular regions.   | 35 |
| 4.2 | Rao–Wilton–Glisson basis function on a pair of flat triangular regions.  | 36 |
| 4.3 | Composite mapping of the parametric unit square on the real curved surface.  | 38 |
| 4.4 | C-RT BF defined on the parametric space. . . . .   | 39 |
| 4.5 | CRWG BF defined on the unit triangle in the parametric space.  | 42 |
| 4.6 | First-order rooftop basis functions defined on the $(u, v)$ parametric space.  | 45 |
| 5.1 | Flat PEC patch illuminated by a plane wave.  | 49 |
| 5.2 | Discretization of the flat patch.  | 50 |

|     |  |    |
|-----|--|----|
| 5.3 | The induced current and charge densities on the flat patch. The patch is discretized into $10 \times 10$ divisions and the RT BFs on the internal edges are used for the expansion. (a) Magnitude of the copolar induced current. (b) Magnitude of the crosspolar current. (c) Real part of the divergence of the induced current. (d) Imaginary part of the divergence of the induced current. The current results are normalized with the magnitude of the incident magnetic field, and the divergence of the current is presented as the charge distribution. . . . . | 51 |
| 5.4 | The induced current and charge densities on the flat patch. The patch is triangulated into 200 subdomains and the RWG BFs on the internal edges are used for the expansion. (a) Magnitude of the copolar induced current. (b) Magnitude of the crosspolar current. (c) Real part of the divergence of the induced current. (d) Imaginary part of the divergence of the induced current. The current results are normalized with the magnitude of the incident magnetic field, and the divergence of the current is presented as the charge distribution. . . . .         | 53 |

|     |   |    |
|-----|---|----|
| 5.5 | <p>The induced current and charge densities on the flat patch. The patch is discretized into <math>20 \times 20</math> divisions and the RT BFs on the internal edges are used for the expansion. (a) Magnitude of the copolar induced current. (b) Magnitude of the crosspolar current. (c) Real part of the divergence of the induced current. (d) Imaginary part of the divergence of the induced current. The current results are normalized with the magnitude of the incident magnetic field, and the divergence of the current is presented as the charge distribution. . . . .</p>  | 54 |
| 5.6 | <p>The induced current and charge densities on the flat patch. The patch is discretized into <math>10 \times 10</math> divisions and two LinRT BFs on the internal edges are used for the expansion. Transverse continuity is imposed at each internal vertex. (a) Magnitude of the copolar induced current. (b) Magnitude of the crosspolar current. (c) Real part of the divergence of the induced current. (d) Imaginary part of the divergence of the induced current. The current results are normalized with the magnitude of the incident magnetic field, and the divergence of the current is presented as the charge distribution. . . . .</p> | 56 |

|     |   |    |
|-----|---|----|
| 5.7 | The induced current and charge densities on the flat patch. The patch is discretized into $20 \times 20$ divisions and two LinRT BFs on the internal edges are used for the expansion. Transverse continuity is imposed at each internal vertex. (a) Magnitude of the copolar induced current. (b) Magnitude of the crosspolar current. (c) Real part of the divergence of the induced current. (d) Imaginary part of the divergence of the induced current. The current results are normalized with the magnitude of the incident magnetic field, and the divergence of the current is presented as the charge distribution. . . . . | 57 |
| 5.8 | The induced current and charge densities on the flat patch. The patch is discretized into $10 \times 10$ divisions and two LinRT BFs on the internal edges are used for the expansion. (a) Magnitude of the copolar induced current. (b) Magnitude of the crosspolar current. (c) Real part of the divergence of the induced current. (d) Imaginary part of the divergence of the induced current. The current results are normalized with the magnitude of the incident magnetic field, and the divergence of the current is presented as the charge distribution. . . . .   | 58 |

|      |   |    |
|------|---|----|
| 5.9  | The induced current and charge densities on the flat patch. The patch is discretized into $20 \times 20$ divisions and two LinRT BFs on the internal edges are used for the expansion. (a) Magnitude of the copolar induced current. (b) Magnitude of the crosspolar current. (c) Real part of the divergence of the induced current. (d) Imaginary part of the divergence of the induced current. The current results are normalized with the magnitude of the incident magnetic field, and the divergence of the current is presented as the charge distribution. . . . . | 59 |
| 5.10 | Boundary-condition error on the flat patch. The solution is obtained using the RT BFs. (a) Copolar BCE for $10 \times 10$ discretization. (b) Copolar BCE for $20 \times 20$ discretization. (c) Crosspolar BCE for $10 \times 10$ discretization. (d) Crosspolar BCE for $20 \times 20$ discretization. . . . .  | 60 |
| 5.11 | Boundary-condition error on the flat patch. The solution is obtained using the transversely continuous LinRT BFs. (a) Copolar BCE for $10 \times 10$ discretization. (b) Copolar BCE for $20 \times 20$ discretization. (c) Crosspolar BCE for $10 \times 10$ discretization. (d) Crosspolar BCE for $20 \times 20$ discretization. . . . .   | 61 |
| 5.12 | Boundary-condition error on the flat patch. The solution is obtained using the LinRT BFs. (a) Copolar BCE for $10 \times 10$ discretization. (b) Copolar BCE for $20 \times 20$ discretization. (c) Crosspolar BCE for $10 \times 10$ discretization. (d) Crosspolar BCE for $20 \times 20$ discretization.   | 62 |



|      |  |    |
|------|--|----|
| 5.13 | (a) Magnitude of the copolar induced current on a $\lambda \times \lambda$ flat patch. (b) Magnitude of the crosspolar induced current on a $\lambda \times \lambda$ flat patch. The color plots are generated using the MSC/ARIES.  | 65 |
| 5.14 | Bistatic RCS of a $2\lambda \times 2\lambda$ flat patch. — $15 \times 15$ division with 420 RT BFs, -- MSC/ARIES triangulation with 560 RWG BFs.   | 65 |
| 5.15 | Timing comparisons of the MoM and the FMM. (a) The matrix solution times using the MoM with LU decomposition, the MoM with CGS, and the FMM with CGS, (b) The problem solution times using the MoM with LU decomposition, the MoM with CGS, and the FMM with CGS . . . . .             | 66 |
| 5.16 | CPU time consumed per one iteration of MoM and FMM algorithms. The iterative solution method is CGS.   | 66 |
| 5.17 | Approximate memory requirements of the MoM and the FMM algorithms.   | 67 |
| 5.18 | Validations of the FMM solutions. (a) Bistatic RCS of a $2\lambda \times 2\lambda$ flat patch using 736 CRWG BFs, — the MoM solution, -- the FMM solution. (b) Bistatic RCS of a $2\lambda \times 2\lambda$ flat patch using 760 CRT BFs, — the MoM solution, -- the FMM solution. . . | 67 |
| 5.19 | Bistatic RCS of a $10\lambda \times 10\lambda$ flat patch. — $65 \times 65$ division with 8320 RT BFs, -- MSC/ARIES triangulation with 8008 RWG BFs. . . . .   | 68 |
| 5.20 | A PEC sphere illuminated by a plane wave.  | 70 |

|      |  |    |
|------|--|----|
| 5.21 | Flat triangulation of the sphere. . . . .  | 71 |
| 5.22 | Magnitude of the surface current induced on the $0.2\lambda$ -radius sphere. Flat triangulation of the sphere is used with the flat RWG basis functions. The results are normalized with the magnitude of incident magnetic field and are given on the three principle cuts of the sphere for different discretizations and different numbers of unknowns. — Mie series, $\cdots$ $7 \times 8$ divisions and 144 unknowns, $-\cdot-$ $9 \times 10$ divisions and 240 unknowns, $--$ $11 \times 16$ divisions and 480 unknowns. . . . . | 72 |
| 5.23 | Magnitude of the electric field scattered by the $0.2\lambda$ -radius sphere. Flat triangulation of the sphere is used with the flat RWG basis functions. The results are given on the three principle cuts of the sphere for different discretizations and different numbers of unknowns. — Mie series, $\cdots$ $7 \times 8$ divisions and 144 unknowns, $-\cdot-$ $9 \times 10$ divisions and 240 unknowns, $--$ $11 \times 16$ divisions and 480 unknowns. . . . .   | 73 |
| 5.24 | Magnitude of the surface current induced on the $0.2\lambda$ -radius sphere. Curved triangulation of the sphere is used with the CRWG basis functions. The results are normalized with the magnitude of incident magnetic field and are given on the three principle cuts of the sphere for different discretizations and different numbers of unknowns. — Mie series, $\cdots$ $7 \times 8$ divisions and 144 unknowns, $-\cdot-$ $9 \times 10$ divisions and 240 unknowns, $--$ $11 \times 16$ divisions and 480 unknowns. . . . .   | 75 |

|      |  |    |
|------|--|----|
| 5.25 | Magnitude of the electric field scattered by the $0.2\lambda$ -radius sphere. Curved triangulation of the sphere is used with the CRWG basis functions. The results are given on the three principle cuts of the sphere for different discretizations and different numbers of unknowns. — Mie series, $\cdots$ $7 \times 8$ divisions and 144 unknowns, $-\cdot-$ $9 \times 10$ divisions and 240 unknowns, $--$ $11 \times 16$ divisions and 480 unknowns. . . . .   | 76 |
| 5.26 | Rooftop basis and testing functions on the sphere. . . . .   | 77 |
| 5.27 | Magnitude of the surface current induced on the $0.2\lambda$ -radius sphere. Curved rectangular meshing of the sphere is used with the CRT basis functions. The results are normalized with the magnitude of incident magnetic field and are given on the three principle cuts of the sphere for different discretizations and different numbers of unknowns. — Mie series, $\cdots$ $5 \times 6$ divisions and 54 unknowns, $-\cdot-$ $7 \times 8$ divisions and 104 unknowns, $--$ $9 \times 18$ divisions and 306 unknowns. . . . . | 78 |
| 5.28 | Magnitude of the electric field scattered by the $0.2\lambda$ radius sphere. Curved rectangular meshing of the sphere is used with the CRT basis functions. The results are given on the three principle cuts of the sphere for different discretizations and different numbers of unknowns. — Mie series, $\cdots$ $5 \times 6$ divisions and 54 unknowns, $-\cdot-$ $7 \times 8$ divisions and 104 unknowns, $--$ $9 \times 18$ divisions and 306 unknowns. . . . .  | 79 |

|      |  |    |
|------|--|----|
| 5.29 | Magnitude of the induced surface current on a $0.2\lambda$ -radius sphere. The sphere is discretized using quadratic triangles and the EFIE is solved using the CRWG BFs defined on these triangular subdomains. The color plot was generated using the MSC/ARIES. . . . .   | 80 |
| 5.30 | Magnitude of the electric field scattered by the $0.2\lambda$ -radius sphere. Curved triangulation of the sphere, obtained from the MSC/ARIES, is used with the CRWG BFs. The results are given on the three principle cuts of the sphere. — Mie series, $\cdots$ 156 curved RWG BFs, $-\cdot-$ 318 curved RWG BFs. . . . .  | 81 |
| 5.31 | Magnitude of the electric field scattered by the $0.5\lambda$ -radius sphere. Curved triangulation of the sphere, obtained from the MSC/ARIES, is used with the CRWG basis functions. The results are given on the three principle cuts of the sphere. — Mie series, $\cdots$ 480 curved RWG BFs, $-\cdot-$ 831 curved RWG BFs, $---$ 1020 curved RWG BFs. . . . . | 82 |
| 5.32 | Magnitude of the electric field scattered by the $0.2\lambda$ -radius sphere. 8-patch Bézier model of the sphere is used with the CRT BFs. The results are given on the three principle cuts of the sphere. — Mie series, $\cdots$ 132 curved RT BFs, $-\cdot-$ 240 curved RT BFs. . . . .   | 84 |

|      |   |    |
|------|---|----|
| 5.33 | Magnitude of the electric field by scattered the $0.5\lambda$ -radius sphere. 8-patch Bézier model of the sphere is used with the CRT BFs. The results are given on the three principle cuts of the sphere. — Mie series, $\cdots$ 552 curved RT BFs, $-\cdot-$ 756 curved RT BFs, $-\cdot-$ 992 curved RT BFs. . . . .   | 85 |
| 5.34 | Magnitude of the surface current induced on the $0.5\lambda$ -radius sphere. Flat-triangulation, curved-triangulation, and curved-rectangular meshing of the sphere are used with the RWG, the CRWG, and the CRT BFs, respectively. The results are normalized with the magnitude of incident magnetic field and are given on the three principle cuts of the sphere. — Mie series, $\cdots$ $11 \times 16$ divisions and 660 flat RWG BFs. $-\cdot-$ $11 \times 16$ divisions and 660 curved RWG BFs, $--$ $11 \times 22$ divisions and 462 curved RT BFs. . . . . | 87 |
| 5.35 | Magnitude of the electric field scattered by the $0.5\lambda$ -radius sphere. Flat-triangulation, curved-triangulation, and curved-rectangular meshing of the sphere are used with the RWG, the CRWG, and CRT BFs respectively. The results are given on the three principle cuts of the sphere. — Mie series, $\cdots$ $11 \times 16$ divisions and 660 flat RWG BFs. $-\cdot-$ $11 \times 16$ divisions and 660 curved RWG BFs, $--$ $11 \times 22$ divisions and 462 curved RT BFs. . . . .  | 88 |

|      |   |    |
|------|---|----|
| 5.36 | Comparison of the different geometry models used in the computation of the magnitude of the electric field scattered by the $0.2\lambda$ -radius sphere. Curved triangulation of the sphere, obtained from the MSC/ARIES, is used with the CRWG BFs and the 8-patch Bézier model of the sphere is used with the CRT BFs. The results are given on the three principle cuts of the sphere. — Mie series, $\cdots$ 156 curved RWG BFs, $--$ 132 curved RT BFs.    | 90 |
| 5.37 | Comparison of the different geometry models used in the computation of the magnitude of the electric field scattered by the $0.5\lambda$ -radius sphere. Curved triangulation of the sphere, obtained from the MSC/ARIES is used with the CRWG BFs and 8-patch Bézier model of the sphere is used with the CRT BFs. The results are given on the three principle cuts of the sphere. — Mie series, $\cdots$ 480 curved RWG BFs. $--$ 552 curved RT BFs. . . . . | 91 |
| 5.38 | Maximum difference in the far-field solutions using different geometry models of the sphere. . . . .  | 92 |
| 5.39 | Norm of the difference in the far-field solutions using different geometry models of the sphere.  | 93 |
| 5.40 | Validations of the FMM solutions. (a) Bistatic RCS of a $0.5\lambda$ -radius sphere using 480 CRWG BFs, $--$ the MoM solution, $--$ the FMM solution, (b) Bistatic RCS of a $0.5\lambda$ radius sphere using 380 CRT BFs, $--$ the MoM solution, $--$ the FMM solution.   | 94 |
| 5.41 | Quadratic triangular mesh of the missile generated using the MSC/ARIES. . . . .   | 95 |

|      |   |    |
|------|---|----|
| 5.42 | Magnitude of the induced surface current on a 6-meter long missile at 100 MHz. The missile is discretized using quadratic triangles and the EFIE is solved using the CRWG BFs defined on these triangular subdomains. The color plot is generated using the MSC/ARIES. . . . .  | 96 |
| 5.43 | Comparison of the bistatic RCS of the 6-meter long missile at 100 MHz. Curved and flat triangulations of the missile, obtained from the MSC/ARIES, is used with the CRWG BFs and flat-RWG BFs respectively, and 34-patch Bézier model of the missile is used with the CRT BFs. The results are given on $x$ - $z$ plane, where the main wings of the missile are located. — 1053 flat-RWG BFs, — 1053 CRWG BFs, . . . 1088 CRT BFs. . . . . | 97 |
| 5.44 | Comparison of the bistatic RCS of the 6-meter long missile at 200 MHz. Curved and flat triangulation of the missile, obtained from the MSC/ARIES, is used with the CRWG BFs and flat-RWG BFs respectively, and 34-patch Bézier model of the missile is used with the CRT BFs. The results are given on $x$ - $z$ plane, where the main wings of the missile are located. — 2058 flat-RWG BFs, — 2058 CRWG BFs, . . . 2448 CRT BFs. . . . .  | 98 |

|   |     |
|---|-----|
| 5.45 Comparison of the bistatic RCS of the 6-meter long missile at 300 MHz. Curved and flat triangulation of the missile, obtained from the MSC/ARIES, is used with the CRWG BFs and flat-RWG BFs respectively, and 34-patch Bézier model of the missile is used with the CRT BFs. The results are given on $x$ - $z$ plane, where the main wings of the missile are located. — 7713 flat-RWG BFs, — 6213 CRWG BFs, ··· 4352 CRT BFs, . . . . . | 99  |
| A.1 Parametric mapping of the unit triangle to the curved triangle in real space. . . . .   | 109 |
| A.2 Subdivision of the parametric unit triangle for singularity annihilation. . . . .   | 110 |
| A.3 Mapping of sub-triangle 1. . . . .  | 110 |
| A.4 Mapping of sub-triangle 2. . . . .  | 110 |
| A.5 Mapping of sub-triangle 3. . . . .  | 111 |
| A.6 Mapping defined to annihilate the singularity at the origin. . . .  | 112 |
| A.7 Mapping of Method II. . . . .   | 113 |
| A.8 Mapping of the parametric unit square to a curved rectangular patch. . . . .  | 114 |
| A.9 Subdivision of the unit square into sub-triangles. . . . .  | 115 |
| A.10 Transformation applied on each parameter. . . . .  | 116 |



|   |     |
|---|-----|
| A.11 The subdivision of the unit square for Method III. . . . . | 118 |
| A.12 The transformation for the first subdomain. . . . .        | 118 |
| A.13 The subdivision of the unit square for Method IV. . . . .  | 121 |

**To My Family**

# Chapter 1

## Introduction

Solution techniques based on the surface integral equations (SIEs) are widely used in computational electromagnetics. Formulations employing SIEs express the unknown function on the defining surface of the problem geometry. Thus, both the surface and the unknown function defined on it have to be accurately represented in the solution algorithm.

Real-life electromagnetic scattering problems are often three dimensional and involve arbitrary geometries. Formulations of these problems can not be based on the arbitrary geometries of the problems, instead, the geometries are approximated by various mathematical models that are easier to work with. Approximating the problem geometry by polynomial subsections is becoming widely used in most of the numerical solution techniques, such as the finite element method (FEM) and the method of moments (MoM) [1, 2]. The MoM, which will be explained in detail in Chapter 2, provides a flexible and powerful formulation for the solution of electromagnetic scattering and

radiation problems.

Canonical geometries such as spherical, cylindrical, and conical surfaces can be exactly modeled. Arbitrarily curved surfaces can be accurately modeled using a mesh of biquadratic, bicubic, or higher-order polynomial surface patches. Non-uniform rational B-spline (NURBS) surfaces and Bézier<sup>1</sup> patches can also be used for the same purpose. NURBS surfaces are powerful modeling tools that are widely used in computer-aided graphical design (CAGD) applications. Hence, the representations of most bodies fabricated by using automated machining processes are based on NURBS meshes. Therefore, if the geometry of the scatterer is represented by NURBS surfaces in the electromagnetic scattering code, the output data of a CAGD tool can be directly used as the input of the code without inducing any geometry-modeling error in the solution.

In this thesis, a general formulation of the MoM for electromagnetic scattering problems involving arbitrarily shaped, conducting scatterers will be given. The limitations of this method will be mentioned and ways to overcome these limitations will be investigated.

The effect of using different techniques to approximate the problem geometry on the solution will be investigated. Comparisons of solutions different geometry-modeling techniques will be given. It will be shown that better geometry models improve the solution accuracy and reduce the size of the resulting matrix equation. Comparisons of results obtained using different basis functions in the MoM expansion will also be given, and it will be shown that the accuracy of the solution heavily depends on the geometry-modeling scheme rather than the type of the basis functions.

---

<sup>1</sup>Named after their inventor, Pierre Bézier.

The basis functions used in the expansion of the unknown function in the MoM formulations are defined to be conformal with the surface representation and are “curved” generalizations of the piecewise linear basis functions defined on flat rectangular domains (rooftops) [3, 2] and flat triangular domains (due to Rao, Wilton and Glisson) [1, 4]. Issues concerning the numerical computation of the singular and nonsingular integrals arising in the formulations using different surface representations and different basis functions will be addressed.

A general formulation of the fast multipole method (FMM) [5, 6, 7] for electromagnetic scattering problems will also be given. The performance of FMM will be investigated. Both the efficiency and the accuracy of the FMM will be demonstrated by comparing the FMM solutions to the MoM and closed-form solutions for some sample problems. Thus, the combination of the FMM and accurate geometry-modelling techniques will be proposed for the efficient solution of real-life electromagnetic scattering problems.

# Chapter 2

## MoM and FMM

The MoM is a well-known technique for obtaining approximate solutions of integral, differential, and integro-differential equations arising in various areas of basic and applied sciences [8]. The equation to be solved is converted into a matrix equation by applying the standard MoM procedure. The procedure is outlined in Section 2.2. This matrix equation is then solved either by Gaussian elimination (GE) or by an iterative solution scheme such as the conjugate gradient method (CGM). GE requires  $O(N^3)$  operations for the solution of an  $N \times N$  system. An iterative solver would require  $O(N^2)$  operations per iteration. As  $N$  gets larger, these high complexities limit the performance and applicability of the MoM.

For electromagnetic scattering and radiation problems, the FMM can be utilized to reduce the  $O(N^2)$  complexity of an iterative solver to  $O(N^{1.5})$ . This is accomplished by calculating the matrix-vector product in a fast and indirect way at iteration of the iterative solver. This chapter outlines the MoM and the

FMM as they are applied to electromagnetic scattering problems.

## 2.1 The Electric-Field Integral Equation

Based on Maxwell's equations, one way of formulating the electromagnetic scattering problems involving open or closed conducting surfaces is the so called electric-field-integral-equation (EFIE) formulation. Maxwell's equations in the frequency domain can be manipulated to obtain the a equation,

$$\nabla^2 \mathbf{E}(\mathbf{r}) + k^2 \mathbf{E}(\mathbf{r}) = -i\omega\mu \mathbf{J}(\mathbf{r}), \quad (2.1)$$

in free space with  $e^{i\omega t}$  time convention. The solution to this equation is given by

$$\mathbf{E}(\mathbf{r}) = -i\omega\mu \int_v dv' \overline{\mathbf{G}}(\mathbf{r}, \mathbf{r}') \cdot \mathbf{J}(\mathbf{r}'). \quad (2.2)$$

In the above,

$$\overline{\mathbf{G}}(\mathbf{r}, \mathbf{r}') = \left[ \overline{\mathbf{I}} - \frac{1}{k^2} \nabla \nabla \right] g(\mathbf{r}, \mathbf{r}') \quad (2.3)$$

is the dyadic Green's function and

$$g(\mathbf{r}, \mathbf{r}') = \frac{e^{ik|\mathbf{r}-\mathbf{r}'|}}{|\mathbf{r}-\mathbf{r}'|}. \quad (2.4)$$

is the scalar Green's function that satisfies the scalar wave equation

$$(\nabla^2 + k^2)g(\mathbf{r}, \mathbf{r}') = \delta(\mathbf{r} - \mathbf{r}'). \quad (2.5)$$

For a given source distribution  $\mathbf{J}(\mathbf{r})$ , the electric field radiated by that source distribution can be calculated using Eq. (2.2).

For conducting objects, the EFIE is given by

$$\hat{t} \cdot \int_s \left[ \mathbf{J}(\mathbf{r}') + \frac{1}{k^2} \nabla' \cdot \mathbf{J}(\mathbf{r}') \nabla \right] \frac{e^{ikR}}{R} ds' = \frac{4\pi i}{k\eta} \hat{t} \cdot \mathbf{E}^i(\mathbf{r}), \quad (2.6)$$

where

$$R = |\mathbf{r} - \mathbf{r}'|. \quad (2.7)$$

Equation 2.6 is the statement of the boundary condition on the tangential component of the electric field on a conducting surface. The vector denoted by  $\hat{t}$  is any unit tangent vector on the surface  $s$  of the scatterer, and  $\mathbf{E}^i(\mathbf{r})$  is an impressed field which excites the system.

## 2.2 Method of Moments

The EFIE for the unknown electric current density  $\mathbf{J}(\mathbf{r})$  on the conducting surface induced by an incident wave is discretized using the MoM technique. The induced surface current is approximated by a sum of  $N$  known basis functions  $\{\mathbf{j}_n(\mathbf{r})\}$  as

$$\mathbf{J}(\mathbf{r}) \approx \sum_{n=1}^N a_n \mathbf{j}_n(\mathbf{r}). \quad (2.8)$$

The EFIE thus becomes

$$\sum_{n=1}^N a_n \hat{t} \cdot \int_s \left[ \mathbf{j}_n(\mathbf{r}') + \frac{1}{k^2} \nabla' \cdot \mathbf{j}_n(\mathbf{r}') \nabla \right] \frac{e^{ikR}}{R} ds' - \frac{4\pi i}{k\eta} \hat{t} \cdot \mathbf{E}^i(\mathbf{r}) \approx 0 \quad (2.9)$$

Hence the problem is reduced to finding a set of  $a_n$ 's that minimizes the error in Eq. (2.9).

By defining a set of  $N$  weighting (also called “testing”) functions, the EFIE



is converted into a system of equations, whose solution minimizes the boundary-condition error in the average sense. The system of equations obtained is,

$$\sum_{n=1}^N Z_{mn} a_n = F_m, \quad m = 1, 2, \dots, N, \quad (2.10)$$

where

$$Z_{mn} = \int_s ds \mathbf{t}_m(\mathbf{r}) \cdot \int_{s'} ds' \left[ \mathbf{j}_n(\mathbf{r}') + \frac{1}{k^2} \nabla' \cdot \mathbf{j}_n(\mathbf{r}') \nabla \right] \frac{e^{ikR}}{R} \quad (2.11)$$

and

$$F_m = \frac{4\pi i}{k\eta} \int_s ds \mathbf{t}_m(\mathbf{r}) \cdot \mathbf{E}^i(\mathbf{r}). \quad (2.12)$$

Hence, the actual problem of finding the induced surface current  $\mathbf{J}(\mathbf{r})$  is reduced to finding  $N$  coefficients of expansion of Eq. (2.8) as the solution of Eq. (2.10).

The expansion functions should be chosen so that their combination in Eq. (2.8) is capable of representing the unknown current density  $\mathbf{J}(\mathbf{r})$  sufficiently well. Quite powerful basis functions (BFs) exist in the literature for the expansion of induced surface current in scattering problems, most common ones being the RWG<sup>1</sup> BFs supported on planar triangular subdomains [1] and rooftop (RT) BFs supported on planar rectangular subdomains [3]. For curved subdomains, generalizations of flat RWG BFs and flat RT BFs that are conformal with the curved surface they are defined on [2, 4] are used. The definitions of these basis functions will be given in Chapter 4. Entire-domain BFs are also used in the MoM formulations, but will not be mentioned here. It should be noted that the BFs chosen for the approximation of the current  $\mathbf{J}(\mathbf{r})$  should also be capable of providing a consistent approximation of the surface charge

---

<sup>1</sup>Named after Rao, Wilton and Glisson.

of providing a consistent approximation of the surface charge  $\rho(\mathbf{r})$ , which is related to the current through the continuity equation [9]

$$\nabla \cdot \mathbf{J}(\mathbf{r}) - i\omega\rho(\mathbf{r}) = 0. \quad (2.13)$$

The choice of testing functions is also arbitrary but some methods are more popular in practice. If the testing functions are chosen to be the same as the basis functions, the method is called *Galerkin's method*. It can be proven that Galerkin's method is equivalent to Rayleigh–Ritz variational method [8]. When the error is constrained to be satisfied on a set of discrete points on the scatterer, which corresponds to choosing testing functions to be delta functions on the scatterer surface, the method is named as *point matching*, and when they are chosen to be pulse functions defined over the subdomains of the geometry, the method is called *collocation by subdomains*. When the testing functions are chosen to be the complex conjugates of the basis functions, the formulation results in the minimization of the square of the error. Throughout this thesis, Galerkin's method is used. In addition to being a variational method, another advantage of the Galerkin's method is that the resultant MoM matrix is symmetric. Therefore, one need only compute and store half of the MoM matrix  $Z_{mn}$ . This is also an important consideration for the choice of the solution algorithm.

Direct application of the MoM requires the computation of  $N^2$  double surface integrals appearing in Eq. (2.11) as the elements of the resulting MoM matrix. Solution of this system of equations by Gaussian elimination requires  $O(N^3)$  operations. Iterative solvers require  $O(N^2)$  operations per iteration. The memory requirement of the MoM is also  $O(N^2)$ . This large order for storage limits the size of the problem that can be solved on a given hardware,

and the high operation cost poses a limit to the size of problems that can be solved in a practically acceptable period of time. For these reasons, the FMM is proposed [5, 6, 7, 10], which requires less memory and CPU time for the solution of large problems.

## 2.3 Multipole Expansions and FMM Formulation

Direct application of the MoM requires the computation of  $N^2$  double surface integrals appearing as the elements of the resultant MoM matrix and  $O(N^2)$  operations per iteration for the iterative solution of the resulting system of equations. A clever way to overcome the difficulties arising from these large storage and computation complexities is used in the FMM. The FMM is developed using two elementary identities. The first is the expansion of the scalar Green's function appearing in Eq. (2.11) as

$$\frac{e^{ik|\mathbf{r}+\mathbf{d}|}}{|\mathbf{r}+\mathbf{d}|} = ik \sum_{l=0}^{\infty} (-1)^l (2l+1) j_l(kd) h_l^{(1)}(kr) P_l(\hat{\mathbf{d}} \cdot \hat{\mathbf{r}}), \quad (2.14)$$

which is a form of Gegenbauer's addition theorem [11]. Here  $j_l$  is the spherical Bessel function,  $h_l^{(1)}$  is the spherical Hankel function of the first kind,  $P_l$  is the Legendre polynomial, and  $d < r$  is the condition for the validity of the expansion. In the FMM formulations of scattering problems, where the source point is denoted by  $\mathbf{x}'$  and the observation point by  $\mathbf{x}$ ,  $\mathbf{r}$  will be chosen to be close to  $\mathbf{x} - \mathbf{x}'$  so that  $\mathbf{d}$  will be small as depicted in Fig. 2.1. The second identity is the expansion of  $j_l P_l$  product appearing in Eq. 2.14 as a sum of

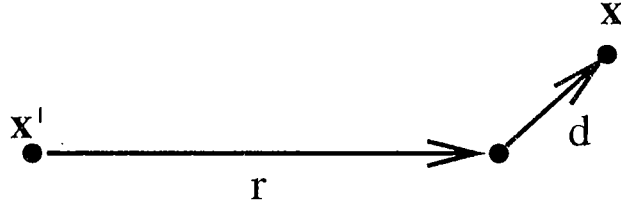


Figure 2.1: The basic geometry illustrating the relationship between  $\mathbf{x}, \mathbf{x}'$ ,  $r$ , and  $d$ .

propagating plane waves [11]:

$$4\pi i^l j_l(kd) P_l(\hat{\mathbf{d}} \cdot \hat{\mathbf{r}}) = \int d^2 \hat{\mathbf{k}} e^{i\mathbf{k} \cdot \mathbf{d}} P_l(\hat{\mathbf{k}} \cdot \hat{\mathbf{r}}). \quad (2.15)$$

The Green's function in Eq. (2.14) can be rewritten using Eq. (2.15) as

$$\frac{e^{ik|\mathbf{r}+\mathbf{d}|}}{|\mathbf{r}+\mathbf{d}|} = \frac{ik}{4\pi} \int d^2 \hat{\mathbf{k}} e^{i\mathbf{k} \cdot \mathbf{d}} \sum_{l=0}^{\infty} (2l+1) h_l^{(1)}(kr) P_l(\hat{\mathbf{k}} \cdot \hat{\mathbf{r}}), \quad (2.16)$$

where the orders of summation and integration are interchanged. The idea of the FMM is that the function

$$T_L(kr, \hat{\mathbf{k}} \cdot \hat{\mathbf{r}}) = \sum_{l=0}^L (2l+1) h_l^{(1)}(kr) P_l(\hat{\mathbf{k}} \cdot \hat{\mathbf{r}}) \quad (2.17)$$

can be computed for various values of  $kr$  which is independent of  $kd$ . The series is truncated at the  $L$ th term in numerical practice. The number of terms kept,  $L+1$ , depends on the maximum allowed value of  $kd$ , as well as the desired accuracy. The choice of  $L$  will be mentioned later. Using Eq. 2.16, Eq. (2.14) becomes

$$\frac{e^{ik|\mathbf{r}+\mathbf{d}|}}{|\mathbf{r}+\mathbf{d}|} \approx \frac{ik}{4\pi} \int d^2 \hat{\mathbf{k}} e^{i\mathbf{k} \cdot \mathbf{d}} T_L(kr, \hat{\mathbf{k}} \cdot \hat{\mathbf{r}}). \quad (2.18)$$

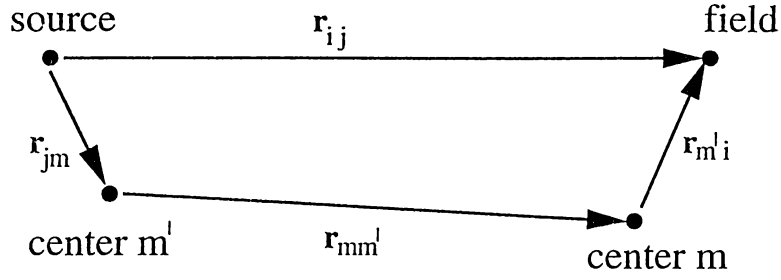


Figure 2.2: The geometry construction used in FMM formulations, illustrating the relation between source point, field point and the group centers.

### 2.3.1 Formulations for the FMM

The direct path from a source point to the field point can be decomposed into three parts as in Fig. 2.2, where

$$\mathbf{r}_{ji} = \mathbf{r}_{jm} + \mathbf{r}_{mm'} - \mathbf{r}_{im'}. \quad (2.19)$$

The idea to be noted is that the same path will be used for all source point in cluster  $m'$  to translate their field to all observation points in cluster  $m$ . Equation (2.16) can be rewritten as

$$\frac{e^{ikr_{ji}}}{r_{ji}} \approx \frac{ik}{4\pi} \int d^2\hat{k} e^{i\mathbf{k}\cdot(\mathbf{r}_{jm}-\mathbf{r}_{im'})} T_L(kr_{mm'}, \hat{k} \cdot \hat{r}_{mm'}) \quad (2.20)$$

and the Green's function becomes

$$\begin{aligned} \bar{\mathbf{G}}(\mathbf{r}_j, \mathbf{r}_i) &= \left[ \bar{\mathbf{I}} - \frac{1}{k^2} \nabla \nabla' \right] \frac{e^{ikr_{ji}}}{r_{ji}} \\ &\approx \int d^2\hat{k} \left[ \bar{\mathbf{I}} - \frac{1}{k^2} \nabla \nabla' \right] e^{i\mathbf{k}\cdot(\mathbf{r}_{jm}-\mathbf{r}_{im'})} T_L(kr_{mm'}, \hat{k} \cdot \hat{r}_{mm'}) \\ &= \int d^2\hat{k} \left[ \bar{\mathbf{I}} - \hat{k}\hat{k} \right] e^{i\mathbf{k}\cdot(\mathbf{r}_{jm}-\mathbf{r}_{im'})} T_L(kr_{mm'}, \hat{k} \cdot \hat{r}_{mm'}). \end{aligned} \quad (2.21)$$

Using the above equations, a matrix element as in Eq. (2.11) is approximated by

$$\begin{aligned} Z_{mn} &= \int_s d\mathbf{s} \mathbf{t}_m(\mathbf{r}) \cdot \int_{s'} ds' \left[ \mathbf{j}_n(\mathbf{r}') + \frac{1}{k^2} \nabla' \cdot \mathbf{j}_n(\mathbf{r}') \nabla \right] \frac{e^{ikR}}{R} \\ &\approx \frac{ik}{4\pi} \int d^2\hat{k} \mathbf{V}_{fmj}(\hat{k}) \cdot T_L(kr_{mm'}, \hat{k} \cdot \hat{r}_{mm'}) \mathbf{V}_{sm'i}^*(\hat{k}), \end{aligned} \quad (2.22)$$

where

$$\begin{aligned}\mathbf{V}_{sm'i}(\hat{k}) &= \int_S ds' e^{i\mathbf{k}\cdot\mathbf{r}_{im'}} [\bar{\mathbf{I}} - \hat{k}\hat{k}] \cdot \mathbf{j}_i(\mathbf{r}_{im'}), \\ \mathbf{V}_{fmj}(\hat{k}) &= \int_S ds e^{i\mathbf{k}\cdot\mathbf{r}_{jm}} [\bar{\mathbf{I}} - \hat{k}\hat{k}] \cdot \mathbf{t}_j(\mathbf{r}_{jm})\end{aligned}\quad (2.23)$$

are the Fourier transforms of the basis and testing functions, respectively, and the superscript \* denotes complex conjugation.

The FMM is proposed for the acceleration of the matrix-vector product computed at each iteration of an iterative solution scheme, like the conjugate gradient method, employed for the solution of the resultant matrix equation. The algorithm is outlined in the next subsection.

### 2.3.2 Description of the FMM Algorithm

Normally the matrix-vector product at each iteration of an iterative solver would require  $O(N^2)$  multiplications for the solution of an  $N \times N$  system of equations. Employing the algorithm below, it is possible to reduce this order to  $O(N^{1.5})$ . The FMM algorithm can be described as follows:

1. The  $N$  basis functions are divided into  $M$  localized groups (clusters), each containing about  $N/M$  basis functions.
2. For groups that are distant to each other, the translation functions of Eq. (2.17) for each pair of distant groups are calculated for a predetermined set of  $\hat{k}$  directions. Choice of this set of  $\hat{k}$  directions and the

choice of truncation limit for the series will be mentioned later. This requires  $O(KLM(M - G))$  computations, where  $G$  is the average number of nearby groups to each group,  $K$  is the number of  $\hat{k}$  directions, and  $L$  is the number of terms kept in Eq. (2.17).

3. The Fourier transforms of each basis function are computed for the pre-determined set of  $\hat{k}$  directions. This step requires  $O(KN)$  computation.
4. For groups that are near or close to each other (the closeness is defined in the sense that either Eq. (2.14) is not valid or the computation requires too many terms of the series to be considered for at least one pair of source and field points), a sparse matrix denoted by  $Z'$  is constructed, with direct computation of matrix elements using Eq. (2.11). This step requires  $O(G(N/M)^2 M)$  computations.
5. The  $KM$  quantities called aggregations

$$\mathbf{s}_{m'}(\hat{k}) = \sum_i \mathbf{V}_{sm'i}^*(\hat{k}) a_{m'i}, \quad (2.24)$$

which represent the far field of each group  $m'$  are computed using the precomputed Fourier transforms. This step requires  $O(KN)$  operations.

6. The  $KM$  quantities called translations

$$\mathbf{g}_m(\hat{k}) = \sum_{m'} T_{mm'}(\hat{k}) \mathbf{s}_{m'}(\hat{k}) \quad (2.25)$$

representing the Fourier components of the field in the neighborhood of group  $m$ , generated by the sources in the groups that are not nearby are computed next. This step requires  $O(KM(M - G))$  operations using the precomputed values of  $T_{mm'}(\hat{k})$ .

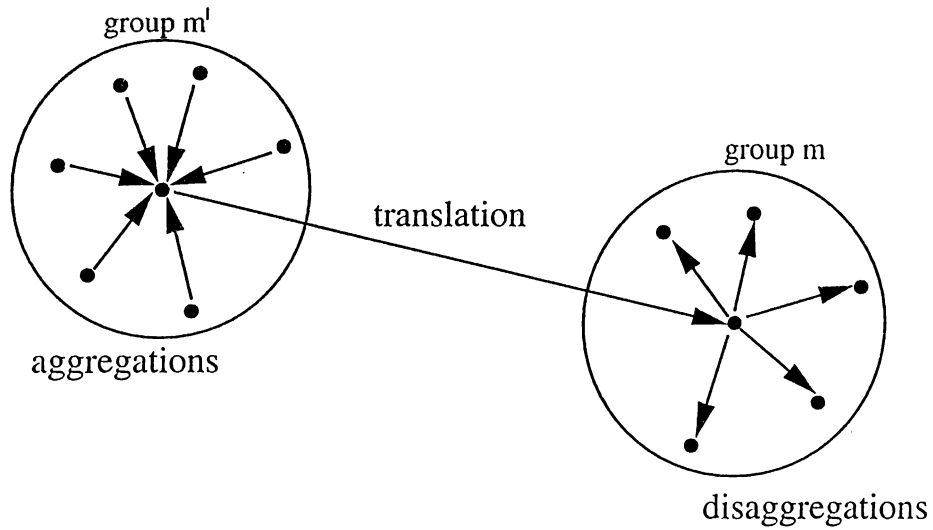


Figure 2.3: Illustration of the FMM strategy.

7. Finally, the disaggregations of the fields of all sources in distant groups are computed from the group centers to the testing functions and added to the sparse matrix-vector product, which represents the testing of the field generated by the sources in nearby groups. This computation can be expressed as

$$B_{mj} = \sum_{m'i} Z'_{mjm'i} a_{m'i} + \int d^2 \hat{k} \mathbf{V}_{mj}(\hat{k}) \cdot \mathbf{g}_m(\hat{k}). \quad (2.26)$$

Figure 2.3 depicts the three main steps of the algorithm.

$L$  is proportional to the size  $D$ , the maximum of the diameters of all groups, and  $K = 2L^2$  is approximately proportional to  $D^2$ . Since  $D^2$  is approximately proportional to  $N/M$ , the number of unknowns in a cluster (for surface scatterers), computation of the vector  $\mathbf{B}$  in Eq. 2.26 requires  $aNM + bN^2/M$  operations, where  $a$  and  $b$  are machine-dependent constants. This total operation count is minimized by choosing  $M = \sqrt{bN/a}$ , and the result is an  $O(N^{1.5})$  algorithm.



Extensions of the FMM that can further reduce this computational complexity exist in the literature. Multilevel FMM [12], which extends the FMM strategy with multilevel grouping, can reduce the computational complexity to  $O(N \log N)$ . Ray-propagation fast multipole algorithm (RPFMA) [13, 14] reduces the complexity to  $O(N^{4/3})$ . The fast far-field approximation (FAFFA) [15] also results in an  $O(N^{4/3})$  algorithm. Among the methods mentioned above, only the FMM is implemented in this work. The implementations of the extensions of the FMM mentioned above are among the future work that can be carried on on this subject.

### 2.3.3 Required Number of Multipoles and Directions

In the numerical implementation of the FMM, the series in Eq. (2.14) is evaluated using a finite number of terms. The number of terms that must be evaluated is chosen so that the expansion converges to the desired accuracy. For  $l < z$  the Bessel functions  $j_l(z)$  and  $h_l^{(1)}(z)$  are nearly constant in magnitude, and for  $l > z$ ,  $j_l(z)$  decays rapidly and  $h_l^{(1)}(z)$  grows rapidly. Therefore, the truncation limit cannot be chosen to be much larger than  $kr_{mm'}$ , since the numerical evaluation of the integral in Eq. (2.16) will cause inaccuracies due to the oscillatory integrand. A semi-empirical fit given in [7] to the number of multipoles required for single precision (32-bit reals) is

$$L_s(kD) = kD + 5 \ln(kD + \pi), \quad (2.27)$$

where  $D \geq 1/k$  is the maximum group diameter. For double precision, the estimate is

$$L_s(kD) = kD + 10 \ln(kD + \pi). \quad (2.28)$$

If the value of  $L$  dictated by the above formula used exceeds  $kr_{mm'}$ , then the groups must be considered as neighboring, and their interaction must be included in the sparse near-field matrix  $Z'_{mn}$ .

The integral in Eq. (2.16) must be evaluated using a quadrature rule that would provide sufficient accuracy in the result. A simple method for determining the sampling points is to pick polar angles  $\theta$  such that they are zeros of  $P_L(\cos \theta)$ , and azimuthal angles  $\phi$  to be  $2L$  equally spaced points so that the azimuthal variation is sampled at the Nyquist rate. For this choice,  $K = 2L^2$ .

### 2.3.4 Memory Requirements and Computational Complexity

The memory required for the FMM can be considered in two parts, the sparse-matrix storage and the FMM elements' storage. The storage of the sparse  $Z'$  matrix requires  $O(N^2/M)$  memory locations. The FMM aggregations need  $O(KN)$  memory locations, and the FMM translations need  $O(KLM^2)$  memory locations. Hence the total memory storage needed is  $O(N^2/M) + O(KN) + O(KLM^2)$ . Using the proportionalities  $K \propto L^2$ ,  $D^2 \propto N/M$ , and  $L \propto D$ , this expression can be simplified to  $C_1(N^2/M) + C_2(NM\sqrt{N/M})$ , where  $C_1$  and  $C_2$  are machine- and implementation-dependent constants. The coefficient  $C_2$  is so small compared to  $C_1$  for all problem sizes that can be solved with the FMM that the memory required is dominated by the  $O(N^2/M)$  term.

The computational complexity of the FMM can be determined by counting the number of floating-point operations required at each step of the algorithm. The aggregation step requires  $MKN/M = KN$  operations. The

translation step requires  $KM^2$  operations with the precomputed  $KM^2$  values of the translation function given in Eq. (2.17). The disaggregations require  $MKN/M = KN$  operations, and finally the sparse matrix-vector product requires  $N^2/M$  operations. Using the proportionalities  $K \propto L^2$ ,  $D^2 \propto N/M$ , and  $L \propto D$ , the total cost of the matrix-vector product is found as  $O(NM) + O(N^2/M)$ . This can be minimized by choosing  $M = \sqrt{N}$  and the result is an  $O(N^{1.5})$  algorithm. The memory required for the FMM also becomes  $O(N^{1.5})$ . Both the operation cost and the memory requirement of the FMM is less than those of standard MoM formulation for problem sizes larger than 1000, which makes the FMM more suitable for the solution of large problems.

## Chapter 3

# Geometry-Modeling Techniques

Real-life electromagnetic scattering problems, almost always, involve electrically large scatterers with complicated geometries. In the formulation of scattering problems involving three-dimensional arbitrarily curved scatterers, the geometry of the scatterer has to be approximated. Various geometry approximation and modeling techniques exist for this purpose [16, 17], some of which are presented in this chapter.

As the electrical size of a geometry gets larger, the size of the problem increases and the CPU time consumed and the memory required to obtain the solution grows rapidly. Hence, the maximum size of the problem that can be solved on a given hardware is limited by these two factors. Using better geometry models for the scatterers, it is possible to reduce the size of the problem. As an introduction to the mathematical background of the subject of better modeling, parametric space curves will be mentioned in the next section.

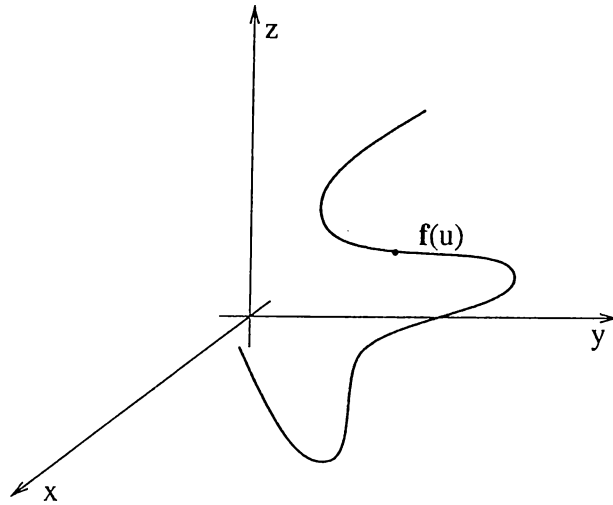


Figure 3.1: A parametric space curve is a vector function of a parameter  $u$ .

### 3.1 Parametric Space Curves

A general 3-D parametric curve in space (Fig. 3.1) is written of the form  $\mathbf{f}(u)$ , where  $\mathbf{f}$  is a vector containing the Cartesian coordinates of the point on the space curve having the parameter value  $u$ .

If  $\mathbf{f}(u)$  is an  $n$ th degree polynomial function of  $u$  having a set of vectors  $\{\mathbf{a}_0, \mathbf{a}_1, \dots, \mathbf{a}_n\}$  as coefficients, i.e.,

$$\mathbf{f}(u) = \sum_{i=0}^n \mathbf{a}_i u^i, \quad (3.1)$$

then one can specify the whole curve uniquely with this set of coefficients. Alternatively, one can specify another set of  $n + 1$  points through which the  $n$ th degree parametric polynomial curve is supposed to pass.

There are other methods of specifying an  $n$ th degree parametric polynomial curve, one of the most popular being the so called Bézier curves [17]. A Bézier curve is specified by an alternative set of points which is called the defining polygon. The shape of the actual curve closely follows the shape of the defining

polygon. Figure 3.2 shows a generic third-order Bézier curve and its defining polygon.

These curves have the following nice properties:

- The degree of the polynomial defining the curve segment is one less than the number of defining polygon points.
- The curve generally follows the shape of the defining polygon.
- The first and the last points on the curve are coincident with the first and the last points of the defining polygon.
- The tangent vectors at the ends of the curve have the same direction as the first and the last polygon spans, respectively.
- The curve is contained within the convex hull of the defining polygon, i.e., within the largest convex polygon obtainable with the defining polygon vertices.
- The curve exhibits the variation-diminishing property. Basically, this means that the curve does not oscillate about a straight line more than the defining polygon.
- The curve is invariant under an affine transformation. An affine transformation is a combination of linear transformations such as translation and rotation.

A parametric Bézier curve is mathematically defined by

$$\mathbf{P}(u) = \sum_{i=0}^n \mathbf{a}_i B_{n,i}(u) \quad 0 \leq u \leq 1, \quad (3.2)$$

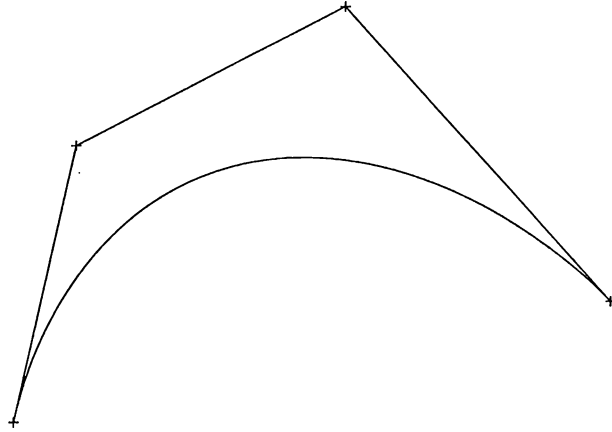


Figure 3.2: A generic Bézier curve and its defining polygon.

where the Bézier or Bernstein basis or blending function is

$$B_{n,i}(u) = \binom{n}{i} u^i (1-u)^{n-i} \quad (3.3)$$

with

$$\binom{n}{i} = \frac{n!}{i!(n-i)!} \quad (3.4)$$

and  $\mathbf{a}_i$  are the defining polygon vertices.

Another useful group of parametric curves is the B-spline curves [16, 17]. These curves are formed by blending Bézier curves. An  $n$ th degree B-spline curve is formed by connecting  $n$ th degree Bézier curves and imposing  $(n-1)$ st derivative continuity at the junction points. The local parameter of each Bézier curve runs from 0 to 1 where the global parameter  $t$  of the whole curve is defined in terms of the local parameters. A knot vector defining which of the polygon points form the sub-Bézier curve must also be specified. If this knot vector is nonuniform then the resulting curve is called a nonuniform B-spline.

B-splines can also be written as an expansion

$$\mathbf{P}(u) = \sum_{i=0}^n \mathbf{a}_i N_{n,i}(u) \quad 0 \leq u \leq 1, \quad (3.5)$$

where  $N_{n,i}(u)$  are B-spline blending functions, which are also functions of the knot vector.

B-spline curves has the interesting property of local control, i.e., when one of its vertices is moved to a new location only the part of the curve around that vertex changes shape. For Bézier curves, this is not the case since the basis functions for them are global, i.e., non-zero over the interval  $0 \leq u \leq 1$ , hence a change in the position of one of the vertices is felt on the entire curve. The basis-function terminology used here should not be confused with the basis functions used to expand the unknown function in the MoM formulation.

Extensions of Bézier and B-spline curves are rational Bézier and rational B-spline curves. They allow one to give weights to each polygon vertex giving these curves one more degree of freedom. This is accomplished by projecting the 4-dimensional Bézier and B-spline curves to 3-dimensional real space. A rational Bézier curve can be expressed as

$$\mathbf{P}(u) = \frac{\sum_{i=0}^n \mathbf{a}_i \omega_i B_{n,i}(u)}{\sum_{i=0}^n \omega_i B_{n,i}(u)} \quad 0 \leq u \leq 1, \quad (3.6)$$

where  $\omega_i$  is the weight of the  $i$ th vertex of the defining polygon.

Blending rational Bézier curves with a nonuniform knot vector results in the very popular NURBS curve representation. This powerful curve definition is used in most of the available CAGD tools.



## 3.2 Exact Parametric Models

All canonical surfaces have exact parametric representations. A sphere, for example, can be formulated in terms of  $\theta$  and  $\phi$  angle parameters. In order the problem geometry be exactly representable, it must be formed from a set of exactly representable subgeometries, such as spherical, conical, or polynomial subsurfaces. This is almost never the case for the scatterers encountered in real-life electromagnetics problems. The geometry of the scatterer is, thus, approximated by parametric subsurfaces, some of which are more popular than others. In the next section some of those popular approximation tools are presented.

## 3.3 Polynomial Interpolation Surfaces

This is the first class of the geometry-modeling techniques. The scatterer surface is approximated by polynomial surface patches. In the approximation process, these subsurfaces are constrained to pass through a set of points in space, which are sampled from the original scatterer surface. In practice, the subsurfaces used are limited to second-order polynomial subsurfaces.

### 3.3.1 Staircase Approximation

This is the zeroth-order polynomial approximation to the problem geometry. The problem geometry is approximated by a collection of cubic and rectangular-prism-like cells as depicted in Fig. 3.3. This modeling scheme is

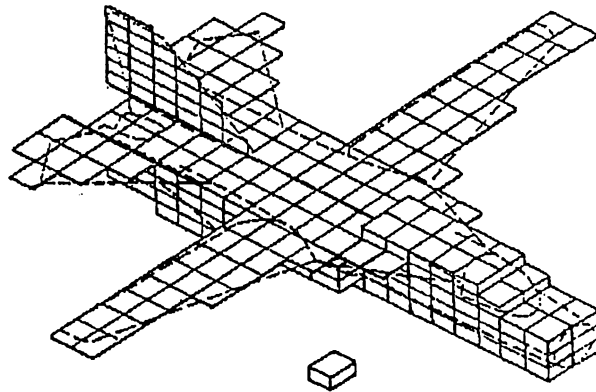


Figure 3.3: An aircraft approximated by a mesh of rectangular cells. (Reproduced from [18].)

very popular in finite-difference methods [18]. In real-life scattering problems, for the scatterer geometry be modeled accurately enough, the number of subdomains used must be very large, indicating that the problem size can fall out of practical solution ranges.

### 3.3.2 Flat Triangulations

This scheme can be considered as the first-order polynomial surface fit to the problem geometry. It is a very popular method and is used not only in the area of numerical electromagnetics, but also in a wide variety of disciplines in science and technology. The problem geometry is approximated by a collection of connected flat triangular subdomains (Fig 3.4). It is very flexible in modeling and in formulations. This technique is widely used in the MoM formulations with the popular RWG BFs [1, 19, 20]. The form of a flat triangular patch is

$$\mathbf{r}(u, v) = \mathbf{a}_0 + \mathbf{a}_1 u + \mathbf{a}_2 v \quad (3.7)$$

and  $\mathbf{a}_i$ 's are related to the vertices of the triangle. The triangulation of the sphere is shown in Fig. 3.4.

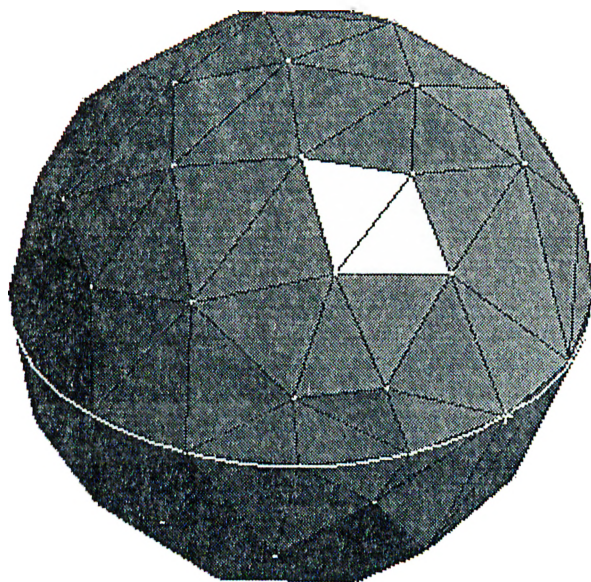


Figure 3.4: Sphere approximated by a mesh of flat triangles. The triangulation is performed by MSC/ARIES.

### 3.3.3 Quadratic Triangulations

One higher degree of polynomial surfaces is the quadratic triangulations. These are curved triangular subdomains defined by 6 discrete points in space. These points must be defined on a topologically triangular curve. The capability of representing curved problem geometries of these subdomains makes them attractive in the formulation of real-life electromagnetics problems involving arbitrary, curved geometries. The form of a curved triangular patch is

$$\mathbf{r}(u, v) = \mathbf{a}_0 + \mathbf{a}_1 u + \mathbf{a}_2 v + \mathbf{a}_3 uv + \mathbf{a}_4 u^2 + \mathbf{a}_5 v^2 \quad (3.8)$$

and  $\mathbf{a}_i$ 's are related to the 6 points defining the curved triangular patch. The triangulation of the sphere using quadratic triangular patches is shown in Fig. 3.5.

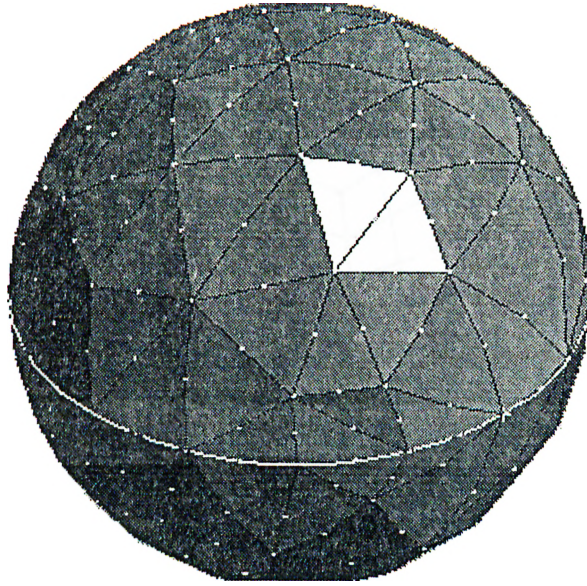


Figure 3.5: Sphere approximated by a mesh of 6-point quadratic triangles. The triangulation is performed by MSC/ARIES.

### 3.3.4 Biquadratic Approximations

These surfaces are formed from the cross-products of second-order polynomials, and each surface is defined by 9 discrete points in space. For quadrilateral surface patches, these 9 points must be defined on a topologically rectangular grid. When one of the parameters are fixed, the curve traced by the other parameter is a parabola in space. They are also used in the MoM formulations of electromagnetic scattering problems [2]. The form of a curved rectangular patch is

$$\mathbf{r}(u, v) = \sum_{i=0}^2 \sum_{j=0}^2 \mathbf{a}_{ij} u^i v^j. \quad (3.9)$$

A sphere approximated by biquadratic patches is shown in Fig. 3.6.

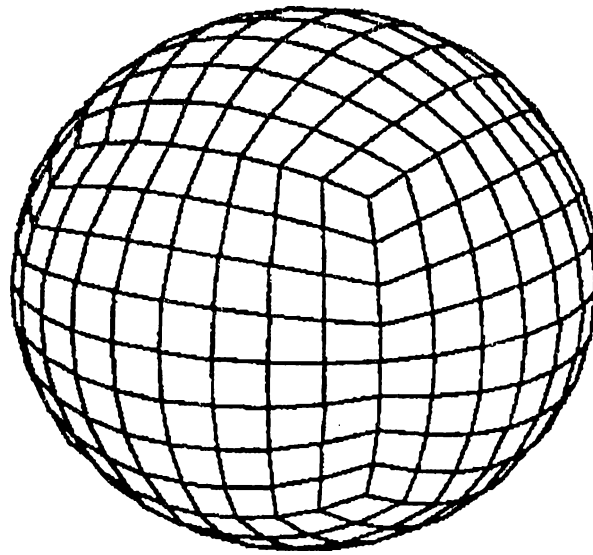


Figure 3.6: Sphere approximated by a mesh of 9-point biquadratic rectangular patches. Reproduced from

### 3.4 Free-Form Surfaces

The polynomial surfaces defined in Section 3.3 are surfaces that are constrained to pass through *existing* data points, i.e., they are surface-fitting techniques. In many cases, excellent results are obtained with these methods. They are suitable for surface approximations when a set of sampled data about the surface is available. This data may be obtained as a result of an experiment or a mathematical calculation. Examples are engine manifolds, aircraft wings, and similar mechanical and structural parts. However, when the design of the shape of the body depends also on the functional and aesthetic requirements, which cannot be formulated entirely in terms of quantitative criteria, one has to resort to a combination of computational and heuristic methods. An alternative method suitable for heuristic design of curves and surfaces was developed by Pierre Bézier.

### 3.4.1 Bézier Patches

Making use of the previously defined powerful Bézier and B-spline curve concepts, one can also form a basis for surface description [16, 17]. Tensor product Bézier surfaces are defined as

$$\mathbf{r}(u, v) = \sum_{i=0}^m \sum_{j=0}^n \mathbf{b}_{ij} B_i^m(u) B_j^n(v). \quad (3.10)$$

This definition can also be given in matrix form as

$$\mathbf{r}(u, v) = [U][N][A][M]^T[V], \quad (3.11)$$

where

$$[U] = [u^n \ u^{n-1} \ \dots \ 1], \quad (3.12)$$

$$[V] = [v^m \ v^{m-1} \ \dots \ 1]^T, \quad (3.13)$$

$$[A] = \begin{bmatrix} \mathbf{a}_{00} & \dots & \mathbf{a}_{0m} \\ \vdots & & \vdots \\ \mathbf{a}_{n0} & & \mathbf{a}_{nm} \end{bmatrix}, \quad (3.14)$$

and  $[N]$  and  $[M]$  are given by

$$[N] = \begin{bmatrix} k_{00}^{(n)} & \dots & k_{0n}^{(n)} \\ \vdots & & \vdots \\ k_{n0}^{(n)} & \dots & k_{nn}^{(n)} \end{bmatrix}, \quad [M] = \begin{bmatrix} k_{00}^{(m)} & \dots & k_{0m}^{(m)} \\ \vdots & & \vdots \\ k_{m0}^{(m)} & \dots & k_{mm}^{(m)} \end{bmatrix}, \quad (3.15)$$

with

$$k_{ij}^l = (-1)^{j-i} \binom{l}{j} \binom{j}{i} \quad \text{and} \quad \binom{l}{j} = \frac{l!}{j!(l-j)!}. \quad (3.16)$$

For quadrilateral surface patches, the defining polygon net must be topologically rectangular, i.e., the net must have the same number of vertices in

each “row”. Figure 3.7 shows a generic quadratic Bézier patch and its defining polygon mesh. They share the following similar properties as Bézier curves:

- The degree of the surface in each parametric direction is one less than the number of defining polygon vertices in that direction.
- The continuity of the surface in each parametric direction is two less than the number of defining polygon vertices in that direction.
- The surface generally follows the shape of the defining polygon net.
- Only the corner points of the defining polygon net and the surface are coincident.
- The surface is contained within the convex hull of the defining polygon net
- The surface does not exhibit the variation-diminishing property. The variation-diminishing property for bivariate surfaces is undefined.
- The surface is invariant under an affine transformation.

Each of the boundary curves of a Bézier surface is a Bézier curve. The tangent vectors at the patch corners are controlled both in direction and magnitude by the position of adjacent points along the edges of the net. The interior polygon net vertices *influence* the direction and magnitude of the twist vectors at the corners of the patch. Consequently, the user can control the shape of the surface patch without an intimate knowledge of the tangent and twist vectors.

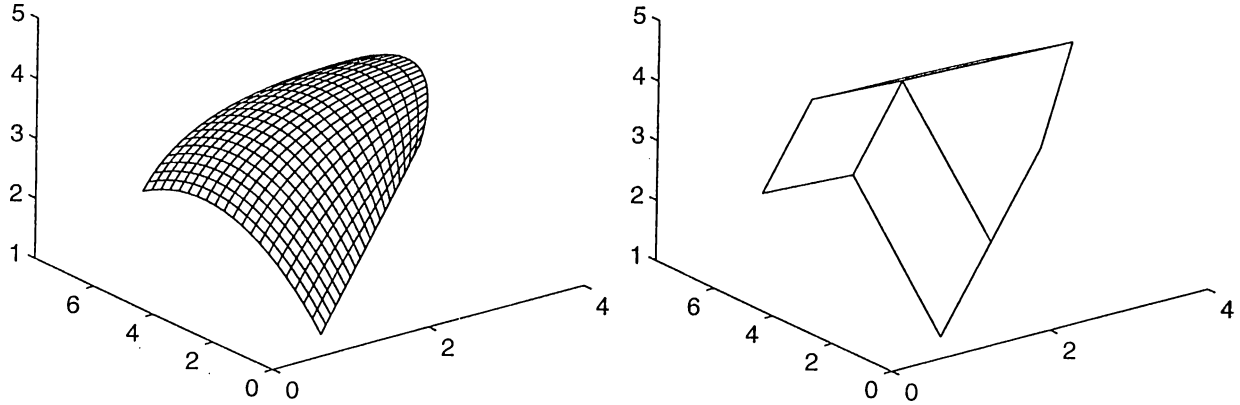


Figure 3.7: Tensor product Bézier surface and its defining polygon net.

The above discussion of Bézier surfaces concentrates on the definition and the characteristics of a single surface patch. For more complex surfaces multiple Bézier surface patches must be joined together.

### 3.4.2 B-spline Surfaces

Cartesian-product B-spline surfaces are the natural extensions of Cartesian-product Bézier surfaces, defined by

$$\mathbf{r}(u, v) = \sum_{i=0}^m \sum_{j=0}^n \mathbf{b}_{ij} N_i^m(u) M_j^n(v), \quad (3.17)$$

where  $N_i^m(u)$  and  $M_j^n(v)$  are the B-spline basis functions in the biparametric  $u$  and  $v$  directions. They are actually blended Bézier surfaces, so one can transform a B-spline surface to a set of connected Bézier surfaces.

As with B-spline curves, the shape and character of a B-spline surface is significantly influenced by the knot vectors in the parametric directions. Open, periodic, and nonuniform knot vectors are used. For example, it is possible to



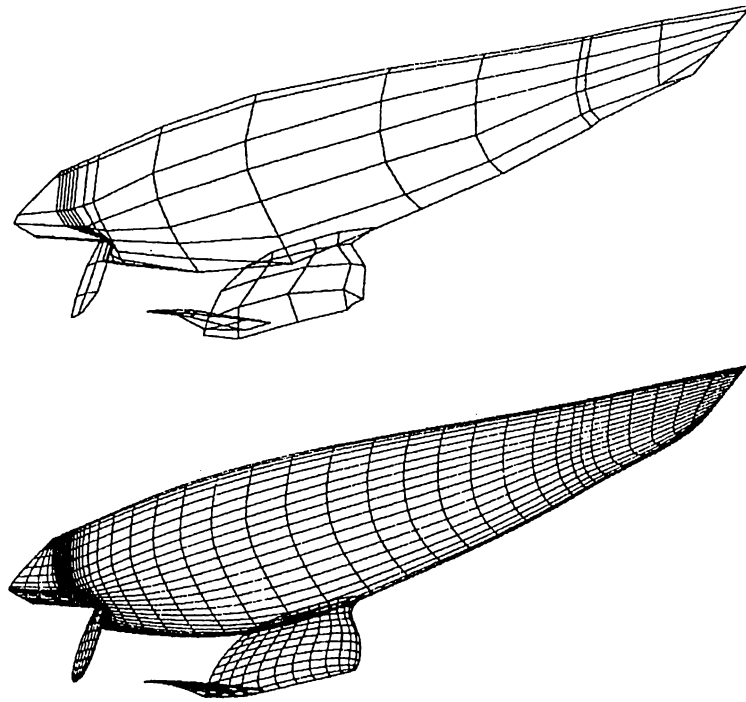


Figure 3.8: A yacht hull defined as a B-spline surface, the defining polygon net and the parametric representation. (Reproduced from [16].)

use an open knot vector for one parametric direction and a periodic knot vector for the other; the result is a cylindrical surface of varying cross-sectional area. As an example to the modeling power of B-splines, a yacht hull represented by B-spline surfaces is shown in Fig. 3.8.

The local control properties of B-spline curves also carry over to B-spline surfaces.

### 3.4.3 Nonuniform Rational B-Spline (NURBS) Surfaces

Bézier and B-spline surfaces can be generalized to their rational counterparts. A rational Bézier or B-spline surface is defined as the projection of a 4-dimensional tensor product Bézier or B-spline surface. Thus the rational Bézier patch takes the form

$$\mathbf{r}(u, v) = \frac{\sum_{i=0}^m \sum_{j=0}^n \omega_{ij} \mathbf{b}_{ij} B_i^m(u) B_j^n(v)}{\sum_{i=0}^m \sum_{j=0}^n \omega_{ij} B_i^m(u) B_j^n(v)}, \quad (3.18)$$

and a rational B-spline surface is written as

$$\mathbf{r}(u, v) = \frac{\sum_{i=0}^m \sum_{j=0}^n \omega_{ij} \mathbf{b}_{ij} N_i^m(u) M_j^n(v)}{\sum_{i=0}^m \sum_{j=0}^n \omega_{ij} N_i^m(u) M_j^n(v)}. \quad (3.19)$$

It must be noted here that these surfaces are not tensor product surfaces themselves. As for nonrational counterparts, open uniform, periodic uniform, and nonuniform knot vectors can be used to generate rational Bézier and B-spline surfaces.

One of the strong attractions of rational B-spline surfaces is their ability to represent quadric surfaces which are given by the general expression

$$Ax^2 + By^2 + Cz^2 + Dxy + Eyz + Fxz + Gx + Hy + Jz + K = 0 \quad (3.20)$$

and to blend them smoothly into higher-order sculptured surfaces. One can represent a sphere exactly using a single rational B-Spline surface, which is a collection of smoothly blended rational Bézier patches. The sphere and the defining polygon net are shown in Fig. 3.9 (c). Figures 3.9 (a) and (b) are the construction curves used to generate the sphere.

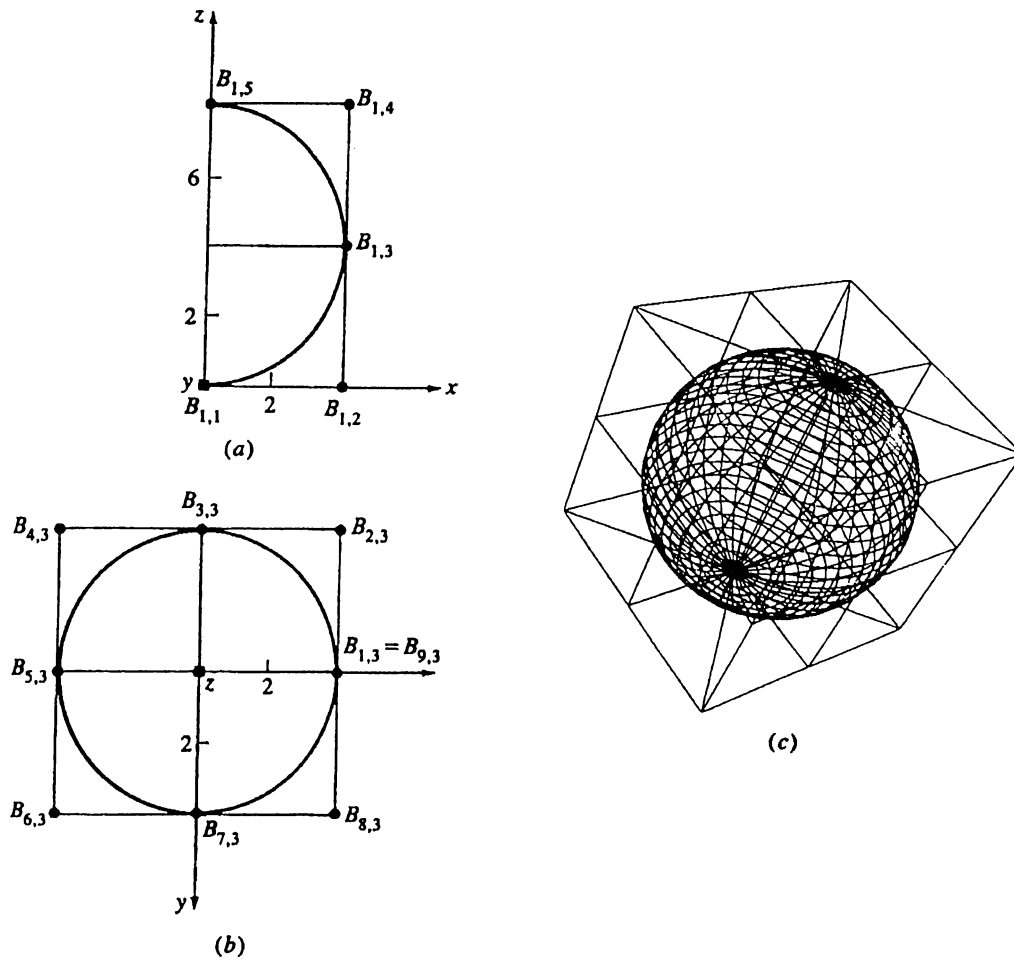


Figure 3.9: Sphere generated as a rational B-spline surface. (a) Offset circle and defining polygon; (b) circle of revolution and defining polygon; (c) defining polygon net and sphere. (Reproduced from [16].)

# Chapter 4

## Basis Functions

Powerful basis functions (BFs) exist in the literature to use with the MoM formulation of electromagnetic scattering and radiation problems. The basis-function expansion employed for the formulation of the problem has to be capable of representing the unknown accurately. For electromagnetic scattering problems, the unknown is the surface current on the scatterer induced by an incident electromagnetic field. For a proper approximation of the surface current, the BFs used must be defined on the surface of the scatterer. In this chapter the definitions of the well-known Rao-Wilton-Glisson (RWG) BFs and rooftop (RT) BFs are given. Also their *curved* counterparts, that are conformal with curved parametric surfaces they are defined on, are presented. The formulations of these *curved* BFs are given in a form that is applicable to any parametric surface definition.

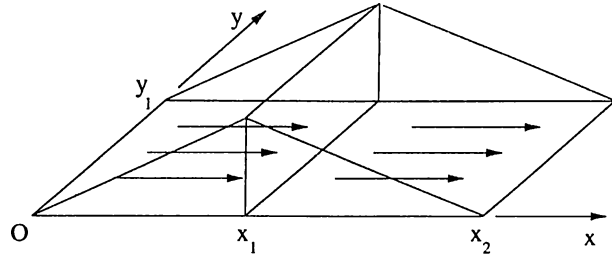


Figure 4.1: Rooftop basis function defined a pair of flat rectangular regions.

## 4.1 Rooftop (RT) Basis Functions

RT BFs are subdomain basis functions and are very popular and widely used in the MoM formulations of problems involving flat, rectangular geometries, such as the geometries encountered in the analysis and simulation of printed circuits. Their combination can approximate the unknown surface current piecewise linearly in the direction of current flow, and the approximation is piecewise constant in the transverse direction. On a pair of flat rectangular subdomains, they can be defined as

$$\mathbf{b}(x, y) = \begin{cases} \frac{x}{x_1} P(y/y_1) \hat{x} & 0 \leq x \leq x_1 \\ \frac{(x_2 - x)}{(x_2 - x_1)} P(y/y_1) \hat{x} & x_1 \leq x \leq x_2 \end{cases} \quad (4.1)$$

where  $P(y/y_1)$  is a pulse function that is nonzero for  $y$  values between 0 and  $y_1$ . The BF is defined by Eq. 4.1 is depicted in Fig. 4.1.

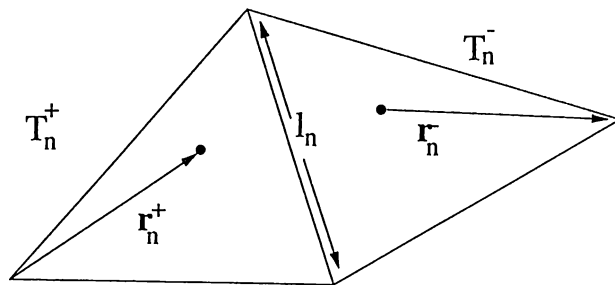


Figure 4.2: Rao–Wilton–Glisson basis function on a pair of flat triangular regions.

## 4.2 Rao-Wilton-Glisson (RWG) Basis Functions

These basis functions are defined over pairs of flat triangular subdomains. Due to the flexibility of flat triangulations in surface modeling, this basis function finds a wide range of applications in electromagnetic scattering and radiation problems. They are defined as

$$\mathbf{b}_n(\mathbf{r}) = \begin{cases} \frac{l_n}{2A_n^+} \mathbf{r}_n^+ & \text{in } T_n^+ \\ \frac{l_n}{2A_n^-} \mathbf{r}_n^- & \text{in } T_n^- \\ 0 & \text{otherwise} \end{cases} \quad (4.2)$$

where  $l_n$  is the length of the common edge, and  $A_n^+$  and  $A_n^-$  are the areas of the triangles  $T_n^+$  and  $T_n^-$ , respectively. The BF is shown in Fig. 4.2.

## 4.3 Curved Rooftop (CRT) Basis Functions

The RT BFs are suitable for the expansion of induced surface currents on flat and rectangular surfaces. They should be modified in order to be capable of

representing an unknown current density on a curved 3-D surface. CRT BFs are defined on curved surfaces in terms of the tangent vectors of the surfaces. The tangent vectors that form a basis for the definition of the basis function can be found by differentiating the parametric surface mapping with respect to each parameter, i.e.,

$$\mathbf{t}_u = \frac{\partial \mathbf{r}}{\partial u}, \quad \mathbf{t}_v = \frac{\partial \mathbf{r}}{\partial v}. \quad (4.3)$$

In the following formulation, a series of transformations will be defined, which should not be mixed up.

- A unit square is the region in the two-dimensional  $(u, v)$  parametric coordinate system which is defined by  $0 \leq u \leq 1$  and  $0 \leq v \leq 1$ .
- A 3-D curved rectangular patch is the mapping of the unit square in the  $(s, t)$  parametric domain into the 3-D  $(x, y, z)$  real space.
- A rectangular subdomain in the  $(s, t)$  domain can be considered as a mapping of the unit square on the  $(u, v)$  domain into the  $(s, t)$  domain.

Therefore, a curved rectangular subdomain, on a surface on which a CRT basis function is defined, can be considered as a mapping of a rectangular subdomain in the  $(s, t)$  parametric space, which, in turn, is the mapping of the unit square in the  $(u, v)$  parametric space into the  $(s, t)$  parametric space. Fig. 4.3 depicts the situation.

With the transformation

$$\mathbf{r}_a = u(\mathbf{r}_1 - \mathbf{r}_3) + v(\mathbf{r}_2 - \mathbf{r}_3) + \mathbf{r}_3, \quad (4.4)$$

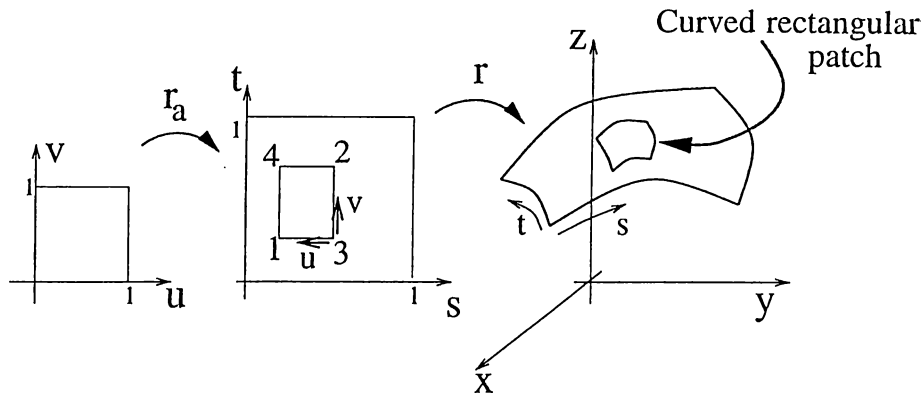


Figure 4.3: Composite mapping of the parametric unit square on the real curved surface.

where  $\mathbf{r}_i$  are the  $(s, t)$  coordinates of the four vertices of the rectangular subdomain, the unit square of the  $(u, v)$  space is mapped to a rectangular subdomain in the  $(s, t)$  parametric space. With the patch transformation, which is given to be the Bézier patch transformation here as an example, the rectangular subdomain in  $(s, t)$  space is mapped to the curved rectangular subdomain on the Bézier patch,

$$\mathbf{r}(s, t) = \frac{\sum_{i=0}^m \sum_{j=0}^n \omega_{ij} \mathbf{b}_{ij} B_i^m(s) B_j^n(t)}{\sum_{i=0}^m \sum_{j=0}^n \omega_{ij} B_i^m(s) B_j^n(t)}. \quad (4.5)$$

With the above composite transformation, the subdomain supporting half of the CRT BF on the patch is formed from the unit square of the  $(u, v)$  domain.

The CRT BFs can now be defined on the  $(u, v)$  domain very simply in terms of  $u$  and  $v$  parameters as

$$\mathbf{b}(u, v) = \frac{1}{\sqrt{g(u, v)}} u \frac{\partial \mathbf{r}(u, v)}{\partial u} \quad (4.6)$$

where  $g(u, v)$  is the determinant of the metric tensor, which is given by

$$g = \begin{vmatrix} g_{11} & g_{12} \\ g_{21} & g_{22} \end{vmatrix}, \quad (4.7)$$



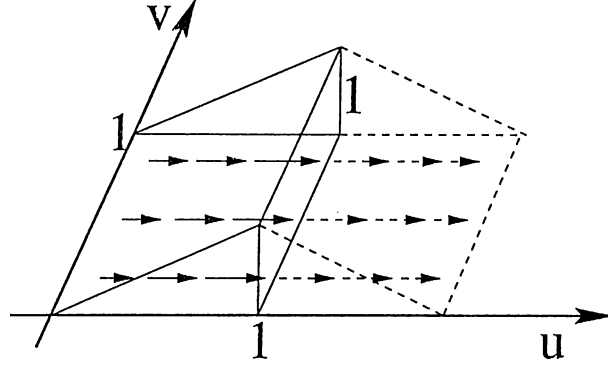


Figure 4.4: C-RT BF defined on the parametric space.

where

$$g_{11} = \frac{\partial \mathbf{r}}{\partial u} \cdot \frac{\partial \mathbf{r}}{\partial u}, \quad g_{12} = \frac{\partial \mathbf{r}}{\partial u} \cdot \frac{\partial \mathbf{r}}{\partial v}, \quad g_{21} = \frac{\partial \mathbf{r}}{\partial v} \cdot \frac{\partial \mathbf{r}}{\partial u}, \quad g_{22} = \frac{\partial \mathbf{r}}{\partial v} \cdot \frac{\partial \mathbf{r}}{\partial v}. \quad (4.8)$$

Equation (4.6) actually defines half of the CRT BF. By defining the positions of the vertices of transformation (4.4), one can properly pair the two halves to form the basis function (Fig. 4.4).

The surface gradient of a scalar function and the surface divergence of a vector function of the forms

$$\phi = \phi(u, v) \quad (4.9)$$

and

$$\mathbf{f}(u, v) = f_u \frac{\partial \mathbf{r}}{\partial u} + f_v \frac{\partial \mathbf{r}}{\partial v}, \quad (4.10)$$

respectively, are given as

$$\nabla_s \phi = g^{11} \frac{\partial \phi}{\partial u} \frac{\partial \mathbf{r}}{\partial u} + g^{12} \frac{\partial \phi}{\partial u} \frac{\partial \mathbf{r}}{\partial v} + g^{21} \frac{\partial \phi}{\partial v} \frac{\partial \mathbf{r}}{\partial u} + g^{22} \frac{\partial \phi}{\partial v} \frac{\partial \mathbf{r}}{\partial v} \quad (4.11)$$

and

$$\begin{aligned} \nabla_s \cdot \mathbf{f} &= g^{11} \frac{\partial \mathbf{f}}{\partial u} \cdot \frac{\partial \mathbf{r}}{\partial u} + g^{12} \frac{\partial \mathbf{f}}{\partial u} \cdot \frac{\partial \mathbf{r}}{\partial v} + g^{21} \frac{\partial \mathbf{f}}{\partial v} \cdot \frac{\partial \mathbf{r}}{\partial u} + g^{22} \frac{\partial \mathbf{f}}{\partial v} \cdot \frac{\partial \mathbf{r}}{\partial v} \\ &= \frac{1}{\sqrt{g}} \left( \frac{\partial(f_u \sqrt{g})}{\partial u} + \frac{\partial(f_v \sqrt{g})}{\partial v} \right) \end{aligned} \quad (4.12)$$

where  $g^{ij}$  are the corresponding elements of the inverse of the metric tensor of differential geometry.

With the definitions given above, the divergence of the basis function can be found as

$$\nabla_s \cdot \mathbf{b}(\mathbf{r}) = \frac{1}{\sqrt{g(u, v)}}. \quad (4.13)$$

The surface charge in each subdomain is found to be

$$\sigma ds = \frac{i}{\omega} \nabla_s \cdot \mathbf{b} \sqrt{g(u, v)} dudv, \quad (4.14)$$

which is constant in the parametric space ( $\sigma ds/dudv$ ). It is proven below that the current density across the common edge per unit parameter is independent of the geometry. Thus, there is no line-charge accumulation on the common edge. The unit vector parallel to the common edge and the unit vector perpendicular to the common edge are given as

$$\hat{t}_{\parallel} = \frac{1}{\sqrt{g_{22}}} \frac{\partial \mathbf{r}}{\partial v} \quad (4.15)$$

and

$$\hat{t}_{\perp} = \hat{t}_{\parallel} \times \hat{n} = \frac{1}{\sqrt{g g_{22}}} \left[ g_{22} \frac{\partial \mathbf{r}}{\partial u} - g_{12} \frac{\partial \mathbf{r}}{\partial v} \right]. \quad (4.16)$$

Using Eqs. (4.6) and (4.16), the normal component of the basis function across the edge can be found to be

$$\hat{t}_{\perp} \cdot \mathbf{b} = \frac{1}{\sqrt{g_{22}(u=1, v)}}. \quad (4.17)$$

Since the denominator is the differential length along the common edge, the current density across the edge per unit parameter is independent of the rest of the geometry. Therefore, the normal components of the two halves of the RT

BFs on the common edge are equal, which means that the two halves can be paired properly to form the basis function with continuous normal component at the common edge.

CRT BFs defined on rectangular subdomains on Bézier patches were implemented for the solution of scattering problems involving scatterers modeled by meshes of connected Bézier patches. The surface tangents needed can be easily computed using the chain rule of differentiation and the properties of the Bernstein polynomials, such as

$$\frac{\partial}{\partial s} B_i^n(s) = n [B_{i-1}^{n-1}(s) - B_i^{n-1}(s)]. \quad (4.18)$$

Both  $B_{i-1}^{n-1}(s)$  and  $B_i^{n-1}(s)$  are already computed in the calculation of  $\mathbf{r}(u, v)$ , therefore, no extra effort is needed for the calculation of the surface tangents, which are used in the definition of the BFs.

## 4.4 Curved RWG (CRWG) Basis Functions

A curved triangular subdomain, on the surface on which the CRWG BF is defined, can be considered as a mapping of a triangular subdomain in the  $(s, t)$  parametric space, which, in turn, is the mapping of the unit triangle in the  $(u, v)$  parametric space into the  $(s, t)$  parametric space.

With the transformation

$$\mathbf{r}_a = u(\mathbf{r}_1 - \mathbf{r}_3) + v(\mathbf{r}_2 - \mathbf{r}_3) + \mathbf{r}_3 \quad (4.19)$$

subject to the condition

$$u + v \leq 1, \quad (4.20)$$

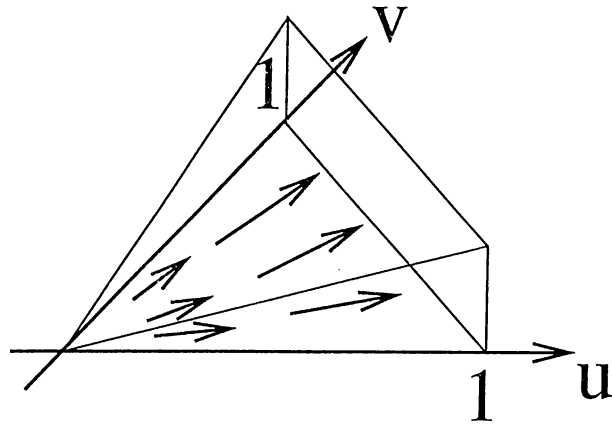


Figure 4.5: CRWG BF defined on the unit triangle in the parametric space.

the unit triangle of the  $(u, v)$  parametric space is mapped to a triangular subdomain in the  $(s, t)$  parametric space, where  $\mathbf{r}_i$  are the  $(s, t)$  coordinates of the three vertices of the triangular subdomain. With the patch transformation, the triangular subdomain in the  $(s, t)$  space is mapped to the curved triangular subdomain on the patch in real space.

When quadratic triangular surfaces are used to model the scatterer, the unit triangle of the  $(u, v)$  domain can be directly mapped to a quadratic triangle in the real space defined by 6 points. The parametric representation of the patch is

$$\mathbf{r}(u, v) = \mathbf{a}_0 + \mathbf{a}_1 u + \mathbf{a}_2 v + \mathbf{a}_3 uv + \mathbf{a}_4 u^2 + \mathbf{a}_5 v^2. \quad (4.21)$$

With this transformation, the subdomain supporting half of a CRWG BF on the patch is formed from the unit triangle of the  $(u, v)$  domain.

The CRWG BFs can now be defined on the  $(u, v)$  domain very simply [4] as

$$\mathbf{b}(\mathbf{r}) = \frac{1}{\sqrt{g(u, v)}} \left( u \frac{\partial \mathbf{r}}{\partial u} + v \frac{\partial \mathbf{r}}{\partial v} \right), \quad (4.22)$$

whose divergence can be formulated to be

$$\nabla_s \cdot \mathbf{b}(\mathbf{r}) = \frac{2}{\sqrt{g(u, v)}} \quad (4.23)$$

Equation (4.22) actually defines half of the CRWG BF. By defining the positions of the vertices of transformation (4.19), one can properly pair the two halves to form the BF.

The surface charge in each subdomain is found to be

$$\sigma ds = \frac{i}{\omega} \nabla_s \cdot \mathbf{b} \sqrt{g(u, v)} dudv, \quad (4.24)$$

which is constant in the parametric space ( $\sigma ds/dudv$ ). The current density across the common edge per unit parameter is independent of the geometry, as proven below. Thus there is no line charge accumulation on the common edge. The unit vector parallel to the common edge and the unit vector perpendicular to the common edge are given as

$$\hat{t}_{\parallel} = \frac{1}{\sqrt{g_{11} + g_{22} - 2g_{12}}} \left( \frac{\partial \mathbf{r}}{\partial u} - \frac{\partial \mathbf{r}}{\partial v} \right) \quad (4.25)$$

and

$$\hat{t}_{\perp} = \hat{t}_{\parallel} \times \hat{n} = \frac{1}{\sqrt{g(g_{11} + g_{22} - 2g_{12})}} \left[ (g_{22} - g_{12}) \frac{\partial \mathbf{r}}{\partial u} + (g_{11} - g_{12}) \frac{\partial \mathbf{r}}{\partial v} \right] \quad (4.26)$$

Using Eqs. (4.22) and (4.26), the normal component of the basis function across the edge can be found to be

$$\hat{t}_{\perp} \cdot \mathbf{b} = \frac{1}{\sqrt{g_{11} + g_{22} - 2g_{12}}}. \quad (4.27)$$

Since the denominator is just the differential length along the common edge, the current density across the edge per unit parameter is independent of the

rest of the geometry. For two triangular subdomains sharing a common edge, the normal components of the two halves of the CRWG BF are equal, therefore, there is no line charge accumulation at the common edge.

CRWG BFs defined on quadratic triangular subdomains defined by 6 discrete points in space that are on a topologically triangular curve are implemented for the solution of scattering problems involving scatterers triangulated by quadratic triangles.

## 4.5 First-Order RT Basis Functions

RT BFs allow a piecewise (PW) continuous representation of the surface current in the direction of current flow and a PW constant representation in the transverse direction. A natural extension of RT BFs are the first-order (linear) RT BFs (LinRT BFs). They allow a PW continuous representation of the surface current in the direction of current flow and a PW linear representation in the transverse direction. In the parametric  $(u, v)$  space, they can be simply defined as

$$\mathbf{f}_1(u, v) = \frac{1}{\sqrt{g(u, v)}} u(1-v) \frac{\partial \mathbf{r}(u, v)}{\partial u}, \quad (4.28)$$

$$\mathbf{f}_2(u, v) = \frac{1}{\sqrt{g(u, v)}} u v \frac{\partial \mathbf{r}(u, v)}{\partial u} \quad (4.29)$$

and

$$\mathbf{f}(u, v) = a \mathbf{f}_1(u, v) + b \mathbf{f}_2(u, v) \quad (4.30)$$

with divergences

$$\nabla \cdot \mathbf{f}_1(u, v) = \frac{1}{\sqrt{g(u, v)}} (1-v), \quad (4.31)$$

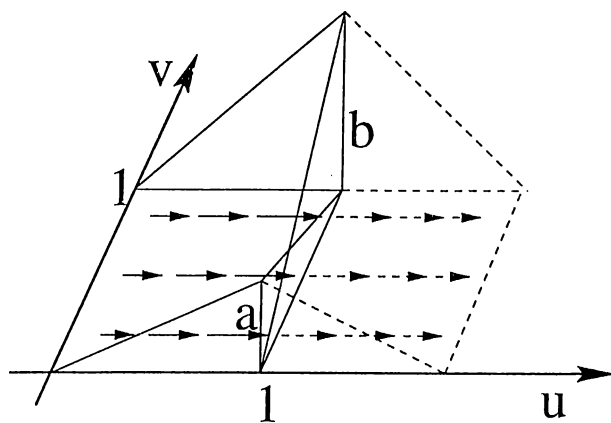


Figure 4.6: First-order rooftop basis functions defined on the  $(u, v)$  parametric space.

$$\nabla \cdot \mathbf{f}_2(u, v) = \frac{1}{\sqrt{g(u, v)}} v \quad (4.32)$$

and

$$\nabla \cdot \mathbf{f}(u, v) = \frac{1}{\sqrt{g(u, v)}} (a(1-v) + bv), \quad (4.33)$$

respectively, on the same parametric domain. They are depicted in Fig 4.6. The above definitions are for half of the LinRT BF. By properly pairing two subdomains the LinRT BF associated with the common edge can be formed on them. Further continuity constraints can be imposed to force a PW continuous current approximation in the direction transverse to the direction of current flow.

These BFs are implemented for the scattering problem involving a flat patch as outlined in Chapter 5. The results obtained and presented in Chapter 5 are incorrect. A close investigation of these BFs using the topological properties of the rectangular mesh of the flat patch reveals that the LinRT BFs are not capable of properly modeling the induced surface charge, which is implicitly modeled by the divergence of the BF. This leads to a very important and

intuitive idea: The basis functions used must also be capable of representing the induced surface charge density modeled by the divergence of the BFs, along with the induced surface current density. Due to this observation, these BFs are not used in the formulations and implementations for scattering problems involving arbitrary geometries.

Other higher-order BFs on triangular and rectangular subdomains are reported in the literature [4, 21, 22, 23, 24]. Some of them are proven not to be capable of representing the surface charge density properly [9]. In this thesis only CRT BFs and CRWG BFs are employed in the MoM formulations of scattering problems involving arbitrary scatterers.



## Chapter 5

# Scattering from Canonical and Complicated Targets

The MoM and the FMM formulations of the electromagnetic scattering problems using quadratic triangular patch modeling and Bézier patch modeling are implemented. Also the MoM solutions of scattering from a perfect-electric-conductor (PEC) sphere are implemented using the exact model of the sphere with CRWG BFs and CRT BFs. The results obtained are compared on the basis of geometry modeling. It is shown that accurate geometry models increase the solution accuracy, hence the problem size can be reduced using better geometry models for the scatterers.

In this chapter, the solutions of some sample scattering problems will be presented. For sample problems involving curved surfaces, the results of different geometry-modeling techniques will be compared. Analytical results will

also be given when possible. All sample problems are solved for different discretizations in order to ensure the convergence of the solutions. Mostly three geometry-modeling schemes, namely, flat triangulations, quadratic triangulations, and Bézier-patch formulation will be contrasted for the sphere. Especially, the problem of scattering from a PEC sphere constitutes a benchmark in order to investigate the effect of the geometry model on the solution. It is a doubly-curved canonical scatterer for which the exact parametric geometry model exists. The closed-form solution to the problem also exists, therefore, the results obtained, including the induced surface currents and the scattered far-fields, can be compared with the analytical results. For these reasons, this problem is investigated in detail.

The implementation of quadratic triangular patch formulation is integrated with the commercially available CAGD program, MSC/ARIES. The triangulation of the scatterer is obtained from this program and the induced surface current results obtained by executing the code that were developed are input back to the program where the user can visualize the solution.

The MoM and the FMM solutions will also be compared on the basis of accuracy, solution time, and memory requirements. Some of the problems are solved for large number of unknowns in order to demonstrate the capabilities of the FMM.

## 5.1 Flat Patch

This is the first sample problem studied because of the simplicity of the geometry. The scatterer is an infinitely thin flat square patch lying on the  $x-y$  plane

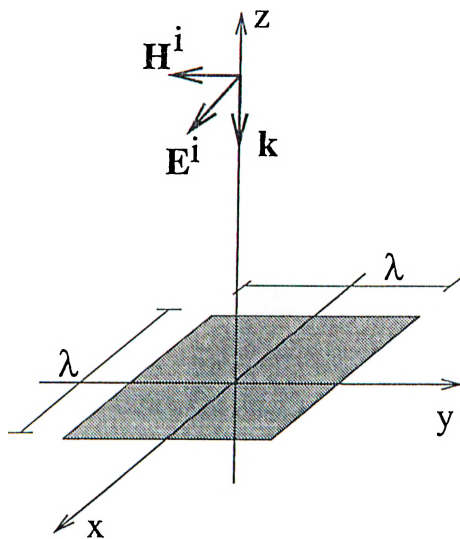


Figure 5.1: Flat PEC patch illuminated by a plane wave.

centered at the origin as depicted in Fig. 5.1. The patch is illuminated by a plane wave propagating in the negative  $z$  direction.

The surface current density induced on the patch and the scattered far-field are investigated using the RT BFs, the LinRT BFs, and the CRWG BFs, which become identical to flat RWG BFs for this geometry. Using the LinRT BFs seems to be legitimate choice for the current expansion, but we will present some interesting results obtained with them later in this section. Also, the current results obtained using flat RWG BFs are given. The discretization scheme for RT BFs is depicted in Figure 5.2.

Figure 5.3(a) shows the component of the induced surface current that is in the same direction as the incident electric field, which may be called the copolar current. The result is obtained using the RT BFs and normalized with the magnitude of the incident magnetic field. Figure 5.3(b) shows the crosspolar component of the induced surface current, whose direction of flow is perpendicular to the incident field polarization. The edge singularities in

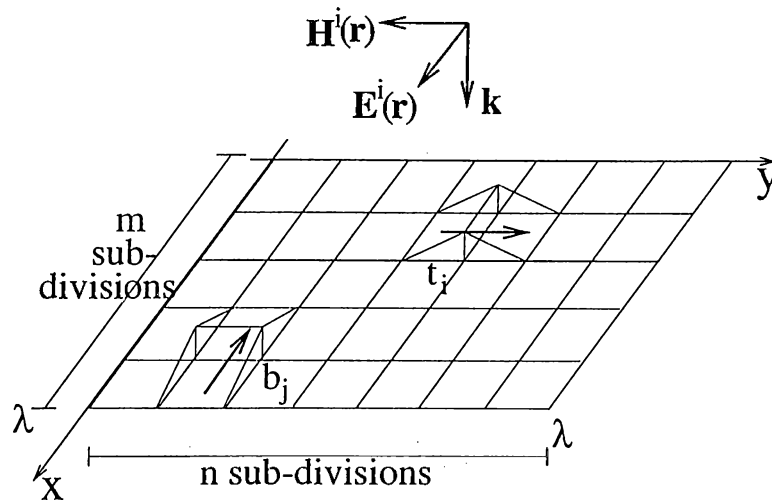


Figure 5.2: Discretization of the flat patch.

both components are resolved. The decoupling of the two perpendicular components by the RT BFs also turned out to be desirable for this problem since the magnitudes of the two current components are very different. This feature does not exist in the (flat or curved) RWG BFs, i.e., on one triangular subdomain of the BF, the BF is designed to be a vector function with two nonzero components. As seen in Fig. 5.3, near the  $y = 0$  and  $y = \lambda$  edges, the copolar current takes large values in magnitude, and the crosspolar current is smaller compared to the copolar current. In the middle region of the patch, again the copolar current has large values and crosspolar current has smaller values. The RT BFs, by decoupling these two components, can resolve the copolar and crosspolar currents very well. Figure 5.3(c) and (d) show the variation of the total induced surface charge, which is calculated with the aid of the continuity equation. It should be noted that the RT BFs used to model the induced surface current density results in a PW constant modeling of the induced surface charge density.

In Figs. 5.4(a) and (b) the induced surface current computed using flat

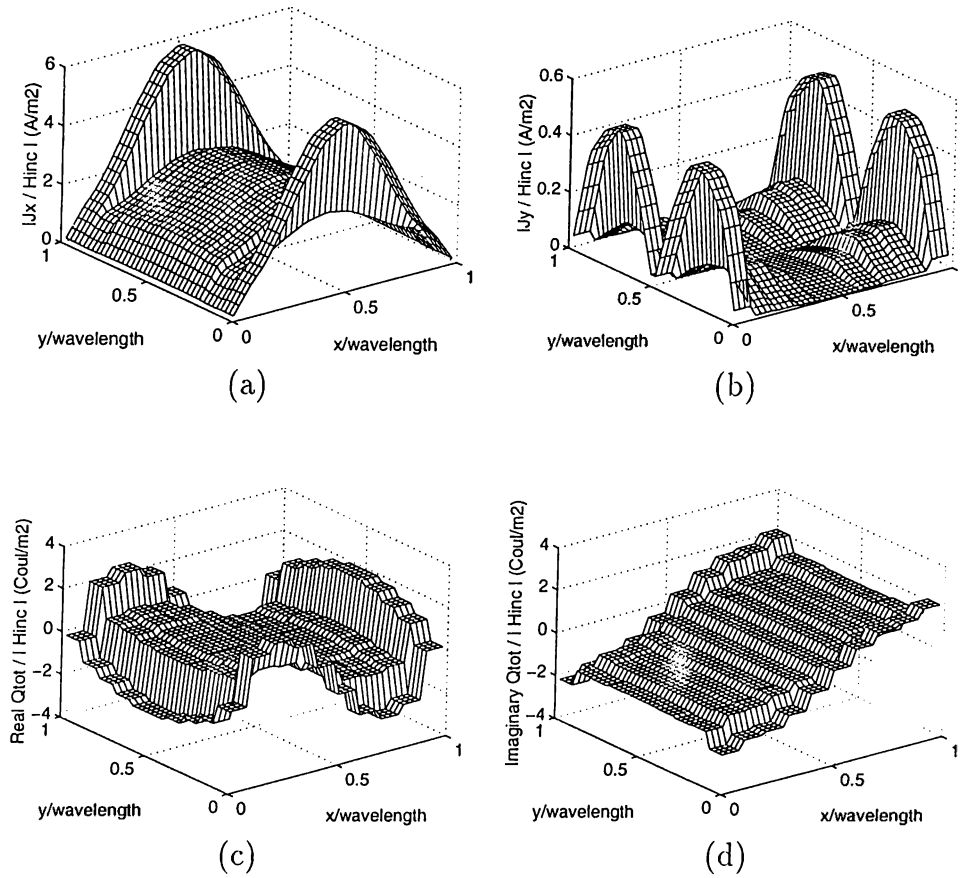


Figure 5.3: The induced current and charge densities on the flat patch. The patch is discretized into  $10 \times 10$  divisions and the RT BFs on the internal edges are used for the expansion. (a) Magnitude of the copolar induced current. (b) Magnitude of the crosspolar current. (c) Real part of the divergence of the induced current. (d) Imaginary part of the divergence of the induced current. The current results are normalized with the magnitude of the incident magnetic field, and the divergence of the current is presented as the charge distribution.

RWG BFs is shown. Figure 5.4(c) and (d) depict the induced surface charge density. The resemblance to the RT BF solutions is very well, except for the crosspolar-current result. The irregularities in the solution obtained using the RWG BFs can be explained using the above argument. Each RWG BF is defined over two triangular subdomains. On the subdomains they are defined, they have two nonzero components. If one component of the induced current tends to large values and the other to small values in one subdomain, the MoM solution inevitably results in such irregular current solutions, because the solution is an optimization procedure which minimizes the average error on the patch and the basis function does its job as good as it can. The MoM solution makes a trade-off between the two components of the BF, one of which tends to get larger and the other tends to get smaller, both of which cannot be satisfied at the same time. Although the crosspolar current seems very noisy, the RWG BFs are shown to perform as good as the RT BF when the boundary-condition error on the patch is considered [25].

RWG BFs also approximate the induced surface charge density by a PW constant distribution as depicted in Figs. 5.4(c) and (d). The results agree with the RT BF solutions.

Figure 5.5 shows the current and charge solutions for the flat-patch problem obtained with a finer discretization of the geometry using the RT BFs. The convergence of the solutions can be observed. Another point to notice is the better resolution of the edge singularities.

The RT BFs model the unknown surface current density in a PW continuous fashion in the direction of the current flow and in a PW constant fashion in the transverse direction. Can better BFs be used for the current expansion

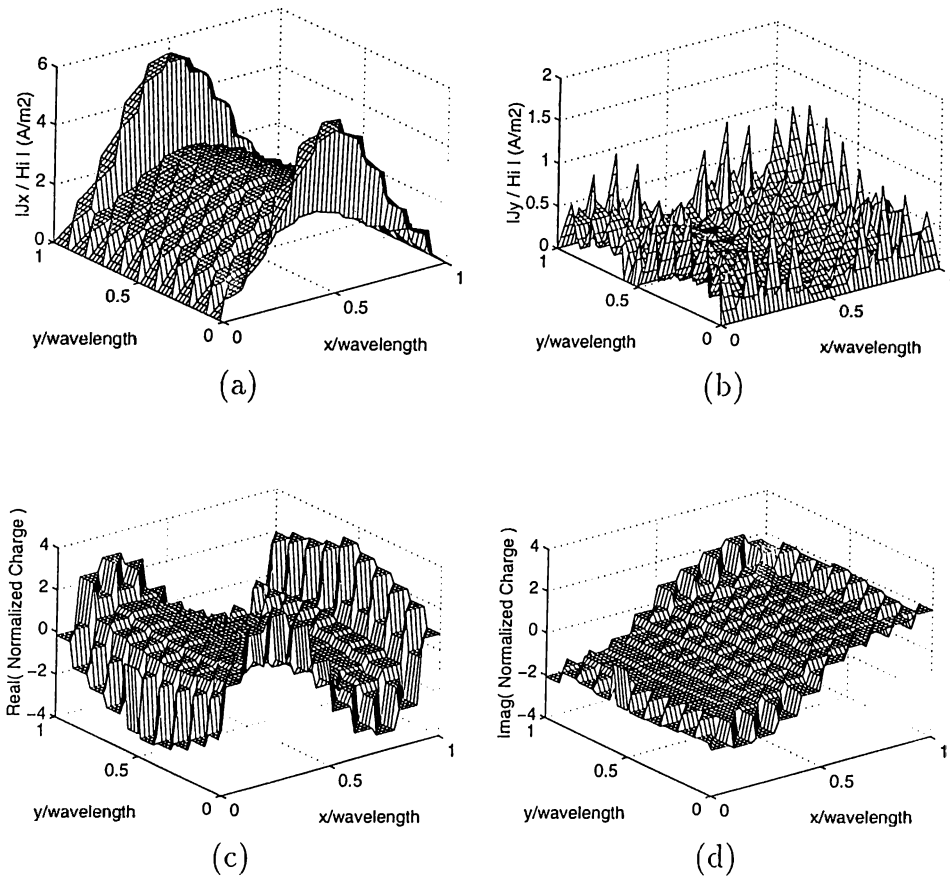


Figure 5.4: The induced current and charge densities on the flat patch. The patch is triangulated into 200 subdomains and the RWG BF's on the internal edges are used for the expansion. (a) Magnitude of the copolar induced current. (b) Magnitude of the crosspolar current. (c) Real part of the divergence of the induced current. (d) Imaginary part of the divergence of the induced current. The current results are normalized with the magnitude of the incident magnetic field, and the divergence of the current is presented as the charge distribution.

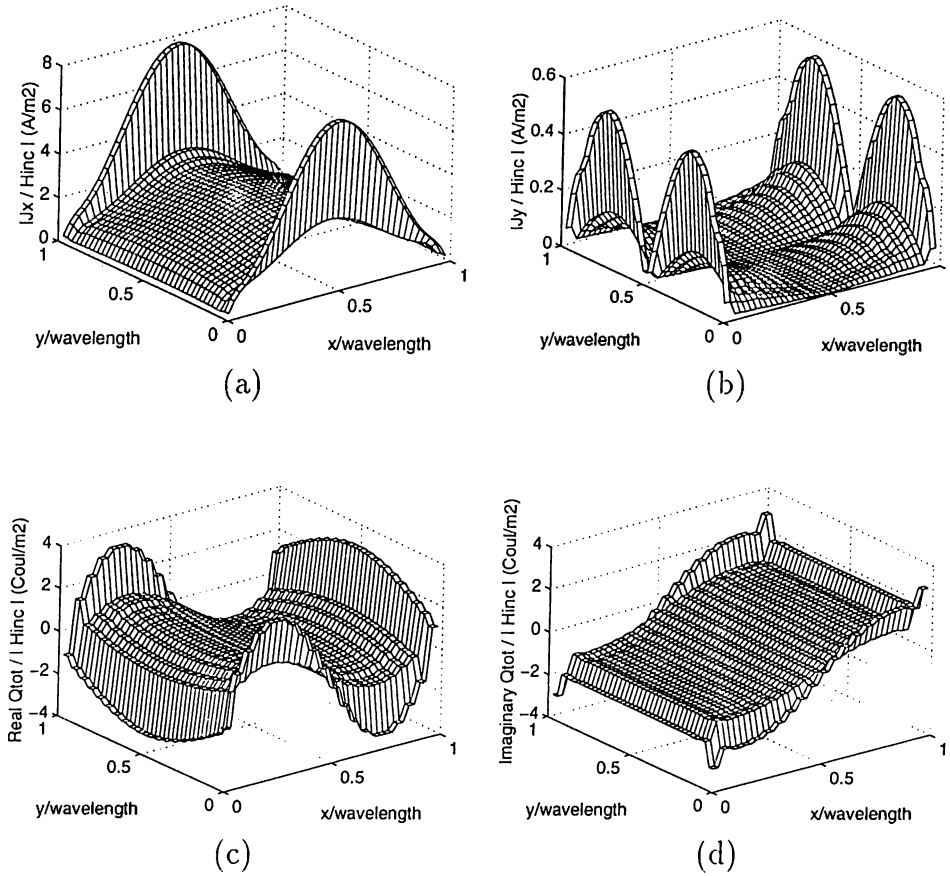


Figure 5.5: The induced current and charge densities on the flat patch. The patch is discretized into  $20 \times 20$  divisions and the RT BF's on the internal edges are used for the expansion. (a) Magnitude of the copolar induced current. (b) Magnitude of the crosspolar current. (c) Real part of the divergence of the induced current. (d) Imaginary part of the divergence of the induced current. The current results are normalized with the magnitude of the incident magnetic field, and the divergence of the current is presented as the charge distribution.



so that more continuity constraints be imposed to get better results? Some higher-order BFs are reported in the literature [4, 21, 22, 23, 24]. The LinRT BFs defined in Chapter 4 are implemented. These LinRT BFs model the current PW bilinearly and they model the charge PW linearly. If continuity of the tangential component of the BF on the internal vertices of the patch is imposed, a new group of BFs is obtained which we called linear continuous rooftop (LinContRT) BFs. They are identically the same basis functions as the pyramidal basis functions defined on quadruples of rectangular subdomains.

Figure 5.6 depicts the induced surface current density computed using the LinContRT BFs and the induced surface charge density calculated thereafter. The copolar current seems to be acceptable, but the crosspolar component is unexpectedly incorrect. The situation obtained with a finer discretization is no better (Fig. 5.7). Figures 5.8 and 5.9 show the results obtained by using LinRT BFs. The results are even worse. A close investigation of the problem resulted in a very important and intuitive idea: The basis function chosen for the expansion of the surface current density must also be capable of representing the surface charge distribution. Considering the degrees of freedom (DoFs) supplied by the current expansion and the DoFs needed by the charge approximation, it is proven [9] that the LinRT BFs and LinContRT BFs are not suitable basis functions for this problem.

In Figure 5.10, the copolar and crosspolar components of the boundary-condition error (BCE), on the patch for two different solutions belonging to two different discretizations are plotted. The BCE is seen to be satisfied over the surface of the patch except at the  $x = 0$  and  $x = \lambda$  edges for the copolar BCE and at the other two edges for the crosspolar BCE. This is because the

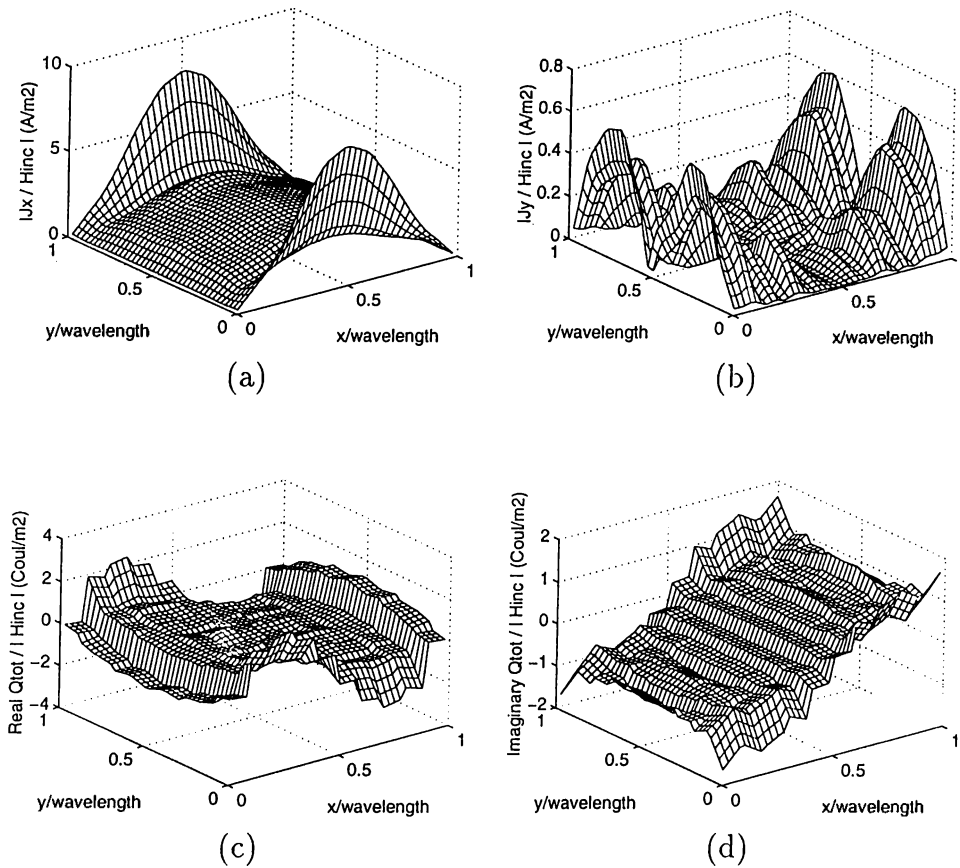


Figure 5.6: The induced current and charge densities on the flat patch. The patch is discretized into  $10 \times 10$  divisions and two LinRT BF's on the internal edges are used for the expansion. Transverse continuity is imposed at each internal vertex. (a) Magnitude of the copolar induced current. (b) Magnitude of the crosspolar current. (c) Real part of the divergence of the induced current. (d) Imaginary part of the divergence of the induced current. The current results are normalized with the magnitude of the incident magnetic field, and the divergence of the current is presented as the charge distribution.

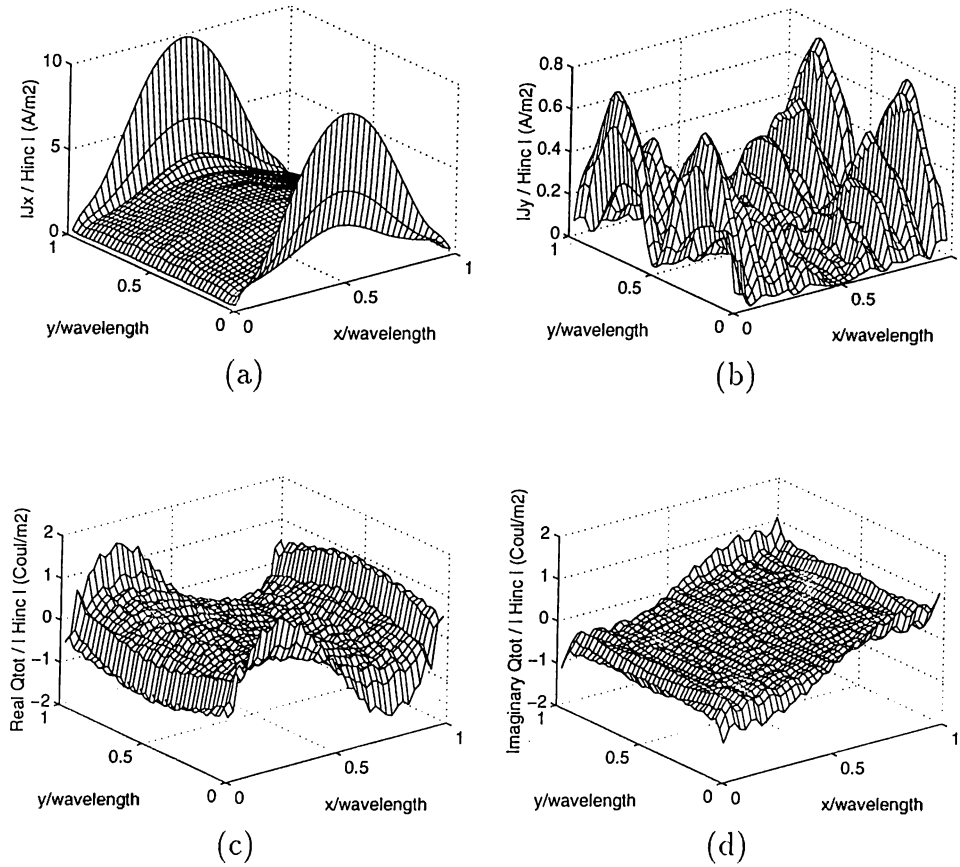


Figure 5.7: The induced current and charge densities on the flat patch. The patch is discretized into  $20 \times 20$  divisions and two LinRT BF's on the internal edges are used for the expansion. Transverse continuity is imposed at each internal vertex. (a) Magnitude of the copolar induced current. (b) Magnitude of the crosspolar current. (c) Real part of the divergence of the induced current. (d) Imaginary part of the divergence of the induced current. The current results are normalized with the magnitude of the incident magnetic field, and the divergence of the current is presented as the charge distribution.

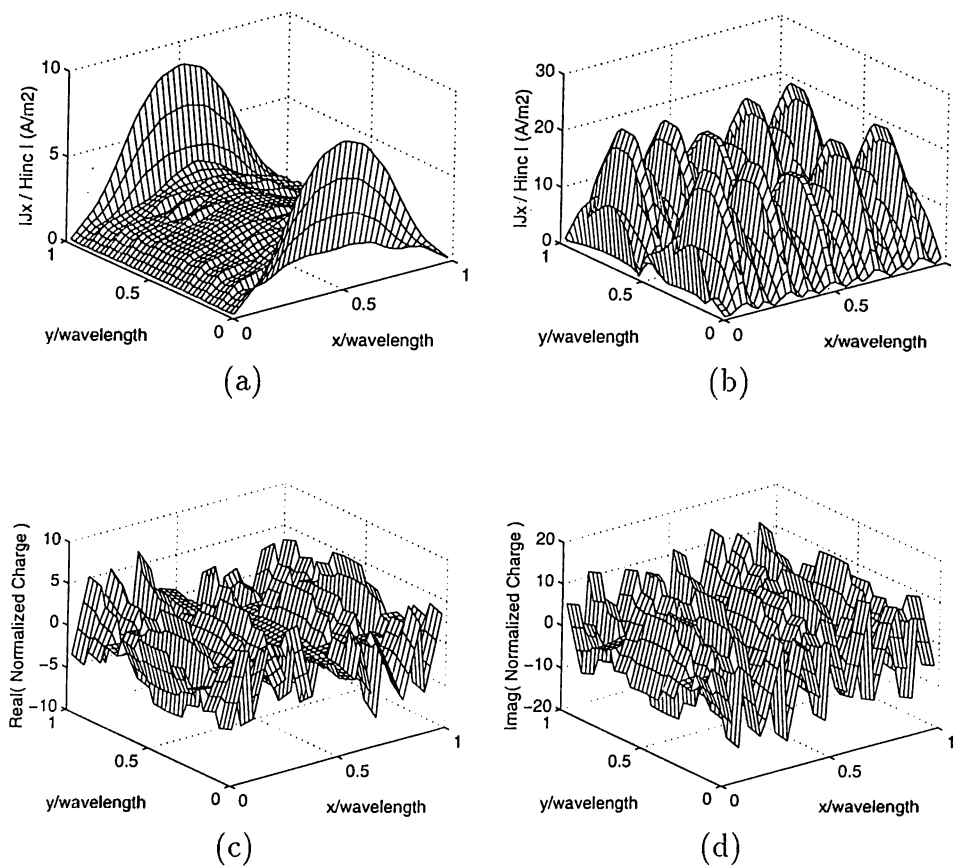


Figure 5.8: The induced current and charge densities on the flat patch. The patch is discretized into  $10 \times 10$  divisions and two LinRT BF's on the internal edges are used for the expansion. (a) Magnitude of the copolar induced current. (b) Magnitude of the crosspolar current. (c) Real part of the divergence of the induced current. (d) Imaginary part of the divergence of the induced current. The current results are normalized with the magnitude of the incident magnetic field, and the divergence of the current is presented as the charge distribution.

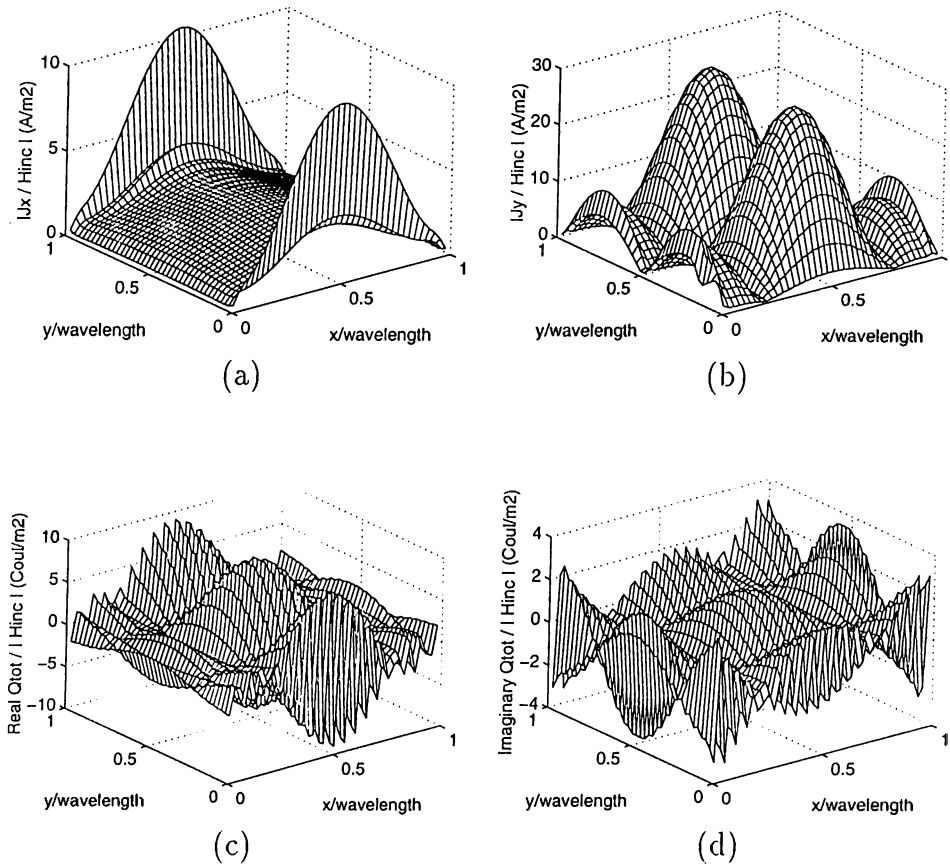


Figure 5.9: The induced current and charge densities on the flat patch. The patch is discretized into  $20 \times 20$  divisions and two LinRT BF's on the internal edges are used for the expansion. (a) Magnitude of the copolar induced current. (b) Magnitude of the crosspolar current. (c) Real part of the divergence of the induced current. (d) Imaginary part of the divergence of the induced current. The current results are normalized with the magnitude of the incident magnetic field, and the divergence of the current is presented as the charge distribution.

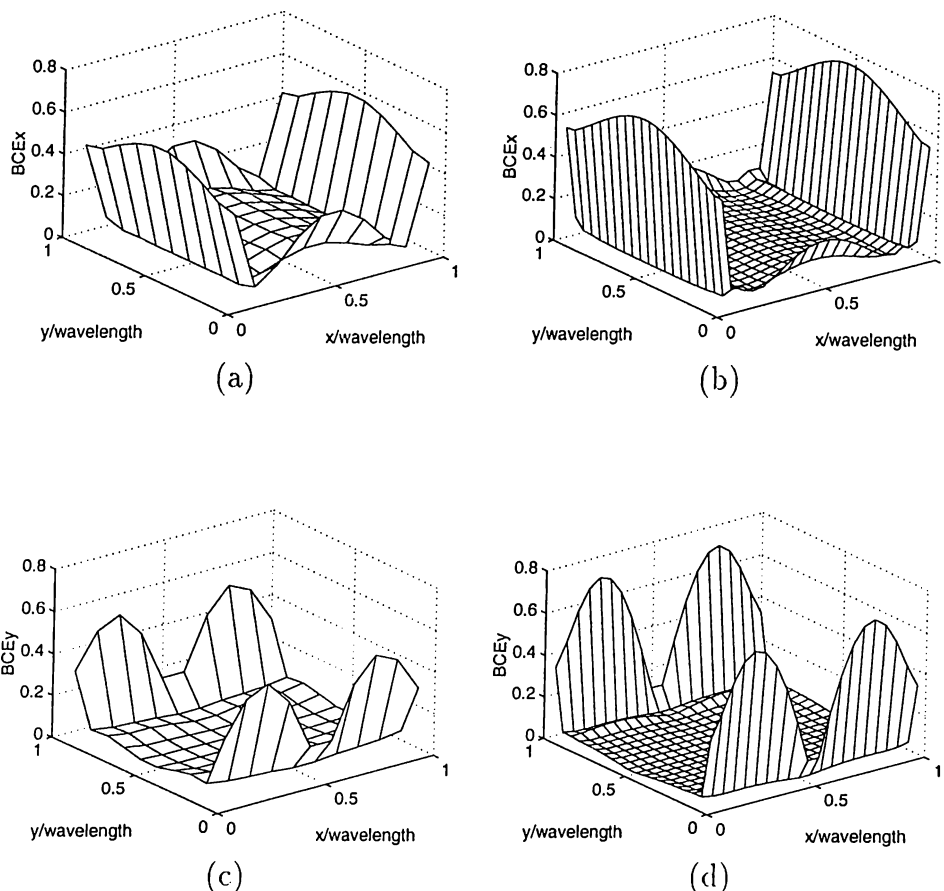


Figure 5.10: Boundary-condition error on the flat patch. The solution is obtained using the RT BFs. (a) Copolar BCE for  $10 \times 10$  discretization. (b) Copolar BCE for  $20 \times 20$  discretization. (c) Crosspolar BCE for  $10 \times 10$  discretization. (d) Crosspolar BCE for  $20 \times 20$  discretization.

copolar and crosspolar unit vectors are not tangential to  $x = 0, \lambda$  and  $y = 0, \lambda$  edges, respectively. Discretizing the original problem can be thought of as enlarging those edges in space, on which the boundary condition need not be satisfied.

Given for comparison and for the demonstration of the incapacibilities of the LinRT BFs and LinContRT BFs, Figs. 5.11 and 5.12 depict the BCE for two different discretizations and for copolar and crosspolar components.

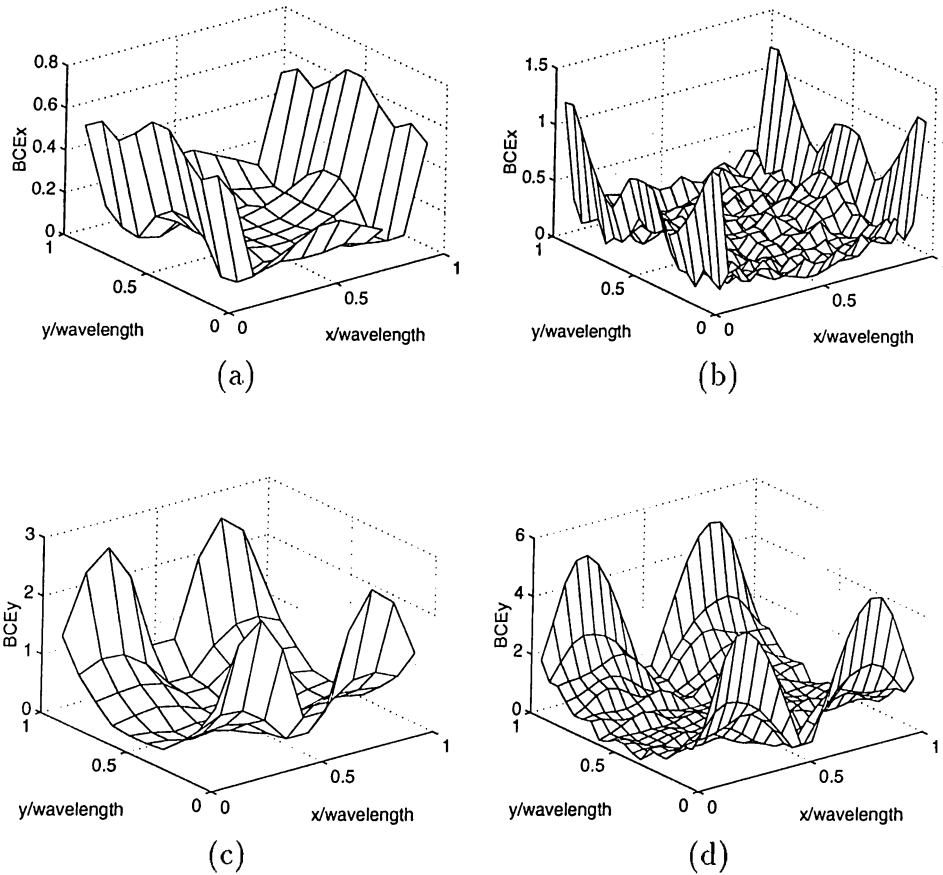
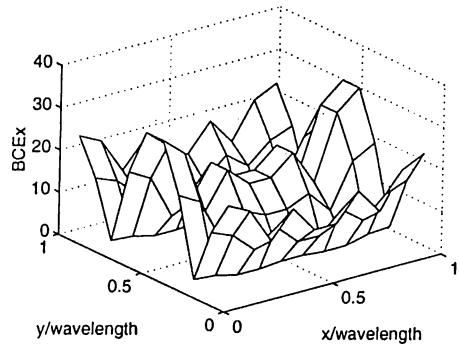
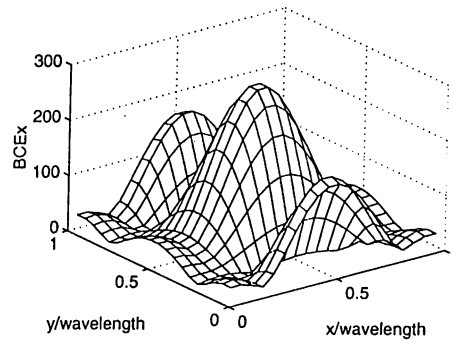


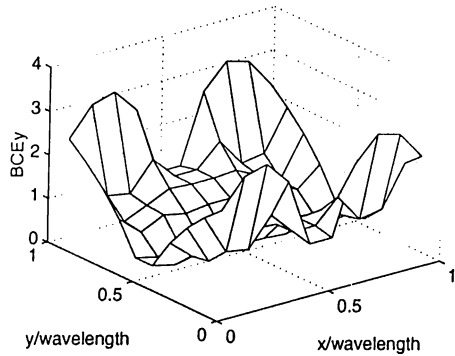
Figure 5.11: Boundary-condition error on the flat patch. The solution is obtained using the transversely continuous LinRT BFs. (a) Copolar BCE for  $10 \times 10$  discretization. (b) Copolar BCE for  $20 \times 20$  discretization. (c) Crosspolar BCE for  $10 \times 10$  discretization. (d) Crosspolar BCE for  $20 \times 20$  discretization.



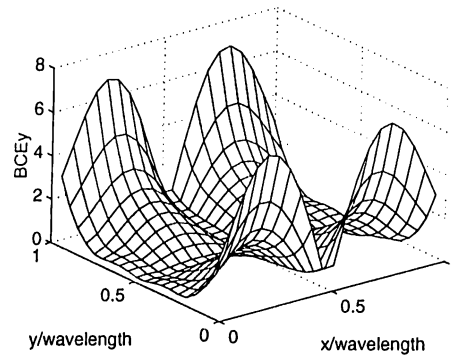
(a)



(b)



(c)



(d)

Figure 5.12: Boundary-condition error on the flat patch. The solution is obtained using the LinRT BFs. (a) Copolar BCE for  $10 \times 10$  discretization. (b) Copolar BCE for  $20 \times 20$  discretization. (c) Crosspolar BCE for  $10 \times 10$  discretization. (d) Crosspolar BCE for  $20 \times 20$  discretization.



A triangulation with the quadratic triangular subdomains obtained from the MSC/ARIES is used with the CRWG BFs<sup>1</sup> and the solution for the induced surface current density is visualized in the MSC/ARIES. This program can make color plots of the magnitude of the induced surface current when the values at the vertices of the triangulation are given. Figure 5.13 shows the magnitudes of the copolar and crosspolar components of the induced surface current as plotted by the MSC/ARIES.

Also, as a comparison between RT BFs and RWG BFs on the patch, the bistatic RCS of a  $2\lambda \times 2\lambda$  patch for the same incident field and on the  $\phi = 0$  cut is shown in Fig. 5.14. The two results are indistinguishable meaning that both the RT BFs and the RWG BFs perform equally well on the flat patch for RCS calculations although there exists differences between the current solutions using the two BFs.

Figure 5.15(a) shows the matrix solution times of the MoM and the FMM. the MoM matrix is solved using direct LU decomposition and using conjugate gradient squared method (CGS). For the FMM solutions the CGS is utilized. For unknown sizes around a few hundreds the FMM outperforms both the MoM solved with LU decomposition and the MoM solved with the CGS. Figure 5.15(b) shows the total problem solution times including the matrix filling times. When total solution time is considered, the FMM is observed to be faster than the standart MoM solution for problem sizes above 200, which is a fairly low number for scattering problems. Figure 5.16 shows the time consumed per iteration for the MoM and the FMM algorithms. The MoM complexity dominates for problem sizes larger than 1000.

---

<sup>1</sup>It should be noted that neither the triangular subdomains nor the BFs are curved for this geometry.

Figure 5.17 depicts the memory required to solve the problem using the MoM and the FMM. The  $O(N^{1.5})$  memory requirement order of the FMM and  $O(N^2)$  memory requirement order of the MoM is clearly observed. For problem sizes above 1000, the MoM memory requirement dominates.

To demonstrate the accuracy and the efficiency of the FMM, Fig. 5.18 depicts two solutions obtained by solving the same problem both with the MoM and with the FMM using the quadratic-triangular-patch models and the Bézier-patch models of the scatterers. The MoM result using the CRWG BFs, shown in Fig. 5.18(a) is obtained in 364 seconds, whereas the FMM solution is obtained in 163 seconds using an iterative solver. The solution of the Bézier-patch model of the flat patch shown in Fig. 5.18(b) is obtained in 433 seconds using the MoM and in 251 seconds using the FMM.

Figure 5.19 shows the bistatic RCS of a  $10\lambda \times 10\lambda$  flat patch illuminated by a  $\theta$ -directed plane wave incident from the direction  $\theta = 135^\circ$ ,  $\phi = 180^\circ$ . About 6.5 unknowns per wavelength are used. This result is obtained using the FMM with the RT BFs and curved RWG BFs, and is presented here to demonstrate the efficiency of the FMM. Note that the direct application of the MoM would result in an  $8000 \times 8000$  system of equations, which would require more than 1 GBytes of memory for its storage and solution. The difference between the RT and the RWG solutions is expected to drop for finer discretizations.

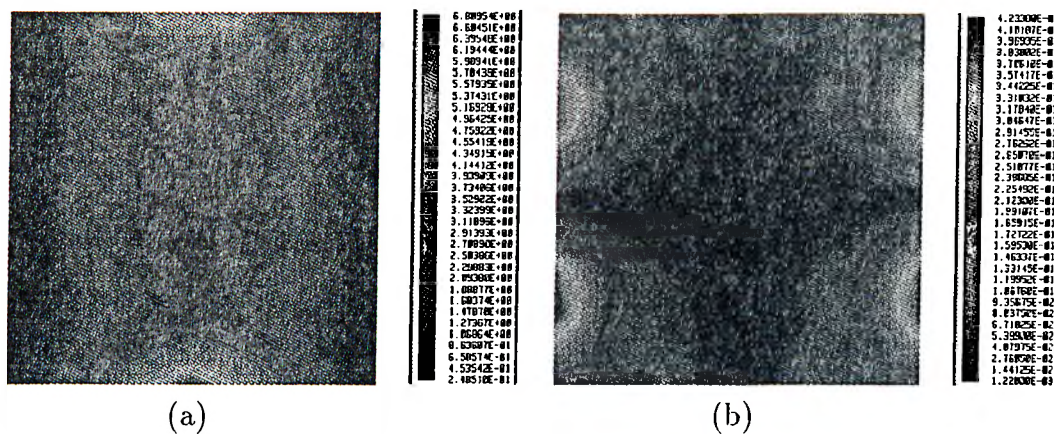


Figure 5.13: (a) Magnitude of the copolar induced current on a  $\lambda \times \lambda$  flat patch. (b) Magnitude of the crosspolar induced current on a  $\lambda \times \lambda$  flat patch. The color plots are generated using the MSC/ARIES.

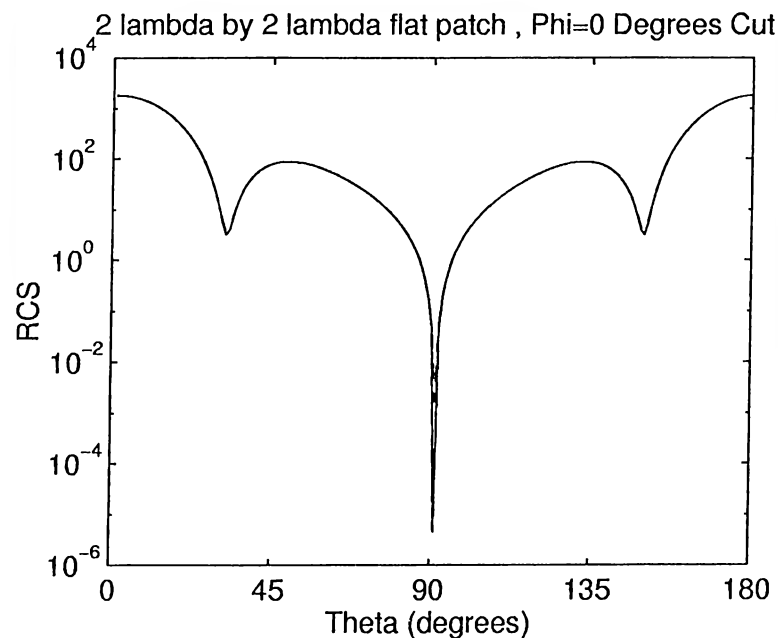


Figure 5.14: Bistatic RCS of a  $2\lambda \times 2\lambda$  flat patch. —  $15 \times 15$  division with 420 RT BF's, --- MSC/ARIES triangulation with 560 RWG BF's.

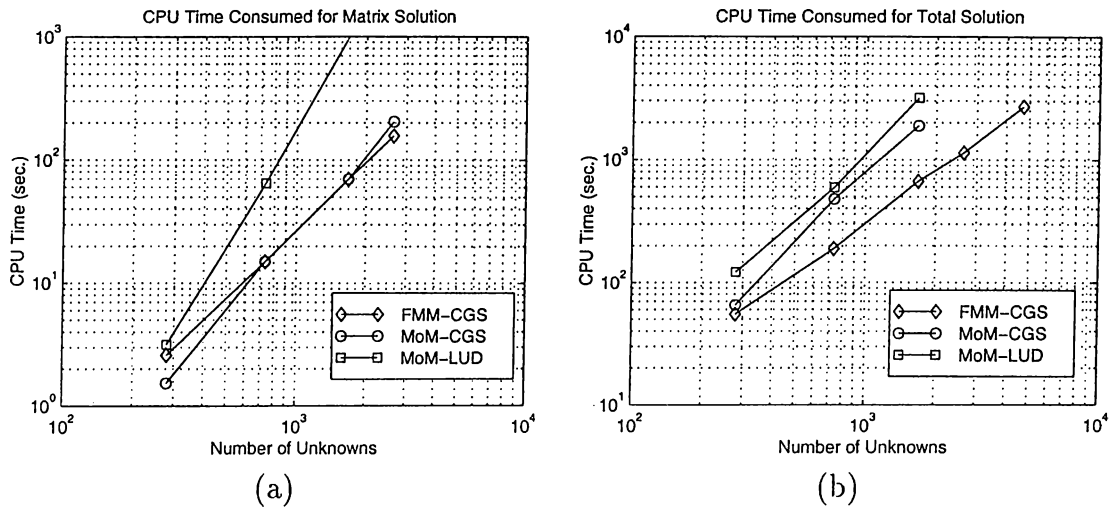


Figure 5.15: Timing comparisons of the MoM and the FMM. (a) The matrix solution times using the MoM with LU decomposition, the MoM with CGS, and the FMM with CGS, (b) The problem solution times using the MoM with LU decomposition, the MoM with CGS, and the FMM with CGS.

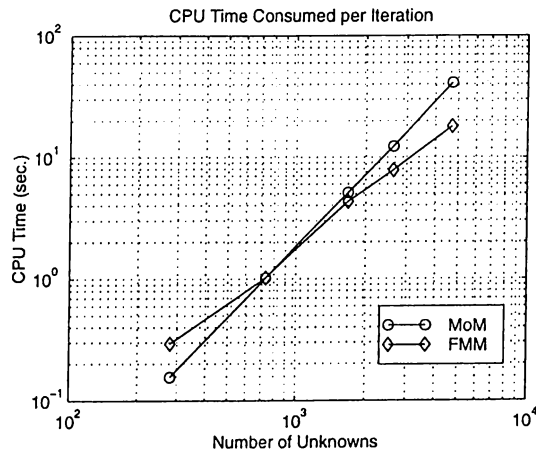


Figure 5.16: CPU time consumed per one iteration of MoM and FMM algorithms. The iterative solution method is CGS.

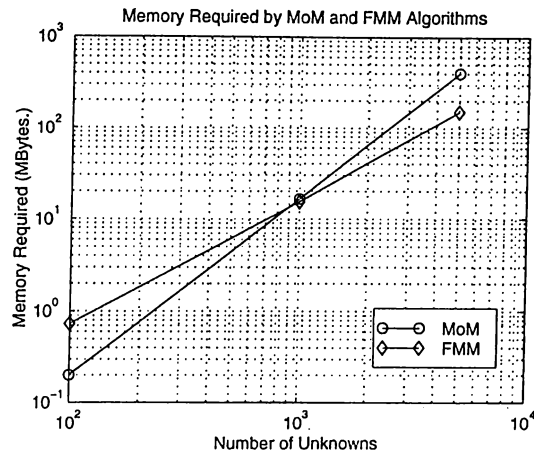


Figure 5.17: Approximate memory requirements of the MoM and the FMM algorithms.

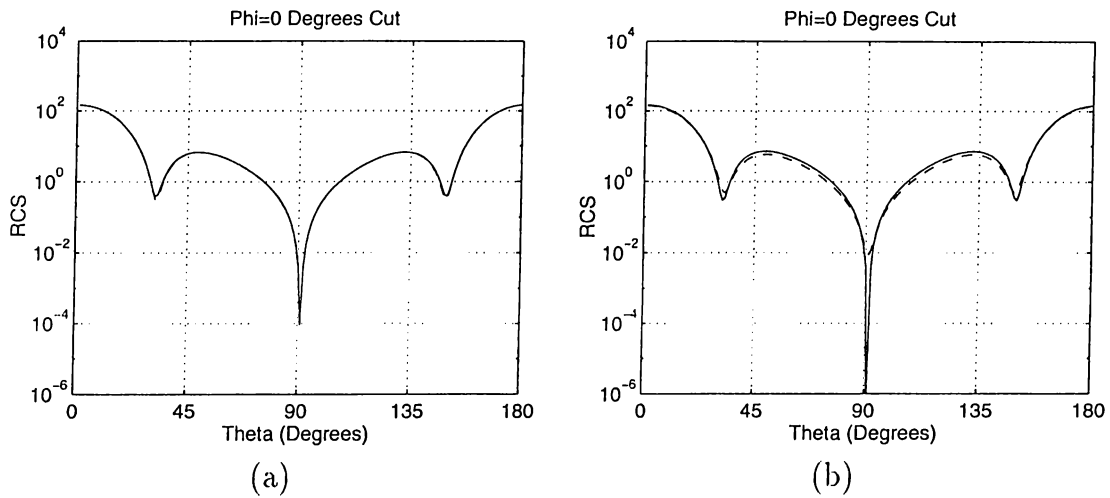


Figure 5.18: Validations of the FMM solutions. (a) Bistatic RCS of a  $2\lambda \times 2\lambda$  flat patch using 736 CRWG BFs, — the MoM solution, -- the FMM solution. (b) Bistatic RCS of a  $2\lambda \times 2\lambda$  flat patch using 760 CRT BFs, — the MoM solution, -- the FMM solution.

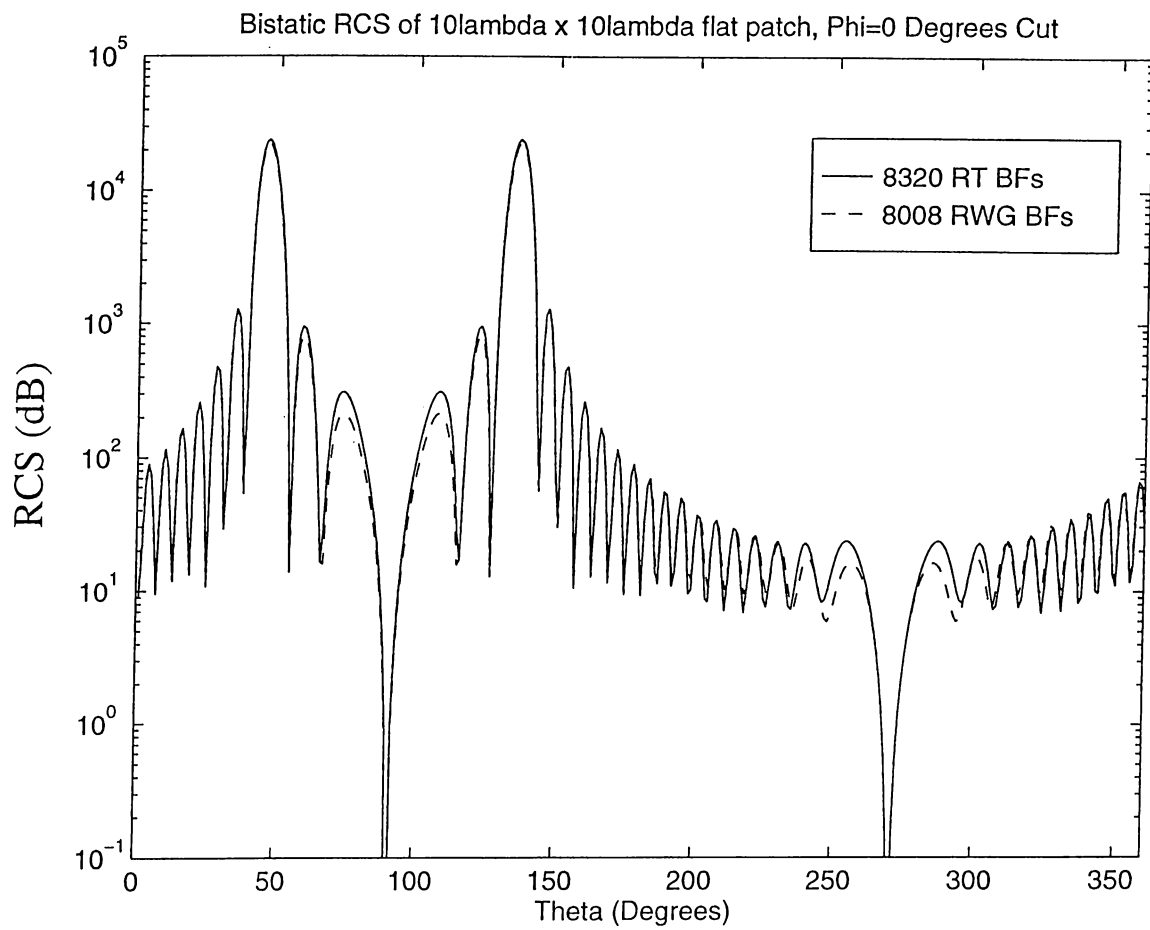


Figure 5.19: Bistatic RCS of a  $10\lambda \times 10\lambda$  flat patch. —  $65 \times 65$  division with 8320 RT BF's, - - MSC/ARIES triangulation with 8008 RWG BF's.

## 5.2 Sphere

This is the most important one of the sample problems investigated. The geometry is canonical and doubly curved. It is an excellent sample to compare various geometry-approximation techniques, since the closed-form solution to the problem also exists. The solution of this problem is obtained using the exact model, flat triangulation, and quadratic triangulation of the sphere. It should be noted that rational Bézier patches can model the sphere exactly. On these models, CRT BFs and flat and CRWG BFs are used. Solutions of the induced current density and the scattered electric field are compared.

In Fig. 5.20, the problem configuration is depicted. The sphere is centered at the origin and the  $x$ -polarized incident plane wave is propagating in the positive  $z$  direction. Mie-series technique [26] is used to obtain a closed-form reference solution for the induced surface current density and the scattered electric field in the far zone. The scattered far-field results are normalized with respect to spherical spread and phase factors. In most of the plots, the reference solution is plotted with a solid line. This solution satisfies the boundary condition on the sphere with an accuracy of one part in thousand. The results are observed and presented on the three principle cuts of the sphere, namely, the  $\theta = 90^\circ$ ,  $\phi = 0^\circ$ , and  $\phi = 90^\circ$  cuts. Some components of the induced current and the far fields are not given on some cuts because they are identically equal to zero on those cuts.

In the following subsections, the results obtained for the sphere by applying different geometry-approximation techniques are presented.

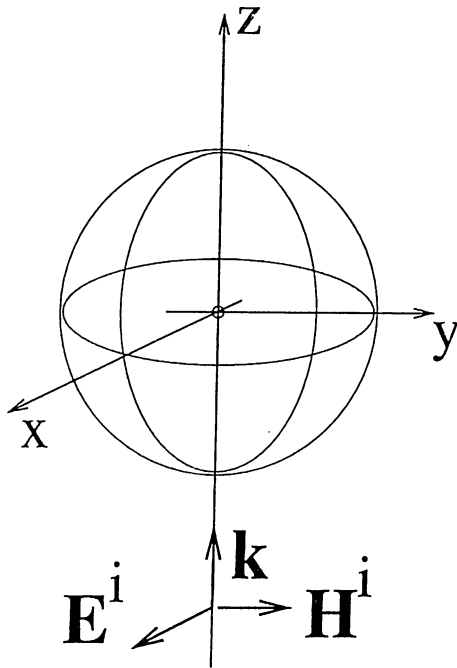


Figure 5.20: A PEC sphere illuminated by a plane wave.

### 5.2.1 Flat Triangulation with RWG BFs

The  $0.2\lambda$ -radius sphere is approximated using flat triangles as shown in Fig 5.21 and the flat RWG BFs are used on pairs of triangles for the expansion of the surface current density. Figure 5.22 shows the solution of the induced surface current for different numbers of BFs used. The convergence of the solutions as the number of unknowns is increased can be observed from the figures. The spikes in the current solution in Fig. 5.22(a) are due to the coupling of the two components of the RWG BF on each triangular subdomain, as mentioned in Section 5.1.

Figure 5.23 shows the scattered field results in the far zone for the same discretizations used to obtain the current results shown in Fig. 5.22. It should be noted that the rapid variations in the current solution is swept out by the far-field transformation and the far-field results are, although not very close to



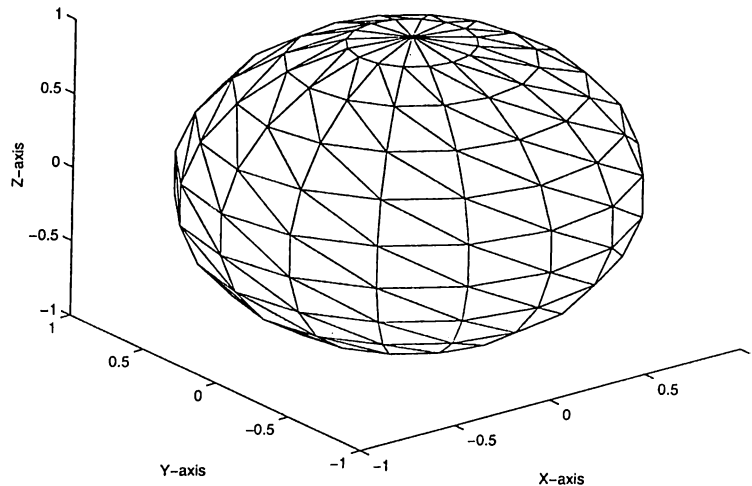


Figure 5.21: Flat triangulation of the sphere.

the exact solution, quite smooth. The error in the scattered far-field results is due in part to the fact that the flat cell model was inscribed within the desired sphere. As observed from the results, to obtain the solution accurately using flat triangulations, one must use a fairly fine triangulation to model the geometry properly. Since the BFs used are defined on these subdomains, this results in the increase of the size of the problem, which is undesirable.

### 5.2.2 Exact Model with CRWG BFs

By projecting each triangular subdomain of the flat triangulation on the sphere surface, a triangulation formed of curved triangular subdomains on the exact model of the sphere can be obtained [27]. This projection can be accomplished by normalizing the position vector  $\mathbf{r}_a$  on the flat triangle with its amplitude. Multiplication of this unit vector by the radius of the sphere gives the position vector  $\mathbf{r}$  which is now on the surface of the sphere, thus the flat triangular

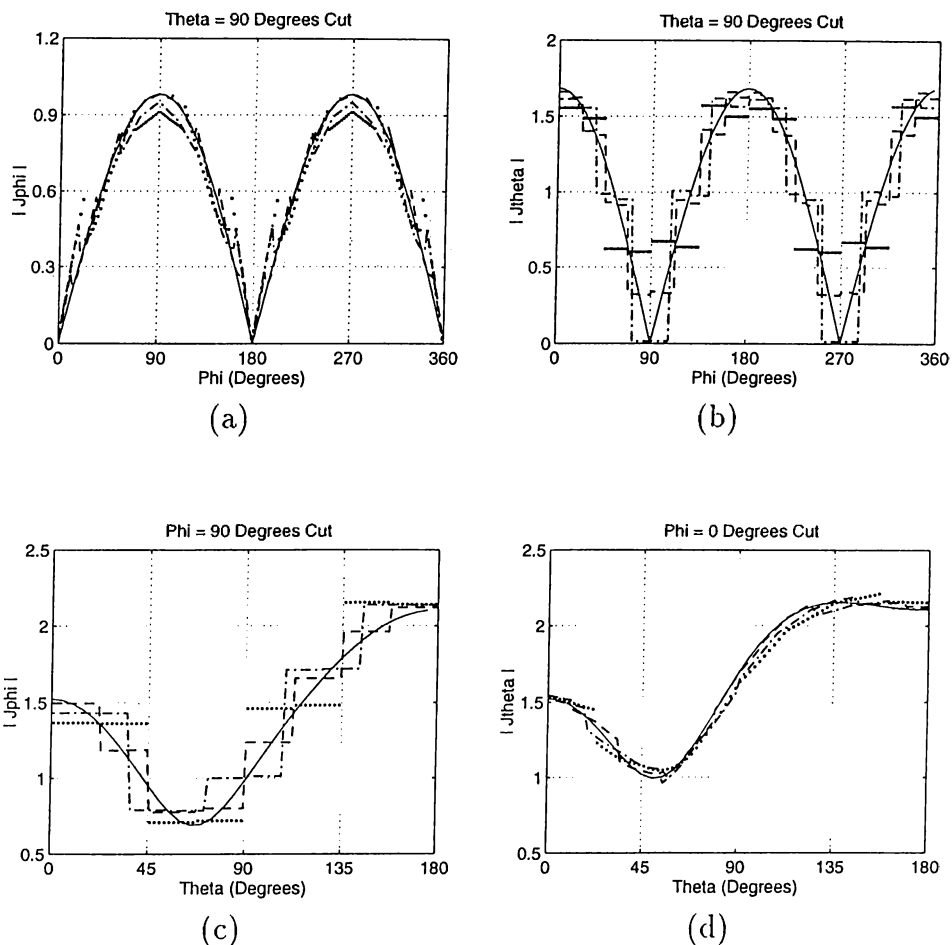


Figure 5.22: Magnitude of the surface current induced on the  $0.2\lambda$ -radius sphere. Flat triangulation of the sphere is used with the flat RWG basis functions. The results are normalized with the magnitude of incident magnetic field and are given on the three principle cuts of the sphere for different discretizations and different numbers of unknowns. — Mie series,  $\cdots$   $7 \times 8$  divisions and 144 unknowns,  $-\cdot-$   $9 \times 10$  divisions and 240 unknowns,  $--$   $11 \times 16$  divisions and 480 unknowns.

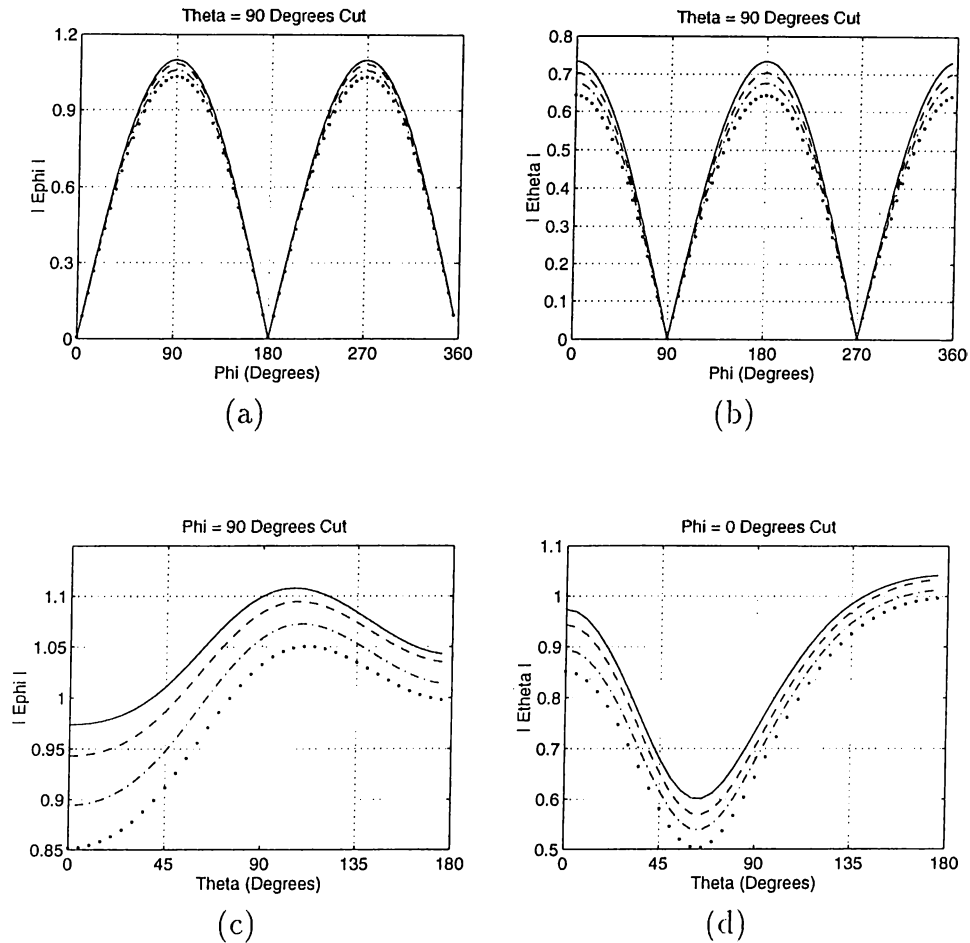


Figure 5.23: Magnitude of the electric field scattered by the  $0.2\lambda$ -radius sphere. Flat triangulation of the sphere is used with the flat RWG basis functions. The results are given on the three principle cuts of the sphere for different discretizations and different numbers of unknowns. — Mie series,  $\cdots$   $7 \times 8$  divisions and 144 unknowns,  $-\cdot-$   $9 \times 10$  divisions and 240 unknowns,  $--$   $11 \times 16$  divisions and 480 unknowns.

subdomain is projected on the sphere to form the curved triangular subdomain. The CRWG BFs are used on pairs of curved triangular subdomains. The induced surface current results are shown in Fig. 5.24. The current results seem noisier than the flat triangulation results. This is due to the curved nature of the CRWG BFs, which is a result of the parametric mapping in their definition. The convergence towards the exact solution is observed as the number of BFs used is increased.

Although the current results seem worse, the scattered field results shown in Fig. 5.25 obtained using the exact model are superior to the results obtained using flat triangulation shown in Fig. 5.23. To obtain this degree of accuracy one has to use a large number of BFs with the flat triangulation. Thus the dependence of the scattered field results on the geometry model is clearly demonstrated by these results.

### 5.2.3 Exact Model with CRT BFs

Figure 5.26 shows the discretization of the sphere using the CRT BFs. This discretization is obtained by dividing the  $\theta$ - $\phi$  parametric domain into a uniform rectangular grid. The CRT BFs are defined on each pair of subdomains. This regular gridding results in a better current solution as seen in Fig. 5.27. Due to this nice gridding of the sphere, accurate far-field results have been obtained for number of unknowns as low as 54 as shown in Fig. 5.28. The accuracy of the scattered-field results are in the same order as those obtained using CRWG BFs presented in the previous subsection.

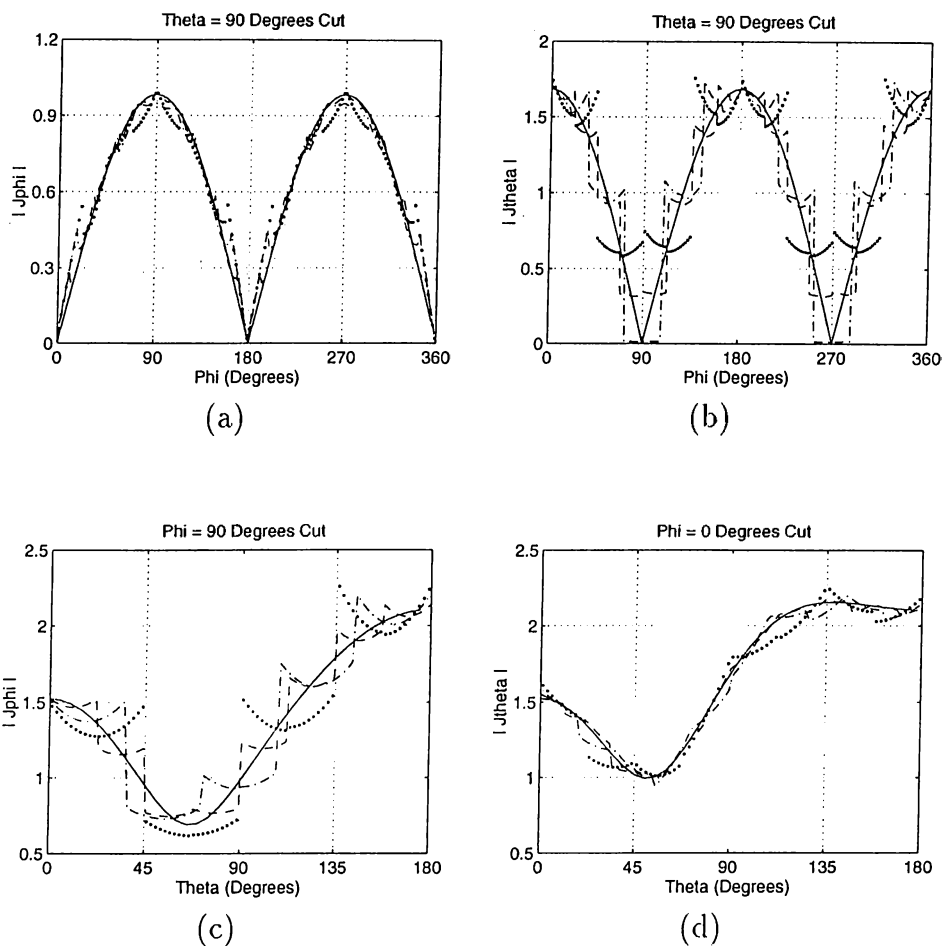


Figure 5.24: Magnitude of the surface current induced on the  $0.2\lambda$ -radius sphere. Curved triangulation of the sphere is used with the CRWG basis functions. The results are normalized with the magnitude of incident magnetic field and are given on the three principle cuts of the sphere for different discretizations and different numbers of unknowns. — Mie series,  $\cdots$   $7 \times 8$  divisions and 144 unknowns,  $-\cdot-$   $9 \times 10$  divisions and 240 unknowns,  $--$   $11 \times 16$  divisions and 480 unknowns.

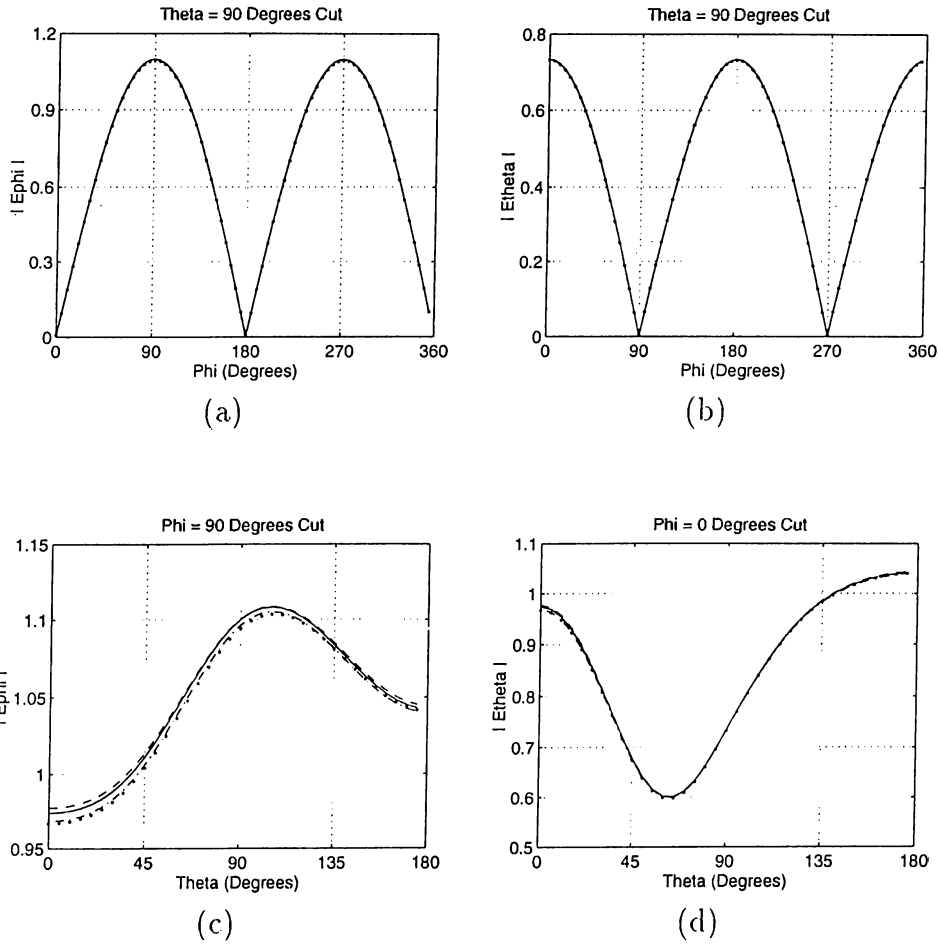


Figure 5.25: Magnitude of the electric field scattered by the  $0.2\lambda$ -radius sphere. Curved triangulation of the sphere is used with the CRWG basis functions. The results are given on the three principle cuts of the sphere for different discretizations and different numbers of unknowns. — Mie series,  $\cdots$   $7 \times 8$  divisions and 144 unknowns,  $-\cdot-$   $9 \times 10$  divisions and 210 unknowns,  $---$   $11 \times 16$  divisions and 480 unknowns.

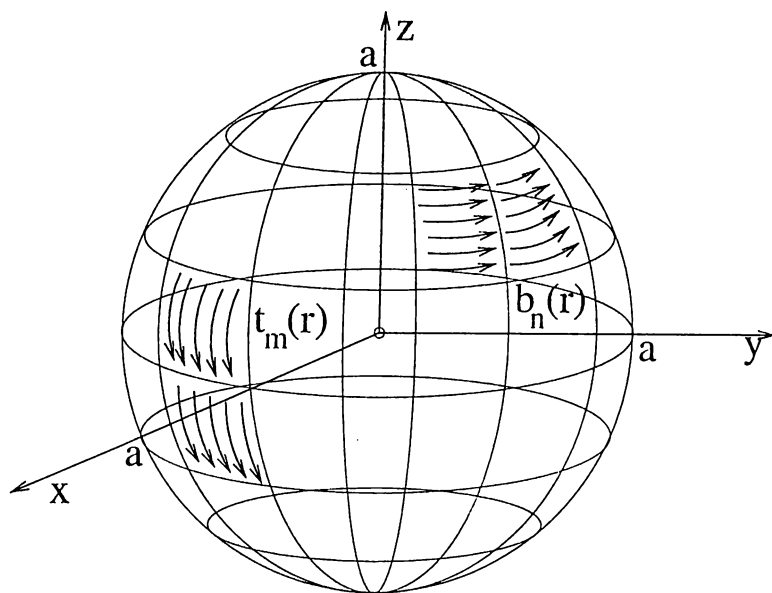


Figure 5.26: Rooftop basis and testing functions on the sphere.

#### 5.2.4 Quadratic Triangulation with CRWG BFs

In real-life electromagnetic scattering problems, the exact geometry model of the scatterer is almost never available and the scatterer must be approximated somehow. Finite-difference solution methods mostly approximate the geometry by a collection of cubic or rectangular domains. This may be called the zeroth-order approximation of the geometry. A better approximation is the flat triangulation of the scatterer surface, as presented before, which we may call the first-order approximation of the geometry. The degree of the polynomial approximation can be further increased. In this section, the solution of the same scattering problem outlined before using a higher-order geometry model, namely, the quadratic triangulation of the sphere, is presented. For the expansion of the induced surface current, the CRWG BFs defined on pairs of quadratic triangular subdomains are used. The triangulation of the sphere is directly obtained from a commercial CAGD program: MSC/ARIES. The

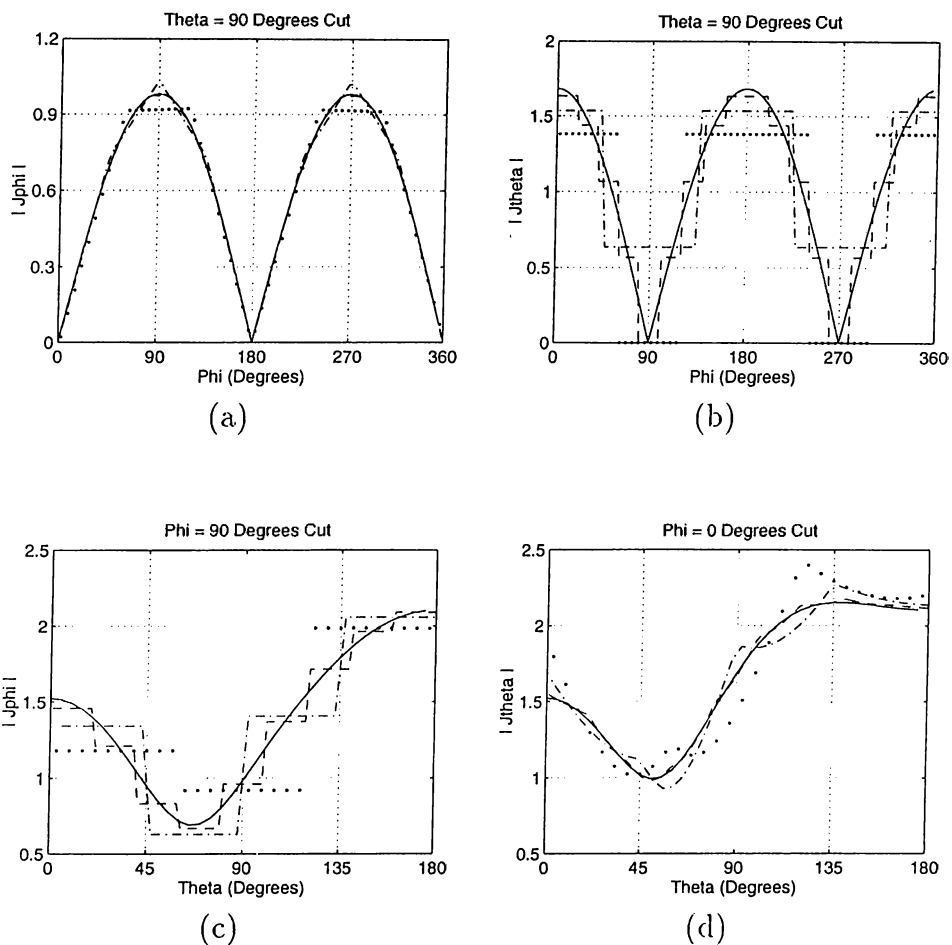


Figure 5.27: Magnitude of the surface current induced on the  $0.2\lambda$ -radius sphere. Curved rectangular meshing of the sphere is used with the CRT basis functions. The results are normalized with the magnitude of incident magnetic field and are given on the three principle cuts of the sphere for different discretizations and different numbers of unknowns. — Mie series,  $\cdots$   $5 \times 6$  divisions and 54 unknowns,  $-\cdot-$   $7 \times 8$  divisions and 104 unknowns,  $--$   $9 \times 18$  divisions and 306 unknowns.



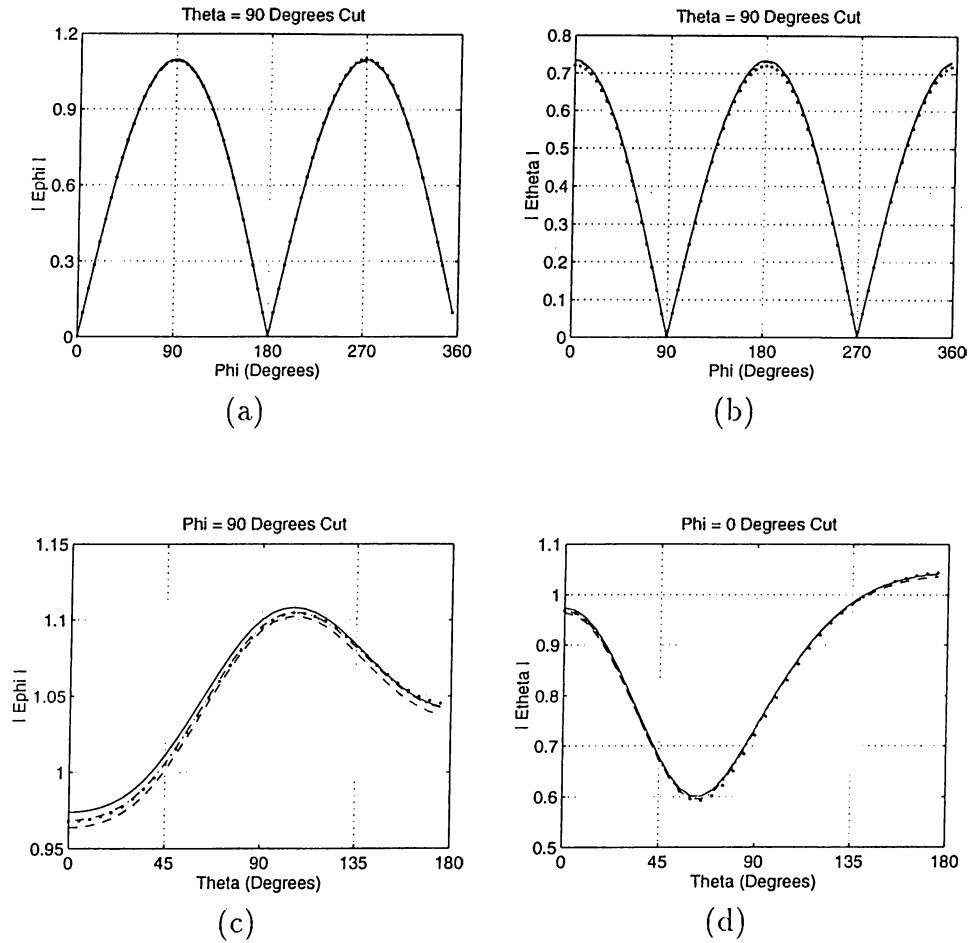


Figure 5.28: Magnitude of the electric field scattered by the  $0.2\lambda$  radius sphere. Curved rectangular meshing of the sphere is used with the CRT basis functions. The results are given on the three principle cuts of the sphere for different discretizations and different numbers of unknowns. — Mie series,  $\cdots$   $5 \times 6$  divisions and 54 unknowns,  $-\cdot-$   $7 \times 8$  divisions and 104 unknowns,  $---$   $9 \times 18$  divisions and 306 unknowns.

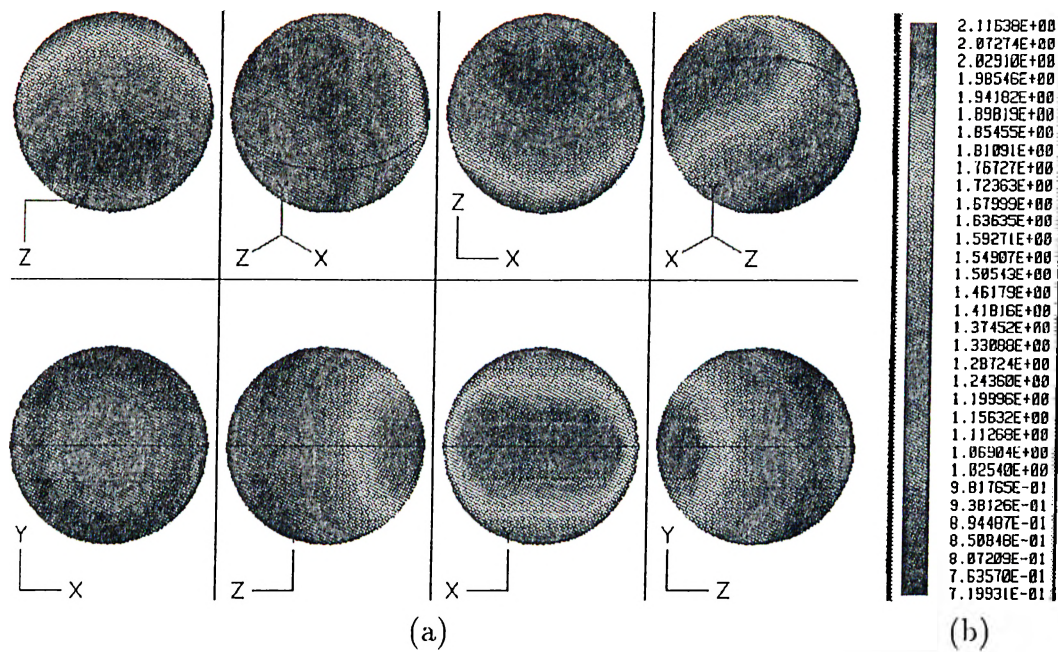


Figure 5.29: Magnitude of the induced surface current on a  $0.2\lambda$ -radius sphere. The sphere is discretized using quadratic triangles and the EFIE is solved using the CRWG BFs defined on these triangular subdomains. The color plot was generated using the MSC/ARIES.

results on the vertices of the triangulation are input back to the program for the visualization of the solution.

The magnitude of the induced surface current on the  $0.2\lambda$ -radius sphere is seen in Fig. 5.29 from 8 different views. The scattered-field results are given in Fig. 5.30 for a  $0.2\lambda$ -radius sphere and in Fig. 5.31 for a  $0.5\lambda$ -radius sphere. The results are very close to the exact solution, meaning that the quadratic triangular patch approximation performs significantly better than the flat patch model.

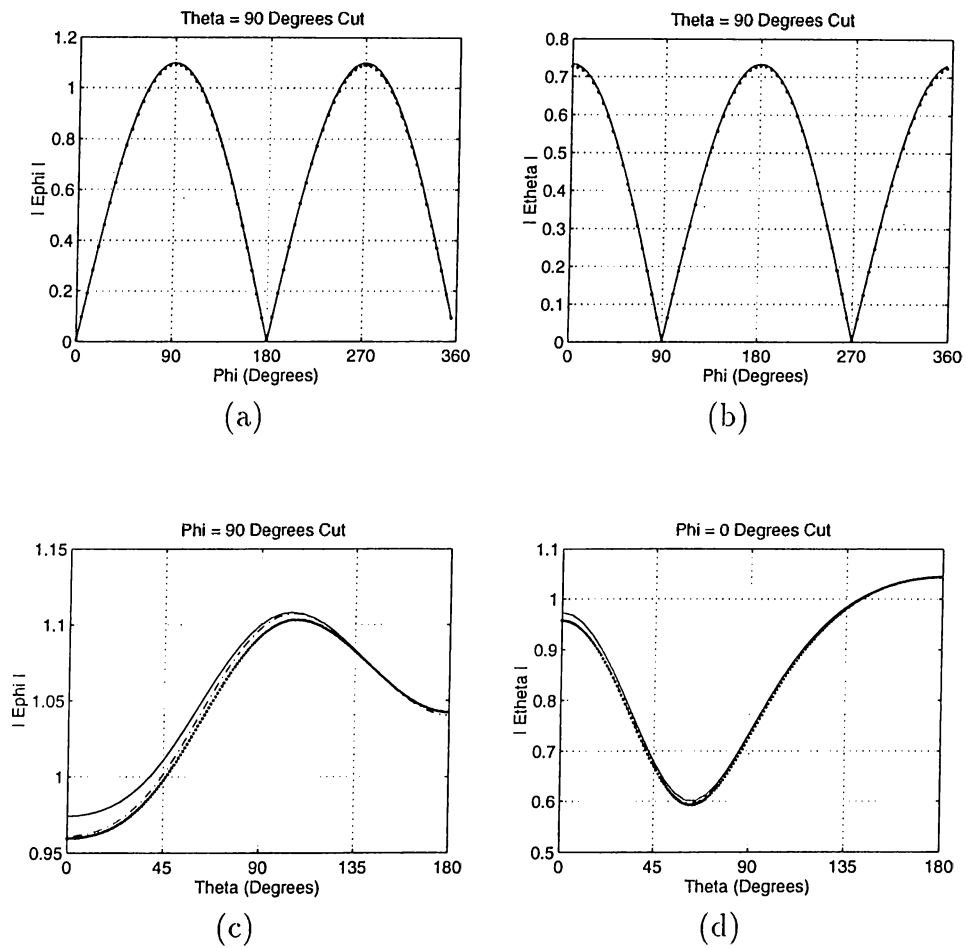


Figure 5.30: Magnitude of the electric field scattered by the  $0.2\lambda$ -radius sphere. Curved triangulation of the sphere, obtained from the MSC/ARIES, is used with the CRWG BFs. The results are given on the three principle cuts of the sphere. — Mie series,  $\cdots$  156 curved RWG BFs,  $-\cdot-$  318 curved RWG BFs.

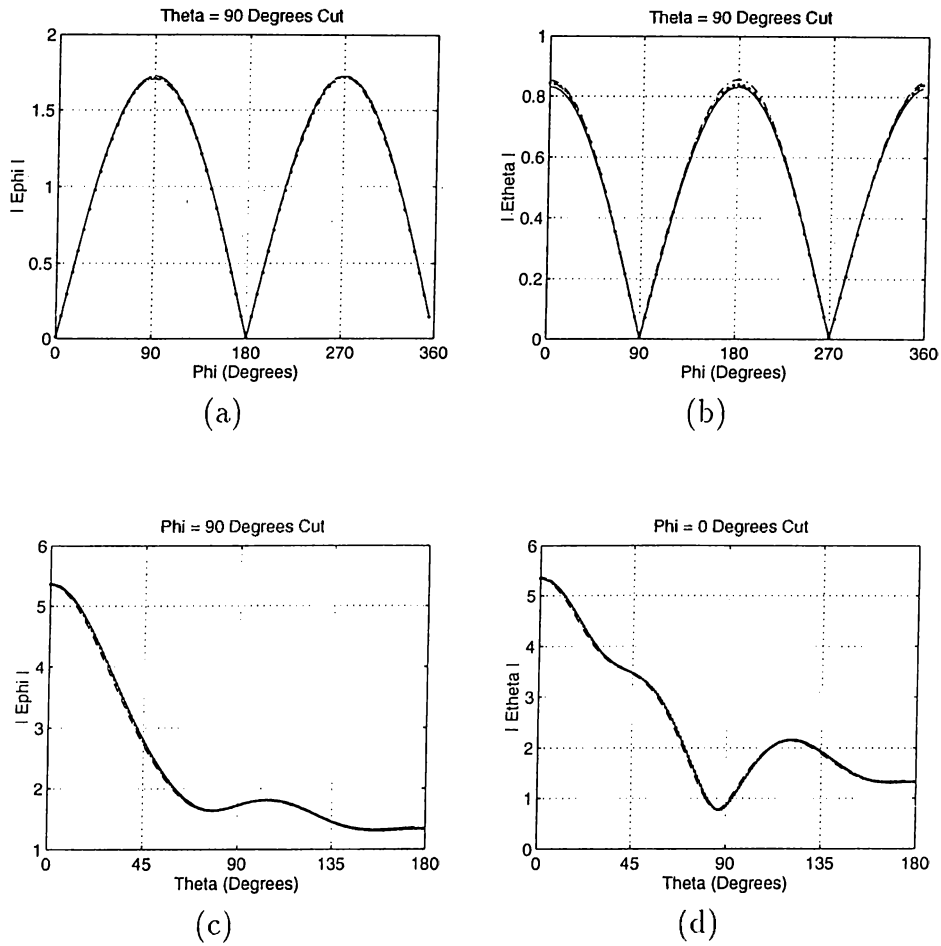


Figure 5.31: Magnitude of the electric field scattered by the  $0.5\lambda$ -radius sphere. Curved triangulation of the sphere, obtained from the MSC/ARIES, is used with the CRWG basis functions. The results are given on the three principle cuts of the sphere. — Mie series,  $\cdots$  480 curved RWG BFs,  $-\cdot-$  831 curved RWG BFs,  $--$  1020 curved RWG BFs.

### 5.2.5 Bezier-Patch Model with CRT BFs

If available CAGD programs are examined, it will be observed that nearly all of them are based on NURBS meshes. The NURBS surfaces are defined and explained in Chapter 3. Their advantage is that they allow complex shapes, including conic sections, to be defined precisely by means of a small number of NURBS surfaces, which are defined by a small number of control points. For instance, a sphere can be described by only one NURBS. Any NURBS can also be written in terms of piecewise rational Bézier patches. It is quite fast and easy to obtain the Bézier mesh form of a NURBS representation by applying the Cox-de Boor transformation algorithm [17].

A code that uses the Bézier patch model of the scatterer geometry with CRT BFs defined on them is implemented for the solution of scattering problems involving arbitrary curved scatterers. 8-patch Bézier model of the sphere is used along with the CRT BFs to check the performance of the code and the modeling technique. The discretization is performed in the parametric space of each patch by dividing the definition domain of the patch uniformly into rectangular subdomains. Figure 5.32 depicts the far-fields scattered from a  $0.2\lambda$ -radius sphere. The agreement with the analytical result is good for all discretizations. The results of the  $0.5\lambda$ -radius sphere are also in good agreement with the closed-form solutions as depicted in Fig. 5.33.

The advantage of using Bézier patches is that the geometry designed in a CAGD program using NURBS meshes is directly used in the solution algorithm. Therefore, no geometry modeling error is induced on the solution.

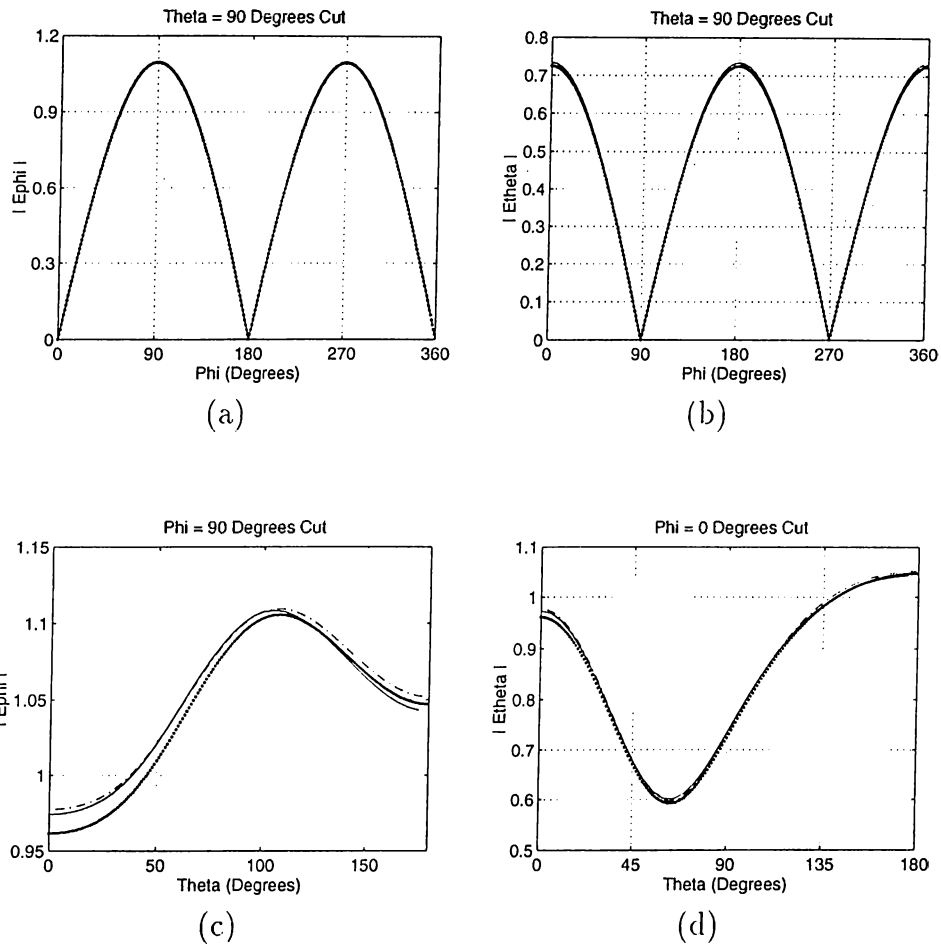


Figure 5.32: Magnitude of the electric field scattered by the  $0.2\lambda$ -radius sphere. S-patch Bézier model of the sphere is used with the CRT BFs. The results are given on the three principle cuts of the sphere. — Mie series,  $\cdots$  132 curved RT BFs,  $-\cdot-$  240 curved RT BFs.

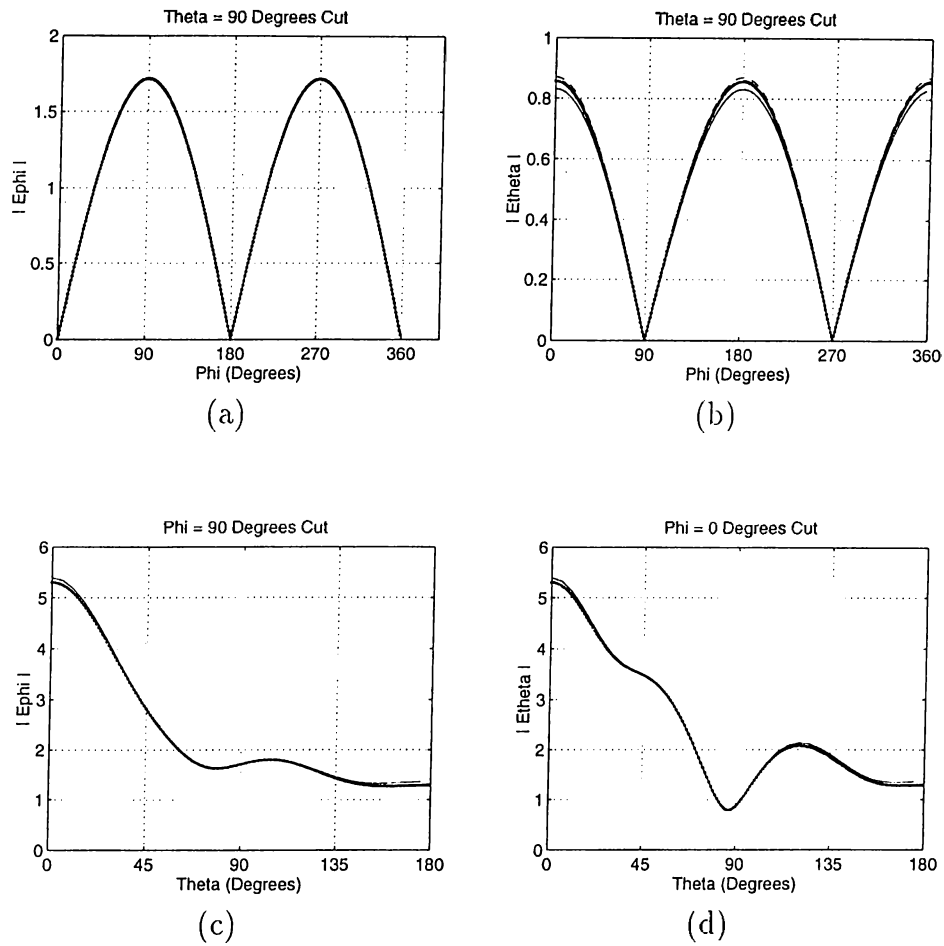


Figure 5.33: Magnitude of the electric field by scattered the  $0.5\lambda$ -radius sphere. 8-patch Bézier model of the sphere is used with the CRT BFs. The results are given on the three principle cuts of the sphere. — Mie series,  $\cdots$  552 curved RT BFs,  $-\cdot-$  756 curved RT BFs,  $- - -$  992 curved RT BFs.

### 5.2.6 Comparison of Different Modeling Schemes

The problem of scattering from a  $0.5\lambda$ -radius sphere is solved by using the flat triangulation, exact curved triangulation, and exact rectangular mesh of the sphere with the RWG BFs, the CRWG BFs, and the CRT BFs, respectively. The current results and the scattered-field results are superimposed with the exact solution for comparison. It is interesting to note in Fig. 5.34 that the current solutions obtained with flat and curved triangulations are very close to each other, both being also close to the exact solution. The reason of the sharp spikes on the current solution in Fig. 5.34(a) was explained in Section 5.1. The solution obtained with the CRT BFs does not exhibit such irregularities.

Although the current solutions for the flat RWG BFs and the CRWG BFs are close to each other, Fig. 5.35 shows that the scattered-field results are not as close as may be expected. The reason for this is that the geometries, on which the flat RWG BFs and the CRWG BFs are defined, are different. This difference in the positions of the currents in space, defined by the RWG BFs and the CRWG BFs, shows itself as a difference in the scattered-field results, because of the phase term in the far-field transformation. All results are seen to agree with the exact solution, some showing better agreement.

The scattered-field solutions of the  $0.2\lambda$ -radius sphere problem using the quadratic triangular patch model and the Bézier patch model for approximately the same number of unknowns is shown in Fig. 5.36 for comparison. The results of the  $0.5\lambda$ -radius sphere problem are compared in Fig. 5.37. The agreement of both solutions with the exact solution is good. For the  $0.5\lambda$ -radius sphere problem, quadratic triangular patch solution performs marginally better than



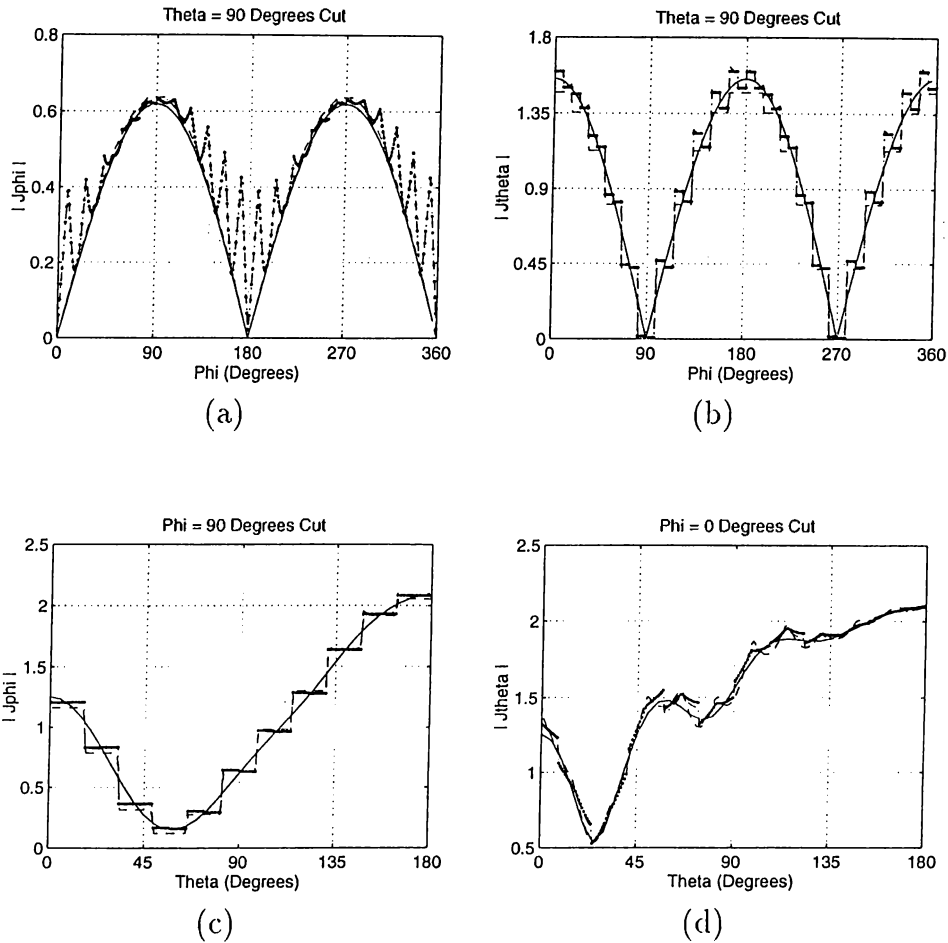


Figure 5.34: Magnitude of the surface current induced on the  $0.5\lambda$ -radius sphere. Flat-triangulation, curved-triangulation, and curved-rectangular meshing of the sphere are used with the RWG, the CRWG, and the CRT BFs, respectively. The results are normalized with the magnitude of incident magnetic field and are given on the three principle cuts of the sphere. — Mie series,  $\cdots$   $11 \times 16$  divisions and 660 flat RWG BFs.  $-\cdot-$   $11 \times 16$  divisions and 660 curved RWG BFs,  $--$   $11 \times 22$  divisions and 462 curved RT BFs.

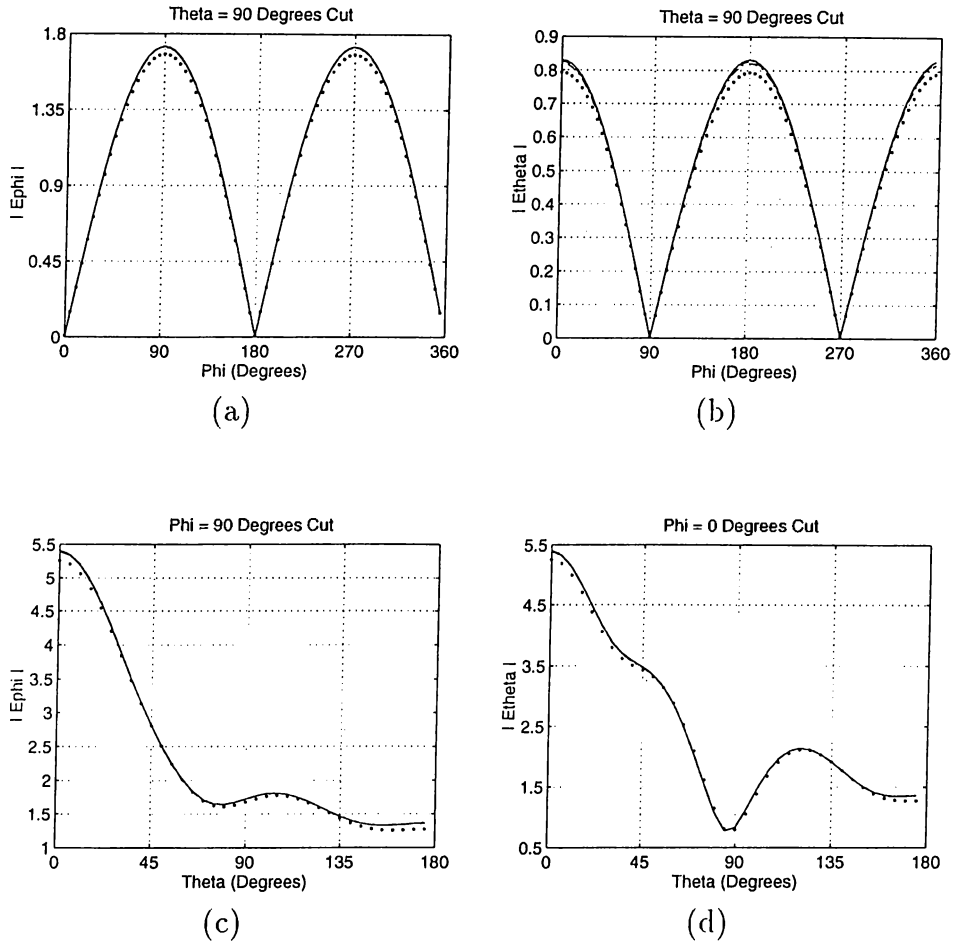


Figure 5.35: Magnitude of the electric field scattered by the  $0.5\lambda$ -radius sphere. Flat-triangulation, curved-triangulation, and curved-rectangular meshing of the sphere are used with the RWG, the CRWG, and CRT BF's respectively. The results are given on the three principle cuts of the sphere. — Mic series,  $\cdots$   $11 \times 16$  divisions and 660 flat RWG BF's.  $-\cdot-$   $11 \times 16$  divisions and 660 curved RWG BF's,  $--$   $11 \times 22$  divisions and 462 curved RT BF's.

the Bézier patch solution. This performance difference can be attributed to the degenerations of the surface at the poles of the sphere for the 8-patch Bézier model.

As a quantitative comparison between various geometry modeling techniques, Fig. 5.38 shows the maximum difference between the far-fields scattered by a  $0.5\lambda$  radius sphere computed using different geometry models for the sphere. The far-field is sampled at 117 directions chosen uniformly on the unit sphere, and Mie series solution is used as the reference. The performance of different geometry modeling techniques can be observed as a function of unknowns. Figure 5.39 depicts the norm of the error obtained as the square-root of the sum of the squares of the error values at the 117 directions. The effect of the geometry model on the solution is well observed on this plot as a function of number of unknowns. It should be noted that both Bézier-patch models of the sphere are exact but the 8-patch model has surface degeneracies at the poles. This degeneracy shows itself in the definition of the basis functions around the two poles. Due to this degeneration the performance of the 8-patch Bézier model is worse than the 6-patch Bézier model which does not have any surface degeneracies.

Figure 5.40 depicts two solutions obtained by solving the same problem with both with the MoM and the FMM using quadratic triangular patch models and Bézier patch models of the scatterers. The MoM result using the CRWG BFs, shown in Fig. 5.40(a) is obtained in 155 seconds, whereas the FMM solution is obtained in 122 seconds using an iterative solver. The solution obtained using the Bézier-patch model of the flat patch shown in Fig. 5.40(b) is obtained in 291 seconds with the MoM and in 180 seconds with the FMM.

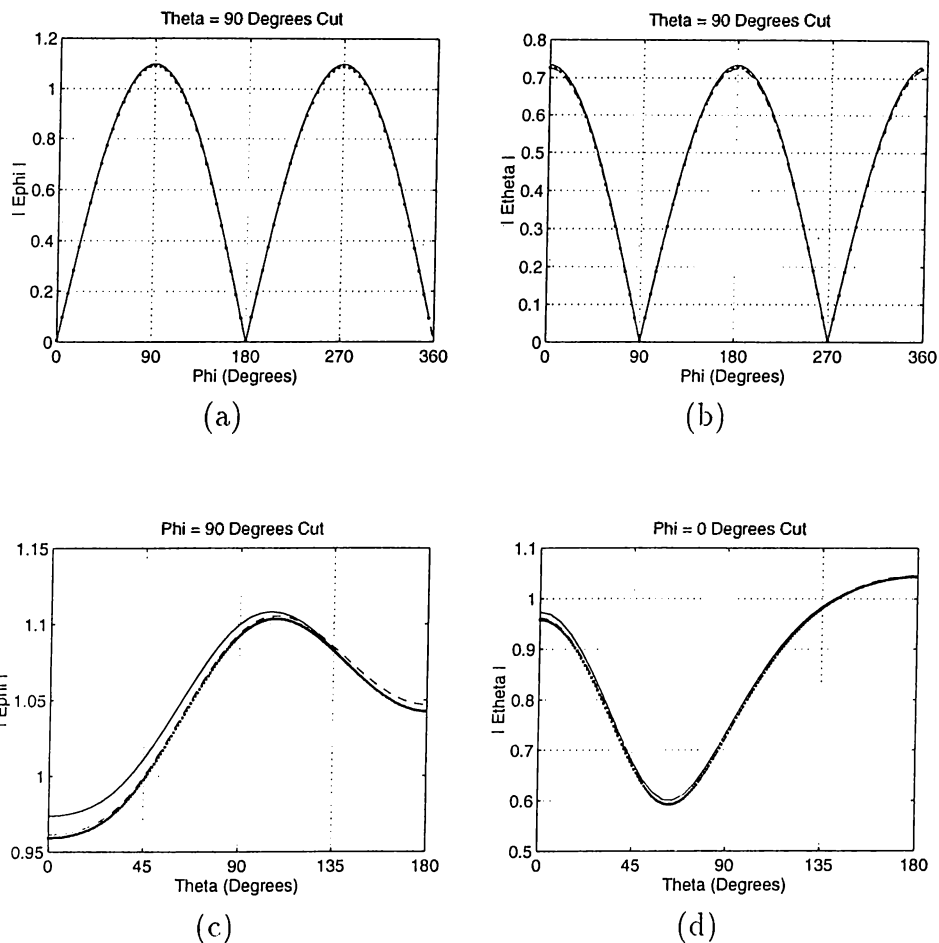


Figure 5.36: Comparison of the different geometry models used in the computation of the magnitude of the electric field scattered by the  $0.2\lambda$ -radius sphere. Curved triangulation of the sphere, obtained from the MSC/ARIES, is used with the CRWG BFs and the 8-patch Bézier model of the sphere is used with the CRT BFs. The results are given on the three principle cuts of the sphere. — Mie series,  $\cdots$  156 curved RWG BFs,  $---$  132 curved RT BFs.

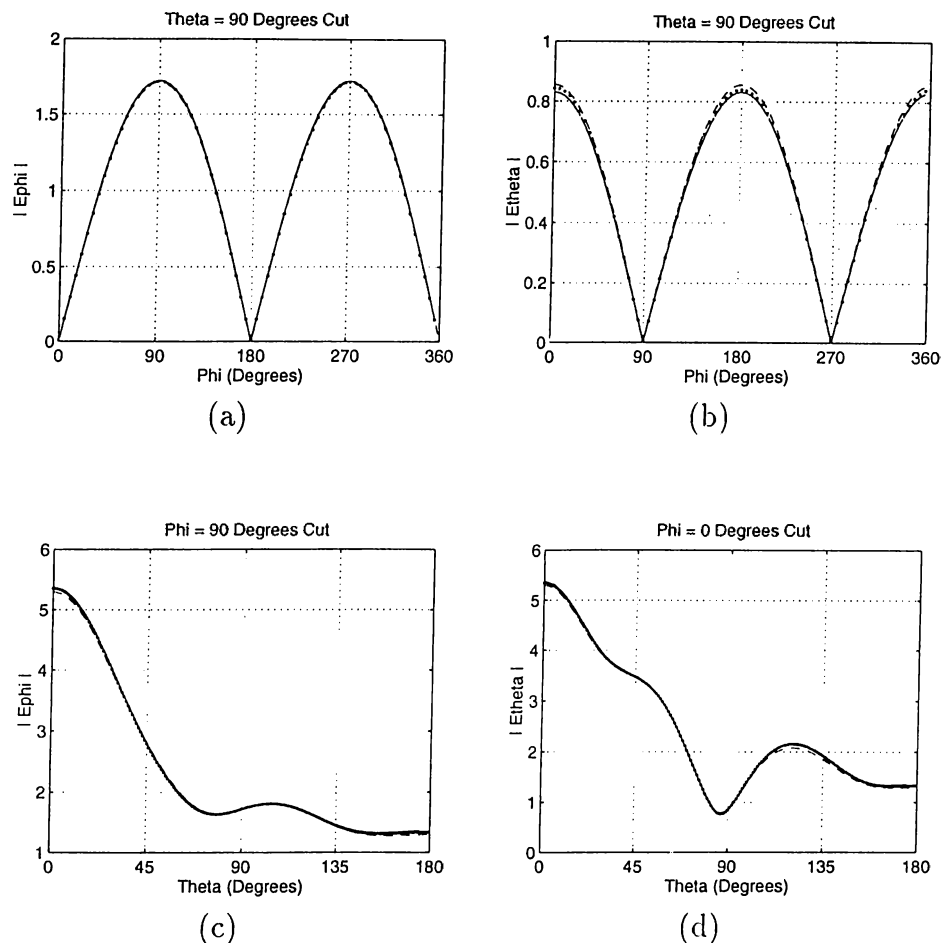


Figure 5.37: Comparison of the different geometry models used in the computation of the magnitude of the electric field scattered by the  $0.5\lambda$ -radius sphere. Curved triangulation of the sphere, obtained from the MSC/ARIES is used with the CRWG BFs and  $\delta$ -patch Bézier model of the sphere is used with the CRT BFs. The results are given on the three principle cuts of the sphere. — Mie series,  $\cdots$  480 curved RWG BFs, -- 552 curved RT BFs.

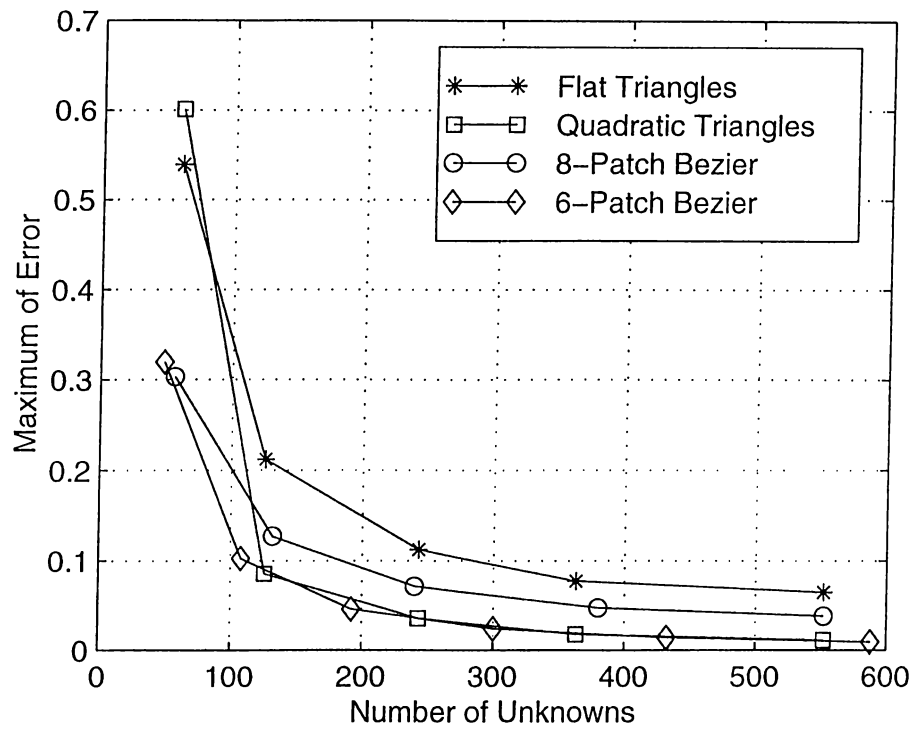


Figure 5.38: Maximum difference in the far-field solutions using different geometry models of the sphere.

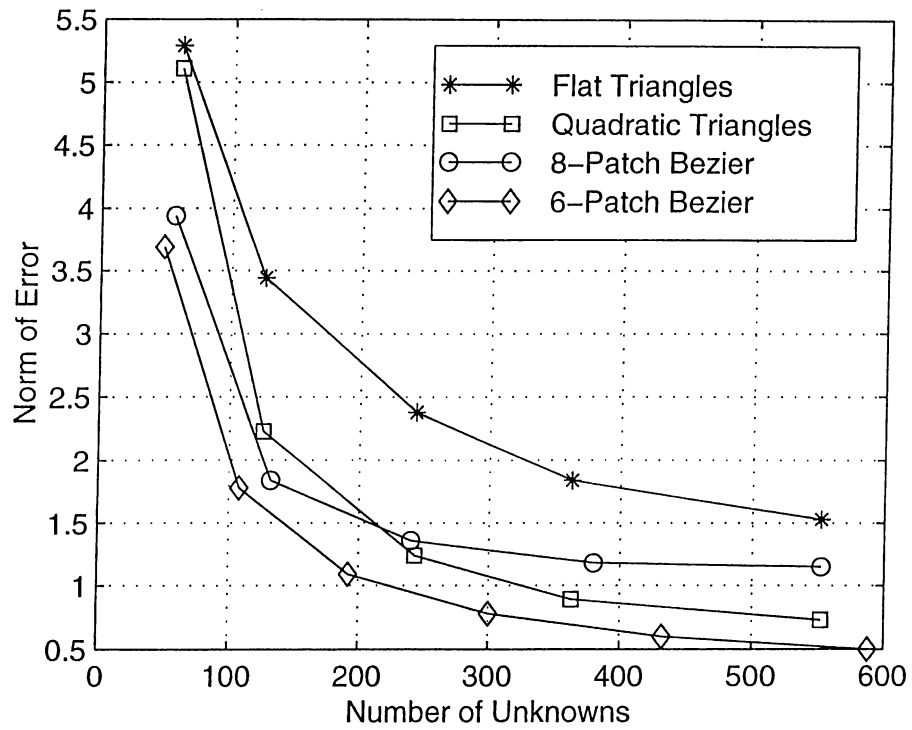


Figure 5.39: Norm of the difference in the far-field solutions using different geometry models of the sphere.

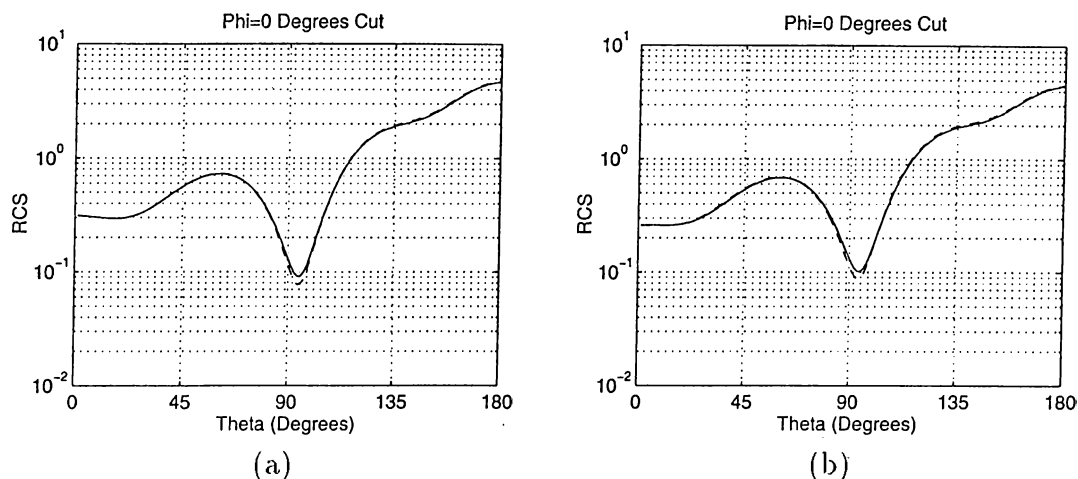


Figure 5.40: Validations of the FMM solutions. (a) Bistatic RCS of a  $0.5\lambda$ -radius sphere using 480 CRWG BF's, — the MoM solution, -- the FMM solution, (b) Bistatic RCS of a  $0.5\lambda$  radius sphere using 380 CRT BF's, — the MoM solution, -- the FMM solution.

### 5.3 Missile

As an example of a real-life scatterer, a generic missile is considered. The missile is designed using the second-order rational Bézier patches on a commercial CAGD program: RHINOCEROS. It should be noted that this missile is not a model of any existing missile. The problem configuration is as follows: The missile is lying in the  $z$  direction with the main wings on the  $y$ - $z$  plane. For bistatic RCS calculations, the incident field is  $x$  directed and propagating in the negative  $z$  direction (head-on incidence). The scattered far field is observed on the  $y$ - $z$  plane. Figure 5.41 shows a typical quadratic triangulation of the missile.

Figure 5.42 shows the magnitude of the induced surface current on the missile that is illuminated with a head-on incident  $x$ -polarized plane wave.



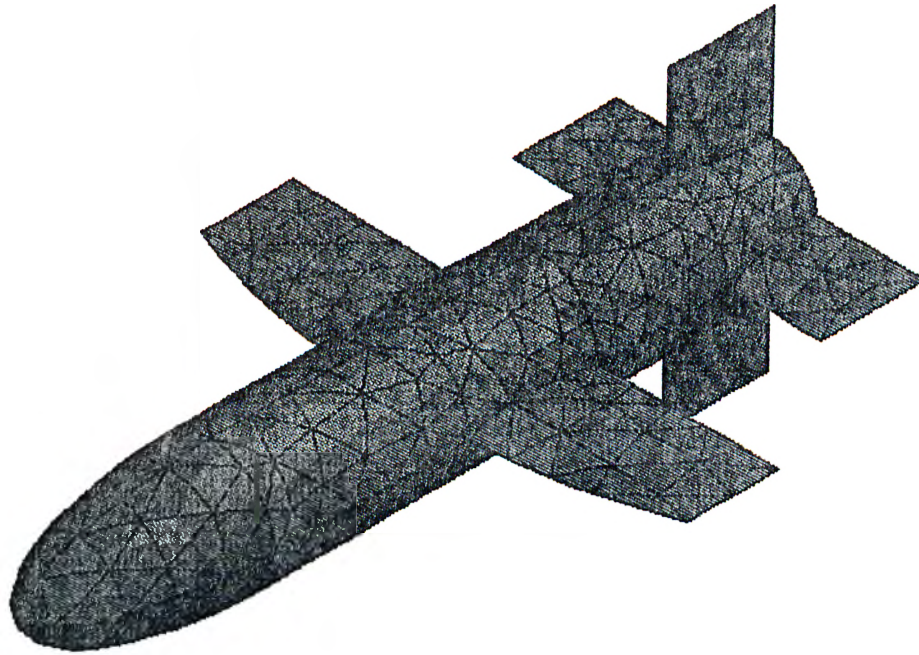


Figure 5.41: Quadratic triangular mesh of the missile generated using the MSC/ARIES.

The frequency of the wave is 10 MHz. At this frequency, the length of the missile is about twice the wavelength. The variation of the induced surface current on the missile verifies this observation. The solution is obtained using the curved triangulation of the missile with CRWG BFs. The color plot of the induced surface current is obtained from MSC/ARIES.

In Figs. 5.43, 5.44, and 5.45, the bistatic RCS results of the missile is shown. The problem is solved at three different frequencies using the curved triangulation and the Bézier-patch model of the missile, again for a head-on incident  $x$ -polarized plane wave. Also shown in the plots are the results of the flat triangulation model of the missile from İ. Kürşat Şendur. The scattered field is observed on the  $y$ - $z$  plane. The agreement among the results is fairly good. It should be noted that fairly good results are observed using as low as 5 unknowns per wavelength.

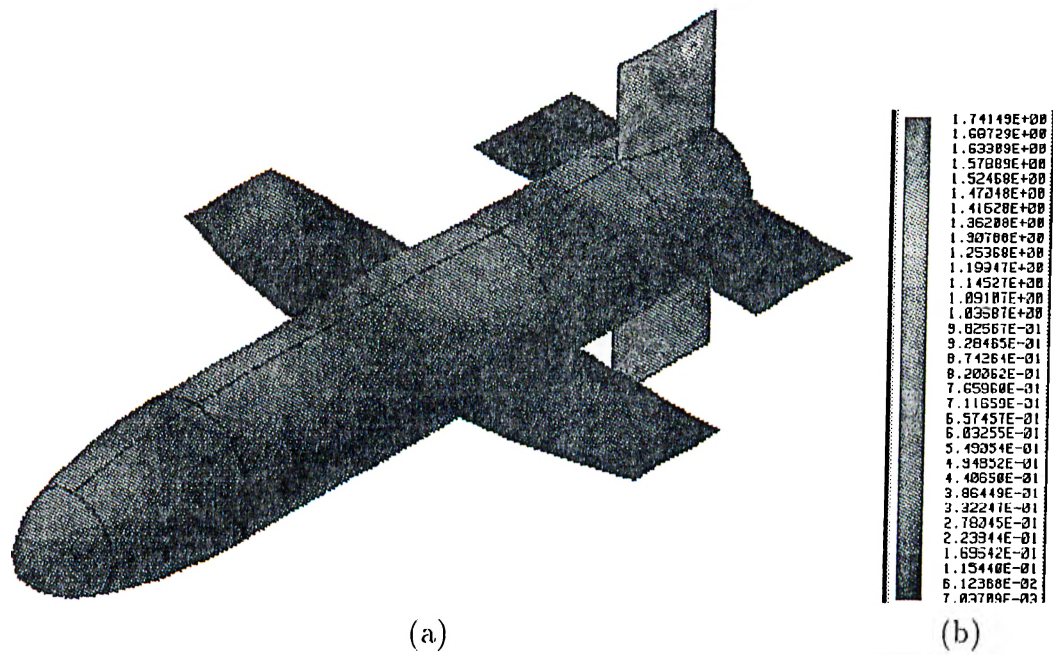


Figure 5.42: Magnitude of the induced surface current on a 6-meter long missile at 100 MHz. The missile is discretized using quadratic triangles and the EFIE is solved using the CRWG BF's defined on these triangular subdomains. The color plot is generated using the MSC/ARIES.

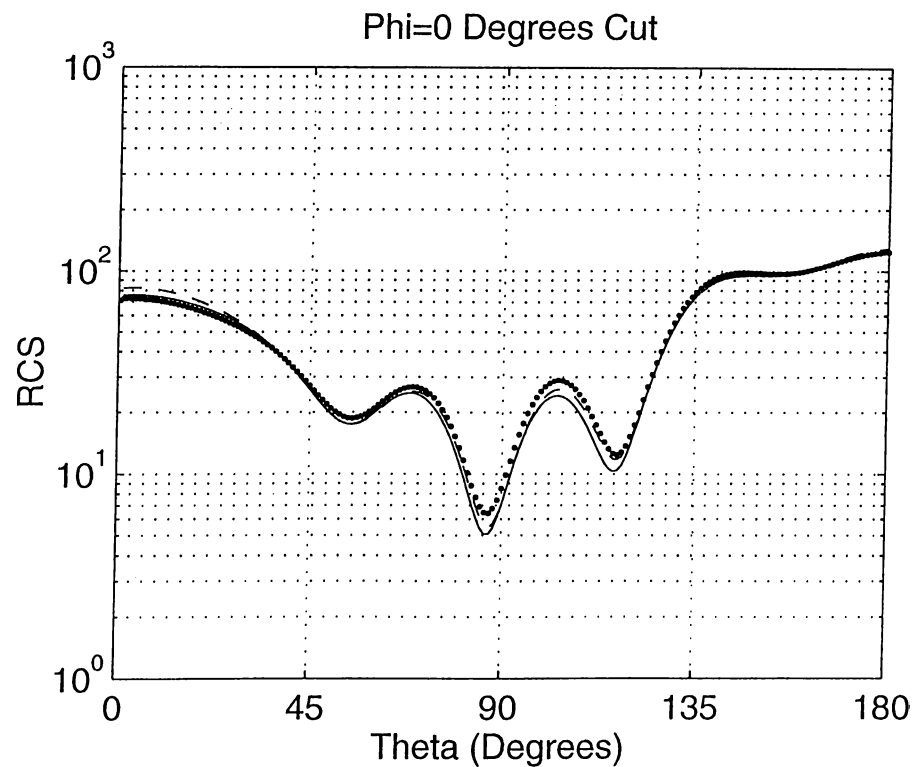


Figure 5.43: Comparison of the bistatic RCS of the 6-meter long missile at 100 MHz. Curved and flat triangulations of the missile, obtained from the MSC/ARIES, is used with the CRWG BFs and flat-RWG BFs respectively, and 34-patch Bézier model of the missile is used with the CRT BFs. The results are given on  $x$ - $z$  plane, where the main wings of the missile are located. — 1053 flat-RWG BFs, - - 1053 CRWG BFs, ··· 1088 CRT BFs.

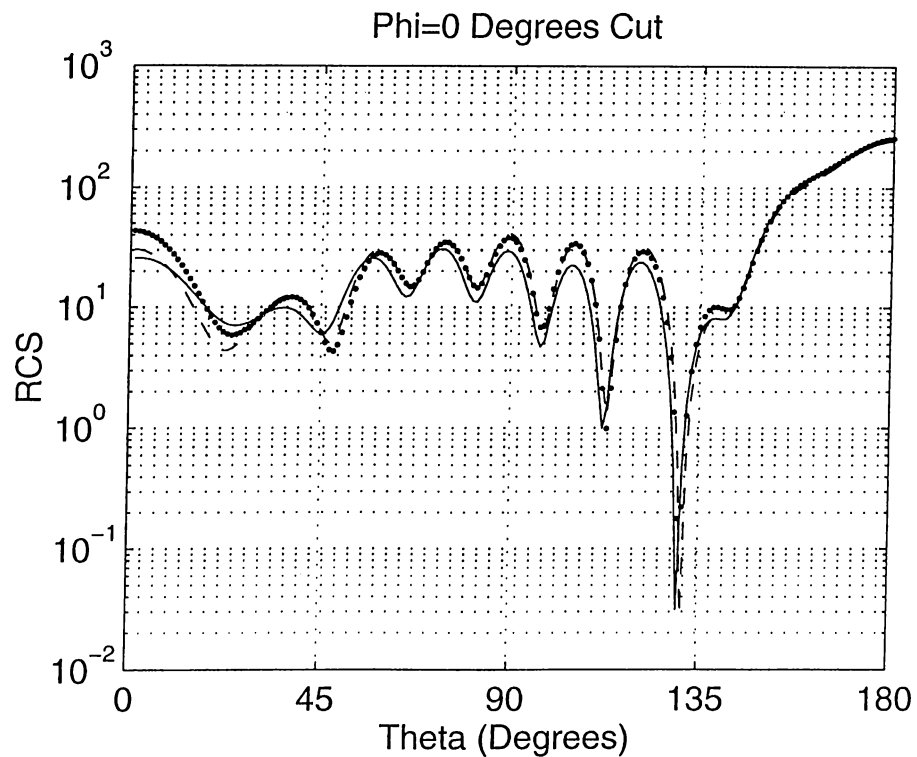


Figure 5.44: Comparison of the bistatic RCS of the 6-meter long missile at 200 MHz. Curved and flat triangulation of the missile, obtained from the MSC/ARIES, is used with the CRWG BF's and flat-RWG BF's respectively, and 34-patch Bézier model of the missile is used with the CRT BF's. The results are given on  $x$ - $z$  plane, where the main wings of the missile are located. — 2058 flat-RWG BF's, - - 2058 CRWG BF's, ··· 2448 CRT BF's.

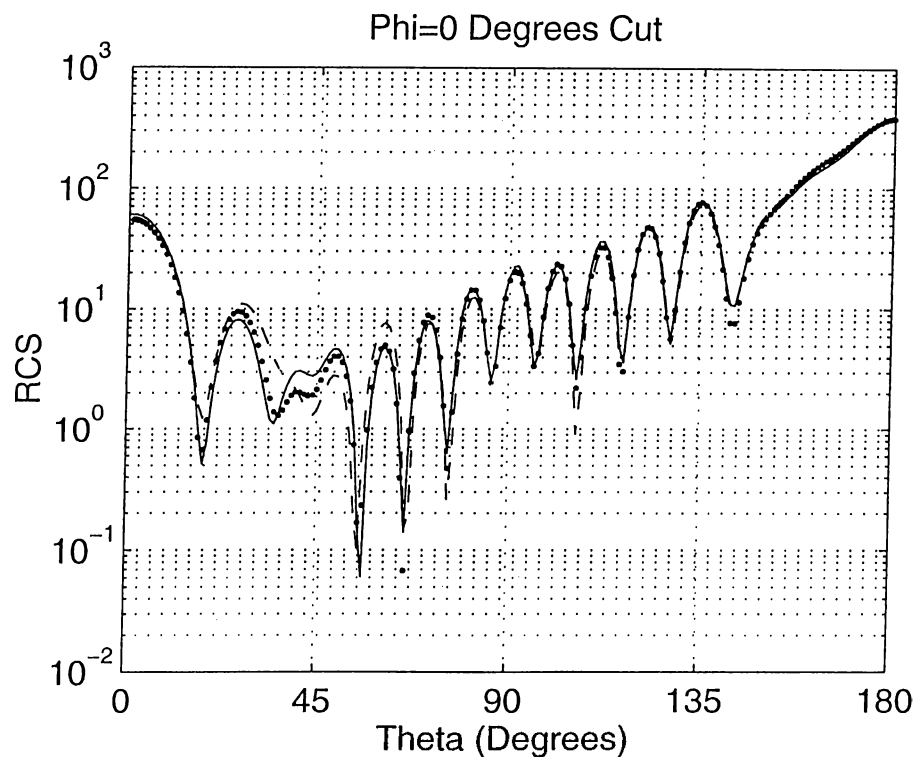


Figure 5.45: Comparison of the bistatic RCS of the 6-meter long missile at 300 MHz. Curved and flat triangulation of the missile, obtained from the MSC/ARIES, is used with the CRWG BFs and flat-RWG BFs respectively, and 34-patch Bézier model of the missile is used with the CRT BFs. The results are given on  $x$ - $z$  plane, where the main wings of the missile are located. — 7713 flat-RWG BFs, - - 6213 CRWG BFs, ... 4352 CRT BFs,

# Chapter 6

## Conclusions

In this thesis, a general MoM formulation of electromagnetic scattering problems involving arbitrarily shaped surface scatterers is presented. The BFs used in the MoM formulations are defined, and issues concerning the evaluation of the MoM matrix elements are addressed. Different BFs are investigated and some seemingly legitimate BFs are demonstrated to be insufficient to model the unknown functions in the formulations.

Different geometry-modeling techniques, which are used to represent the scatterer geometry in the solution algorithm, are investigated. The BFs used in the MoM formulations are modified for geometry models that contain surface curvature. Curved generalizations of some frequently used BFs to be defined on curved parametric surfaces are given. The effect of different geometry-modeling schemes on the solution of the problem is investigated. It is shown that the technique used to approximate the scatterer in the solution algorithm influences the solution more than the type of the BFs used for the approximation of the

unknown.

Two different algorithms using different geometry-modeling techniques and different BFs are developed. The first one uses quadratic triangular patches to approximate the scatterer and the CRWG BFs, defined on these patches, to approximate the induced surface current density. The second uses the Bézier-patch model of the scatterer with the CRT BFs. When applied to the same problems, both are observed to perform equally well. But, due to the simplicity of its parametric mapping, the quadratic triangular patch algorithm is faster. Although the parametric mapping of an  $n$ th-order rational Bézier patch is more complicated and time consuming, the representation potential of rational Bézier patches are superior to quadratic triangular patches. NURBS surfaces, which are collections of smoothly blended rational Bézier patches, are very powerful modeling tools that are widely used in CAGD applications. They are also among the most commonly used geometry-data transfer formats due to the representation capability of complicated geometries using a small number of points in space. Therefore, the geometry of the scatterer designed in a CAGD tool that uses the NURBS surfaces as the geometry format can be directly used in the electromagnetic scattering algorithm, which is capable of representing geometries in the NURBS format. Hence, no geometry-modeling error is induced in the solution of the problem. Various results for contrasting the effect of using different geometry models in the solutions are given.

Using higher-order geometry approximations for the scatterers, the error induced by the geometry model is minimized. Therefore, it is possible to reduce the size of the problem for a demanded accuracy using better geometry models. This reduction in the size of the problem is of ultimate importance since most

real-life electromagnetic scattering problems involve electrically large scatterers. When these large problems are discretized using the MoM, the resulting systems of equations are also large.

The FMM is applied to the scattering problems involving electrically large scatterers modeled by curved subsurfaces. This combination of the FMM with curved surface modeling is proposed for the efficient solution of large electromagnetic scattering problems. The FMM reduces the computational cost of the matrix-vector product at each iteration of the solver to  $O(N^{1.5})$ . The ordinary matrix-vector product would take  $O(N^2)$  operations and the direct solution of the system by the Gaussian elimination would require  $O(N^3)$  operations. The storage complexity of the FMM is also  $O(N^{1.5})$  in contrast to the  $O(N^2)$  storage complexity of the conventional MoM. Therefore, by employing the FMM, it is possible to solve larger problems on a given hardware. A sample problem, scattering from a missile, is solved in order to demonstrate the applicability of the proposed algorithms to real-life electromagnetic scattering problems.

It is shown that the combination of the FMM with curved-surface modeling results in an efficient algorithm which requires less memory and CPU time for the solution of large problems involving 3-D arbitrarily shaped surface scatterers. Extensions of the FMM, such as the multilevel FMM, which would further reduce the computational cost of the solutions are among the future work that can be carried on on this subject.



# Appendix A

## Evaluation of the MoM Matrix Elements

The MoM matrix elements appearing in the formulations as double surface integrals on testing and basis subdomains are evaluated numerically in two different ways depending on the distance between the testing and the basis functions. All surface integrals appearing in the formulation are evaluated in the parametric space on the unit square. Fixed-order Gaussian quadrature [11] is used for the evaluation of these integrals, which is observed to perform better than other quadrature rules [28, 29, 11].

## A.1 Singular Integrals Appearing in the Formulation

A matrix element in the MoM formulation is rewritten below,

$$Z_{mn} = \int_s ds \mathbf{t}_m(\mathbf{r}) \cdot \int_{s'} ds' \left[ \mathbf{j}_n(\mathbf{r}') + \frac{1}{k^2} \nabla' \cdot \mathbf{j}_n(\mathbf{r}') \nabla \right] \frac{e^{ikR}}{R}, \quad (\text{A.1})$$

where

$$R = |\mathbf{r} - \mathbf{r}'| \quad (\text{A.2})$$

and  $\mathbf{t}_m$  and  $\mathbf{b}_n$  are the testing and basis functions respectively. Using the vector identity

$$\nabla \cdot (\phi \mathbf{t}) = \nabla \phi \cdot \mathbf{t} + \phi \nabla \cdot \mathbf{t} \quad (\text{A.3})$$

and Gauss' law

$$\int_s ds \nabla \cdot (\phi \mathbf{t}) = \int_s ds \nabla \phi \cdot \mathbf{t} + \int_s ds \phi \nabla \cdot \mathbf{t} \quad (\text{A.4})$$

$$\oint_c \phi \mathbf{t} \cdot \mathbf{dn}_c = \int_s ds \nabla \phi \cdot \mathbf{t} + \int_s ds \phi \nabla \cdot \mathbf{t} \quad (\text{A.5})$$

where  $\mathbf{dn}_c$  is differential normal vector of the curve  $c$ , and the fact that, for basis functions used in the formulations,  $\mathbf{t} \parallel \mathbf{dn}_c$ , it is possible to reduce the expression for the matrix element. Defining  $\nabla \phi$  as

$$\nabla \phi = \nabla \left[ \frac{1}{k^2} \int_{s'} \nabla' \cdot \mathbf{j}_n \frac{e^{ikR}}{R} \right], \quad (\text{A.6})$$

and using

$$\mathbf{t} \parallel \mathbf{dn}_c \Rightarrow \int_s ds \nabla \phi \cdot \mathbf{t} = - \int_s ds \phi \nabla \cdot \mathbf{t}. \quad (\text{A.7})$$

$Z_{mn}$  is simplified to

$$Z_{mn} = \int_s ds \int_{s'} ds' \left[ \mathbf{t}_m(\mathbf{r}) \cdot \mathbf{j}_n(\mathbf{r}') - \frac{1}{k^2} \nabla \cdot \mathbf{t}_m(\mathbf{r}) \nabla' \cdot \mathbf{j}_n(\mathbf{r}') \right] \frac{e^{ikR}}{R}. \quad (\text{A.8})$$

When the matrix element is transformed to the parametric space using the general definition of the basis functions for curved triangular and curved rectangular subdomains as,

$$\mathbf{f}(u, v) = \begin{pmatrix} \mathbf{f}_{CRWG}(u, v) \\ \mathbf{f}_{CRT}(u, v) \end{pmatrix} = \frac{1}{\sqrt{g}} \left[ \begin{pmatrix} u \\ u \end{pmatrix} \frac{\partial \mathbf{r}}{\partial u} + \begin{pmatrix} 0 \\ v \end{pmatrix} \frac{\partial \mathbf{r}}{\partial v} \right] \quad (\text{A.9})$$

and the divergences as

$$\nabla \cdot \mathbf{f}(u, v) = \frac{1}{\sqrt{g}} \begin{pmatrix} 1 \\ 2 \end{pmatrix}, \quad (\text{A.10})$$

it can be further simplified to read

$$\begin{aligned} Z_{mn} = & \int_s \sqrt{g} dudv \int_{s'} \sqrt{g'} du' dv' \left[ \mathbf{t}_m(u, v) \cdot \mathbf{j}_n(u', v') \right. \\ & \left. - \frac{1}{k^2} \nabla \cdot \mathbf{t}_m(u, v) \nabla' \cdot \mathbf{j}_n(u', v') \right] \frac{e^{ikR}}{R}. \end{aligned} \quad (\text{A.11})$$

A normalized basis function can be defined to further simplify this expression,

$$\check{\mathbf{f}}(u, v) = \left[ \begin{pmatrix} u \\ u \end{pmatrix} \frac{\partial \mathbf{r}}{\partial u} + \begin{pmatrix} 0 \\ v \end{pmatrix} \frac{\partial \mathbf{r}}{\partial v} \right] \quad (\text{A.12})$$

with divergence,

$$\nabla \cdot \check{\mathbf{f}}(u, v) = \begin{pmatrix} 1 \\ 2 \end{pmatrix}, \quad (\text{A.13})$$

so that

$$Z_{mn} = \int_s dudv \int_{s'} du' dv' \left[ \check{\mathbf{t}}_m \cdot \check{\mathbf{j}}_n - \frac{1}{k^2} \nabla \cdot \check{\mathbf{t}}_m \nabla' \cdot \check{\mathbf{j}}_n \right] \frac{e^{ikR}}{R}, \quad (\text{A.14})$$

$$Z_{mn} = \int_s dudv \int_{s'} du' dv' \left[ \check{\mathbf{t}}_m \cdot \check{\mathbf{j}}_n - \frac{1}{k^2} \begin{pmatrix} 1 \\ 2 \end{pmatrix} \right] \frac{e^{ikR}}{R}. \quad (\text{A.15})$$

The matrix elements in Eq. (A.15) can now be computed by evaluating the integrals directly in the parametric space  $(u, v)$ . For RT BFs the integration

domain is the square domain bounded by  $u = 0, 1$  and  $v = 0, 1$  lines. For RWG BFs the integration domain is the triangular domain bounded by  $u = 0$ ,  $v = 0$  and  $u + v = 1$  lines. With an auxiliary transformation, this subdomain can be mapped to the same square domain in an auxiliary  $(\eta, \zeta)$  parametric space. Hence, the same integration routines designed for square integration domains can be used.

All integrals are hence transformed to integrals of the form

$$Z_{mn} = \int \int_{\square, \Delta} dudvdu'dv' \frac{g(u, v, u', v')}{R(u, v, u', v')} \quad (\text{A.16})$$

$$= \int \int_{\square, \Delta} dudvdu'dv' h(u, v, u', v'). \quad (\text{A.17})$$

The outer integrals over the testing subdomain are numerically easy to evaluate and are evaluated with a low-order Gaussian quadrature. For each sample of the outer integral, the inner surface integral must be evaluated. This must be done carefully since when the domains of the basis and the testing functions overlap, the kernel of the integral becomes singular at the observation point. Although this is an integrable singularity, a blindfolded usage of the numerical integration will result in inaccurate values. When the testing and basis subdomains are far from each other, i.e. the singularity of the Green's function does not fall in or near the integration domain, the inner integrals become very easy to integrate, hence a suitable low order quadrature may be employed.

For a fixed sample of the outer integral, the inner surface integral to be evaluated is of the form,

$$I(u_0, v_0) = \int \int_{\square, \Delta} du'dv' \frac{g(u', v')}{R(u', v')} \quad (\text{A.18})$$

where  $R(u', v')$  may become zero at a point  $(u_0, v_0)$  in the integration domain if the testing and basis subdomains overlap. The integral is not singular when the

two subdomains do not overlap and when a quadrature that does not sample the inner integral at the edges of its domain is used, but for subdomains that are close to each other the inner integral becomes quasi-singular meaning that it has a sharp variation in the integration region. The techniques presented in the next subsection will be employed for the annihilation of these singularities and quasi-singularities.

## A.2 Techniques to Annihilate the Singularity

The most common technique used for the numerical evaluation of the singular integrals is to add and subtract a term from the integrand which can be integrated analytically and also renders the integrals well behaved so that standard numerical integration methods can be applied [30, 30]. This technique works for problems involving flat discretizations of the geometry with the addition and subtraction of the well known  $1/R$  term from the integrand in,

$$I(u_0, v_0) = \int \int_{\square, \Delta} dudv \frac{g(u, v)}{R(u, v)}. \quad (\text{A.19})$$

For curved surfaces it is not possible to find such a function which will render the integrand well behaved and which is analytically integrable. One technique is to add and subtract a  $1/R_0$  term that approximates the actual  $1/R$  singularity [2]. This  $R_0$  term is found by using the Taylor series approximation of the curved subdomain around the observation point  $(u_0, v_0)$ . This technique was investigated and it was observed that the  $1/R_0$  eliminates the singularity at  $(u_0, v_0)$ , but the resulting integrand is not well behaved. It is not singular but it has sharp variations around the observation point. So the conclusion is that this technique is not suitable to use with a numerical integration procedure for

problems involving curved surfaces.

Using suitable parametric transformations on  $u$  and  $v$  parameters in Eq.( A.19), it is possible to annihilate the singularity [31]. Let the transformations be,

$$u = u(\eta, \zeta) \quad (\text{A.20})$$

$$v = v(\eta, \zeta). \quad (\text{A.21})$$

The integral on the  $(u, v)$  domain is thus transformed to,

$$\int \int dudvf(u, v) = \int \int d\eta d\zeta f(\eta, \zeta) J(\eta, \zeta) \quad (\text{A.22})$$

where

$$J(\eta, \zeta) = \begin{vmatrix} \frac{\partial u}{\partial \eta} & \frac{\partial u}{\partial \zeta} \\ \frac{\partial v}{\partial \eta} & \frac{\partial v}{\partial \zeta} \end{vmatrix} \quad (\text{A.23})$$

is the *Jacobian* of the transformation.

If one can find a transformation which has a zero at the singularity point of  $f(u, v)$  of the same or higher order as the zero of  $R(u, v)$ , the integrand of the transformed integral, namely  $f(\eta, \zeta)J(\eta, \zeta)$ , becomes non-singular in the integration domain with the condition thta the applied transformation does not increase the order of singularity of  $R(u, v)$ . Below are some transformations that can be used for this purpose.

### A.2.1 For Triangular Subdomains

A curved triangular patch in real space is the transformation of a (unit) triangle in the parametric space, seen in Fig A.1. The observation point  $\mathbf{r}_0$  on the

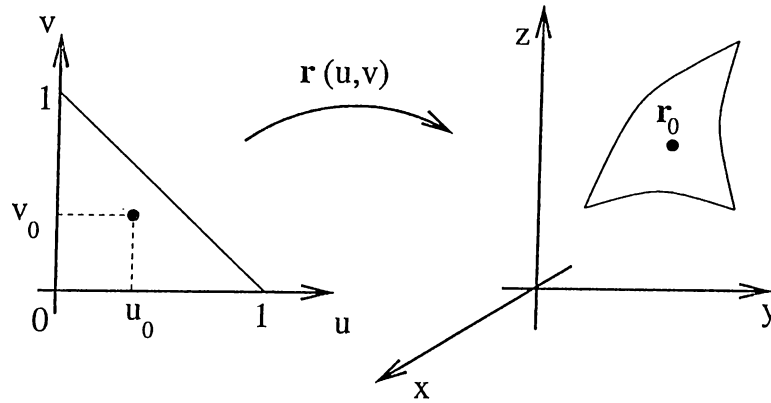


Figure A.1: Parametric mapping of the unit triangle to the curved triangle in real space.

surface and in the patch can be considered as the map of  $(u_0, v_0)$  point of the parametric domain triangle:  $\mathbf{r}_0 = \mathbf{r}(u_0, v_0)$ .

### Method I

Three sub-triangles are formed by connecting the observation point  $(u_0, v_0)$  to the three vertices of the triangle depicted in Fig A.2. For each sub-triangle the following parameter transformations are used:

$$\begin{bmatrix} u \\ v \end{bmatrix} = \eta \begin{bmatrix} u_{13} \\ v_{13} \end{bmatrix} + \zeta \begin{bmatrix} u_{23} \\ v_{23} \end{bmatrix} + \begin{bmatrix} u_3 \\ v_3 \end{bmatrix} \quad (\text{A.24})$$

where  $u_{ij} = u_i - u_j$  and  $i, j$  denote the vertex numbers of the sub-triangles (See Figs A.3– A.5). The transformation is different for each sub-triangle since the triangle vertices denoted by  $u_i$ 's are different but it is essential that vertex number 3 be chosen as the  $(u_0, v_0)$  point for each sub-triangle. The Jacobian of the above transformation mapping the unit triangle in  $(\eta, \zeta)$  domain to the

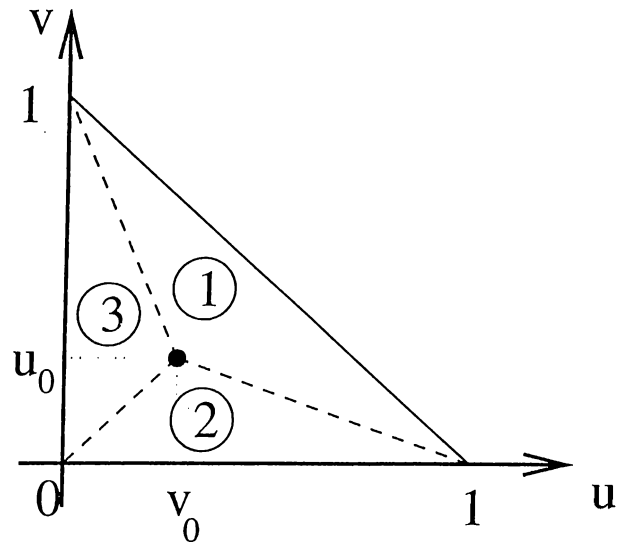


Figure A.2: Subdivision of the parametric unit triangle for singularity annihilation.

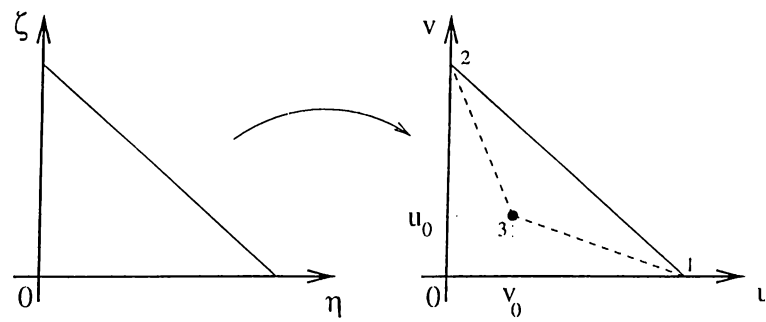


Figure A.3: Mapping of sub-triangle 1.

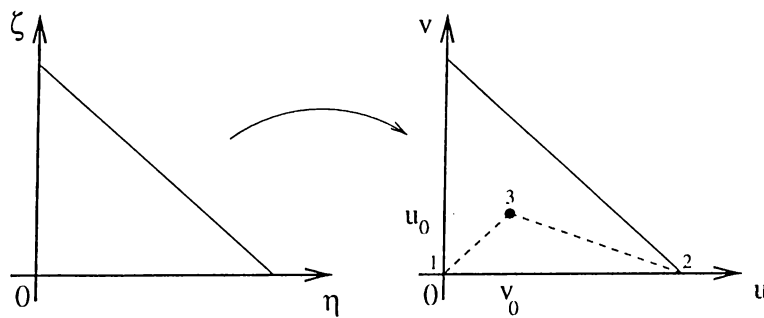


Figure A.4: Mapping of sub-triangle 2.



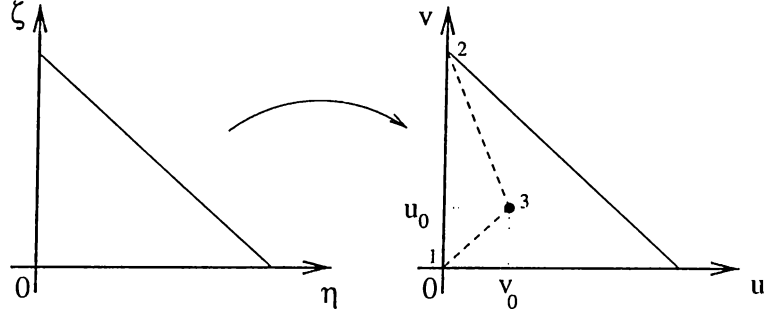


Figure A.5: Mapping of sub-triangle 3.

sub-triangle in  $(u, v)$  domain is,

$$J(u, v) = \begin{vmatrix} u_{13} & u_{23} \\ v_{13} & v_{23} \end{vmatrix} = u_{13}v_{23} - u_{23}v_{13}. \quad (\text{A.25})$$

The singularity point  $(u_0, v_0)$  is now at the third vertex of each sub-triangle, in other words, the origin of each of the three  $(\eta, \zeta)$  parametric domains is mapped into the singular point  $(u_0, v_0)$  in the  $(u, v)$  parametric space. The singular integral can be rewritten as,

$$\int_{\Delta} dudvf(u, v) = \int_{\Delta_1} dudvf(u, v) + \int_{\Delta_2} dudvf(u, v) + \int_{\Delta_3} dudvf(u, v) \quad (\text{A.26})$$

where,

$$\int_{\Delta_i} dudvf(u, v) = \int_{\Delta} d\eta d\zeta f_i(\eta, \zeta) J_i(\eta, \zeta). \quad (\text{A.27})$$

So,

$$\int_{\Delta} dudvf(u, v) = \int_{\Delta} d\eta d\zeta g(\eta, \zeta) \quad (\text{A.28})$$

where,

$$g(\eta, \zeta) = \sum_{i=1}^3 f_i(\eta, \zeta) J_i(\eta, \zeta). \quad (\text{A.29})$$

Here  $g(\eta, \zeta)$  is still singular in the  $(\eta, \zeta)$  parametric space but the singularity is at the origin regardless of the position of  $(u_0, v_0)$  in the  $(u, v)$  parametric

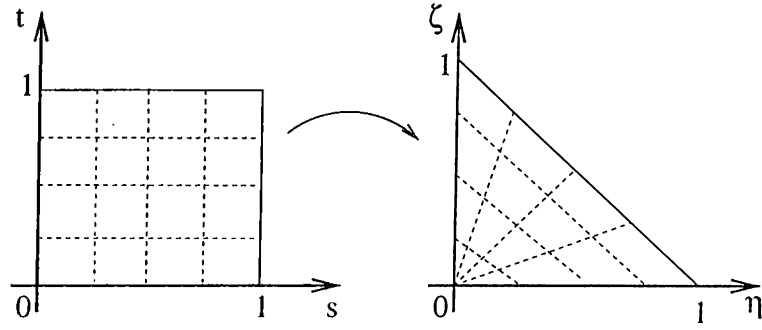


Figure A.6: Mapping defined to annihilate the singularity at the origin.

space. The transformation below annihilates the singularity at the origin, Fig. A.6 sketches the situation:

$$\eta = st \tag{A.30}$$

$$\zeta = s(1-t) \tag{A.31}$$

whose Jacobian is

$$J(s, t) = \begin{vmatrix} t & s \\ (1-t) & -s \end{vmatrix} = -st - s(1-t) = -s. \tag{A.32}$$

Since the origin of  $(\eta, \zeta)$  parametric domain is the map of  $s = 0$  line of  $(s, t)$  domain, the Jacobian has a zero at the origin of  $(\eta, \zeta)$  domain which cancels the singularity there. Hence the integral on  $(s, t)$  domain,

$$\int_{\Delta} dudv f(u, v) = \int_{\square} ds dt g(s, t) J(s, t) \tag{A.33}$$

which is now non-singular can be safely evaluated employing standart numerical integration techniques.

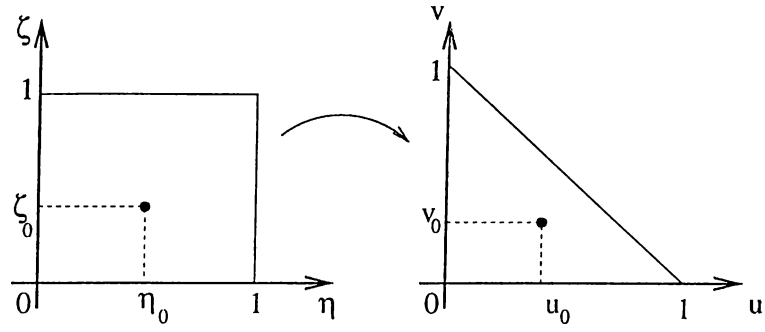


Figure A.7: Mapping of Method II.

## Method II

Using the last transformation of Method I at the beginning leads to the following situation:

$$u = \eta\zeta \quad (\text{A.34})$$

$$v = \eta(1 - \zeta) \quad (\text{A.35})$$

whose Jacobian is

$$J(\eta, \zeta) = -\zeta \quad (\text{A.36})$$

and the singular integral becomes

$$\int_{\Delta} dudv f(u, v) = \int_{\square} d\eta d\zeta f(\eta, \zeta) J(\eta, \zeta) \quad (\text{A.37})$$

$$= \int_{\square} d\eta d\zeta g(\eta, \zeta). \quad (\text{A.38})$$

But  $g(\eta, \zeta)$  is still singular at point  $(\eta_0, \zeta_0)$  of the  $(\eta, \zeta)$  domain. For the annihilation of this singularity as seen in Fig. A.7, one of the methods described for square subdomains below can be utilized.

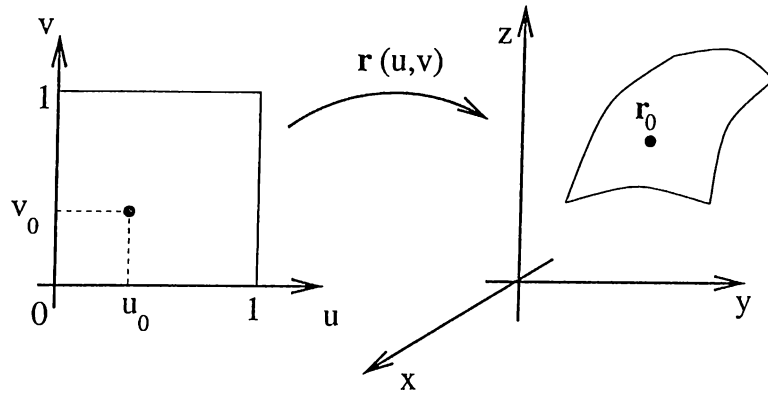


Figure A.8: Mapping of the parametric unit square to a curved rectangular patch.

### A.2.2 For Square Subdomains

A curved rectangular parametric patch in real space is the transformation of a (unit) square region in the parametric space as shown in Fig. A.8:

The observation point  $\mathbf{r}_0$  on the surface and in the patch can be considered as the map of  $(u_0, v_0)$  point of the parametric square region:  $\mathbf{r}_0 = \mathbf{r}(u_0, v_0)$ .

#### Method I

Method I for triangular domains can also be utilized for square subdomains. Four sub-triangles are formed by connecting the observation point  $(u_0, v_0)$  to the four vertices of the square as shown in Fig. A.9.

For each sub-triangle the same parameter transformations are used as in Method I for triangular subdomains.

$$\begin{bmatrix} u \\ v \end{bmatrix} = \eta \begin{bmatrix} u_{13} \\ v_{13} \end{bmatrix} + \zeta \begin{bmatrix} u_{23} \\ v_{23} \end{bmatrix} + \begin{bmatrix} u_3 \\ v_3 \end{bmatrix} \quad (\text{A.39})$$

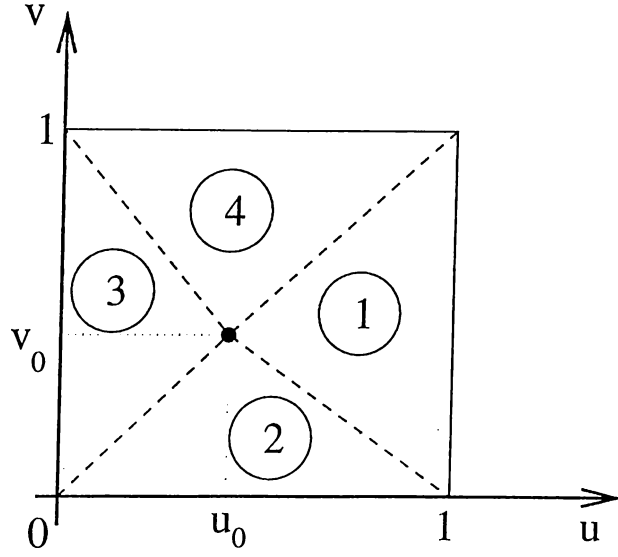


Figure A.9: Subdivision of the unit square into sub-triangles.

with Jacobian

$$J(u, v) = u_{13}v_{23} - u_{23}v_{13}. \quad (\text{A.40})$$

The singular integral is thus transformed into,

$$\int_{\square} dudvf(u, v) = \int_{\Delta} d\eta d\zeta g(\eta, \zeta) \quad (\text{A.41})$$

where

$$g(\eta, \zeta) = \sum_{i=1}^4 f_i(\eta, \zeta) J_i(\eta, \zeta). \quad (\text{A.42})$$

Method I for triangular subdomains is then applied to annihilate the singularity at the origin of the  $(\eta, \zeta)$  parametric space.

## Method II

In this method the parameters  $u$  and  $v$  are transformed separately, i.e.  $u = u(\eta)$  and  $v = v(\zeta)$ . The Jacobian of this transformation is,

$$J(s, t) = \frac{\partial u}{\partial s} \frac{\partial v}{\partial t}. \quad (\text{A.43})$$

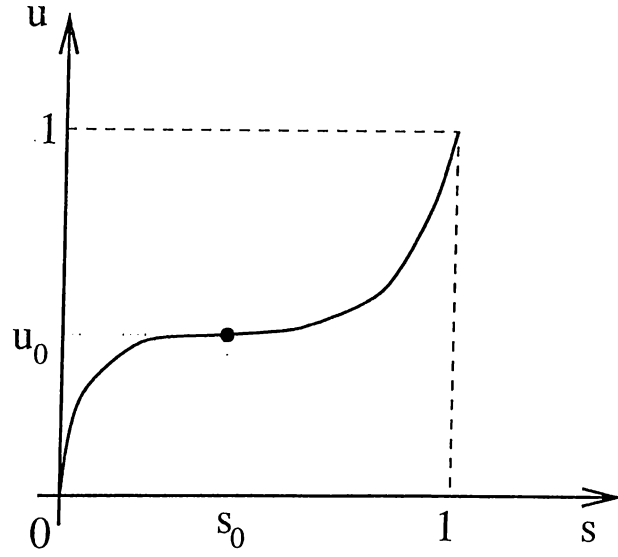


Figure A.10: Transformation applied on each parameter.

This Jacobian should have a zero at  $(u_0(s_0), v_0(t_0))$  to cancel the singularity there. This can be achieved by separately setting,

$$\left. \frac{\partial u}{\partial s} \right|_{s=s_0} = 0 \quad \text{and} \quad \left. \frac{\partial v}{\partial t} \right|_{t=t_0} = 0 \quad (\text{A.44})$$

Another constraint that may be imposed on the transformation is: The unit square in  $(s, t)$  domain should be mapped to the unit square in  $(u, v)$  domain.

A function  $u(s)$  satisfying the given constraints has the form in Fig A.10.

The lowest possible order polynomial satisfying the above criteria may be found to be of the form,

$$u(s) = \frac{(s - s_0)^3 + s_0^3}{(1 - s_0)^3 + s_0^3} \quad (\text{A.45})$$

with

$$\frac{\partial u}{\partial s} = \frac{3(s - s_0)^2}{(1 - s_0)^3 + s_0^3}, \quad (\text{A.46})$$

from which  $s_0$  can be found to be

$$u_0 = \frac{s_0^3}{(1-s_0)^3 + s_0^3} \Rightarrow s_0 = \frac{1}{1 + \sqrt[3]{\frac{1}{u_0} - 1}} \quad (\text{A.47})$$

A similar transformation is applied to the other parameter:

$$v(t) = \frac{(t-t_0)^3 + t_0^3}{(1-t_0)^3 + t_0^3} \quad (\text{A.48})$$

$$\frac{\partial v}{\partial t} = \frac{3(t-t_0)^2}{(1-t_0)^3 + t_0^3} \quad (\text{A.49})$$

$$v_0 = \frac{s_0^3}{(1-t_0)^3 + t_0^3} \Rightarrow t_0 = \frac{1}{1 + \sqrt[3]{\frac{1}{v_0} - 1}}. \quad (\text{A.50})$$

So the Jacobian of the transformation becomes,

$$J(s, t) = J_s(s)J_t(t) = \frac{9(s-s_0)^2(t-t_0)^2}{[(1-s_0)^3 + s_0^3][(1-t_0)^3 + t_0^3]} \quad (\text{A.51})$$

and the singular integral is transformed into a non-singular integral:

$$\int_{\square} dudvf(u, v) = \int_{\square} dsdtf(s, t)J(s, t). \quad (\text{A.52})$$

It is worth noting that due to the Jacobian factor, the integrand  $f(s, t)J(s, t)$  is zero on  $t = t_0$  and  $s = s_0$  lines in  $(s, t)$  domain, i.e. the Jacobian has a zero which is of higher order than the singularity of the original integrand.

### Method III

This method can be considered as the mixture of Method I and Method II. The integration domain (unit square) in  $(u, v)$  parameter space is first divided into four rectangular subdomains with the aid of  $u = u_0$  and  $v = v_0$  lines as depicted in Fig. A.11. Then, each subdomain is considered to be the mapping of the

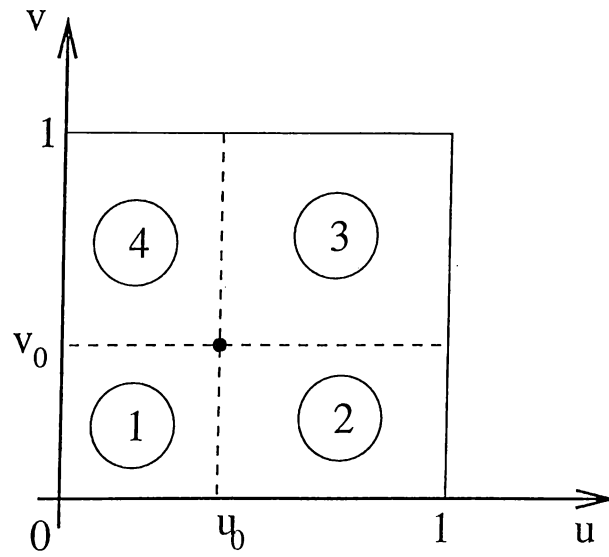


Figure A.11: The subdivision of the unit square for Method III.

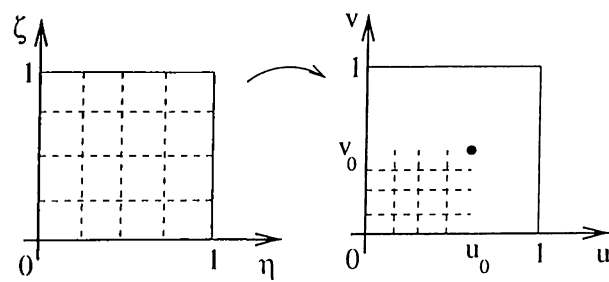


Figure A.12: The transformation for the first subdomain.



unit square in a  $(\eta, \zeta)$  parametric space. Figure A.12 depicts the situation for the first rectangular subdomain. The transformation and the Jacobian of the transformation for the first sub-rectangle are

$$\begin{aligned} u &= u_0(1 - \eta), \\ v &= v_0(1 - \zeta), \\ J_1(\eta, \zeta) &= u_0v_0, \end{aligned} \tag{A.53}$$

and for the other subdomain the transformations are

$$\begin{aligned} u &= (1 - u_0)\eta, \\ v &= v_0(1 - \zeta), \\ J_2(\eta, \zeta) &= (1 - u_0)v_0, \end{aligned} \tag{A.54}$$

$$\begin{aligned} u &= (1 - u_0)\eta, \\ v &= (1 - v_0)\zeta, \\ J_3(\eta, \zeta) &= (1 - u_0)(1 - v_0), \end{aligned} \tag{A.55}$$

$$\begin{aligned} u &= u_0(1 - \eta), \\ v &= (1 - v_0)\zeta, \\ J_4(\eta, \zeta) &= u_0(1 - v_0). \end{aligned} \tag{A.56}$$

After these transformations the singular integral appears as another singular integral in  $(\eta, \zeta)$  domain, but the singularity always appears at the origin.

At this step one can use the transformations described in Method II (Eqs.(A.45) and (A.48)) which simplify to,

$$\begin{aligned} \eta(s) &= s^3 \\ \zeta(t) &= t^3 \end{aligned}$$

$$\begin{aligned}
J(s) &= 3s^2 \\
J(t) &= 3t^2.
\end{aligned}
\tag{A.57}$$

or the degree of this transformation can be lowered,

$$\begin{aligned}
\eta(s) &= s^2 \\
\zeta(t) &= t^2 \\
J(s) &= 2s \\
J(t) &= 2t.
\end{aligned}
\tag{A.58}$$

This leads to a non-singular integrand. However, for numerical integration purposes the cubic transformation was observed to perform better than the quadratic transformation. One can also increase the order of these transformations but numerical instabilities should be expected for large orders.

#### Method IV

This method is another variation of Method III. The first transformation is exactly the same as in Method III. i.e. the four subdomains are mapped to a single square in  $(\eta, \zeta)$  space. This square domain is divided into two triangular subdomains by the  $\eta = \zeta$  line as shown in Fig. A.13. Each triangular subdomain can be considered as the map of a unit triangle on  $(\alpha, \beta)$  parametric domain defined by the transformations of Method I for triangular subdomains:

$$\begin{bmatrix} \eta \\ \zeta \end{bmatrix} = \alpha \begin{bmatrix} \eta_{13} \\ \zeta_{13} \end{bmatrix} + \beta \begin{bmatrix} \eta_{23} \\ \zeta_{23} \end{bmatrix} + \begin{bmatrix} \eta_3 \\ \zeta_3 \end{bmatrix}
\tag{A.59}$$

with Jacobian

$$J(\alpha, \beta) = \eta_{13}\zeta_{23} - \eta_{23}\zeta_{13}.
\tag{A.60}$$

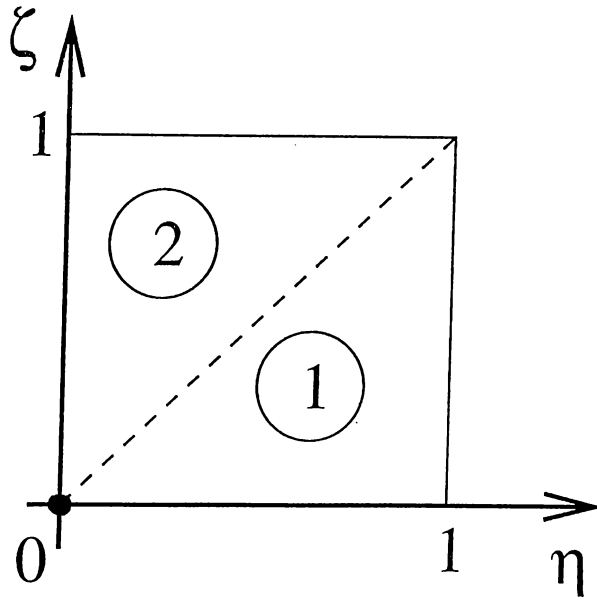


Figure A.13: The subdivision of the unit square for Method IV.

So the singular integral whose singularity is at the origin of the  $(\eta, \zeta)$  parameter space becomes,

$$\int_{\square} d\eta d\zeta g(\eta, \zeta) = \int_{\Delta} d\alpha d\beta \sum_{i=1}^2 g_i(\alpha, \beta) J_i(\alpha, \beta). \quad (\text{A.61})$$

Then using the same procedure of Method I for triangular subdomains, this singular integrand in the  $(\alpha, \beta)$  parameter space is transformed into a non-singular integrand in  $(s, t)$  parameter space. The transformation is,

$$\alpha = st \quad (\text{A.62})$$

$$\beta = s(1-t), \quad (\text{A.63})$$

with the Jacobian  $J(\alpha, \beta) = -s$ .

Other variations of the techniques to annihilate the singularity of the Green's function for integral evaluations on curved subdomains are also possible. Our experience with all of the above techniques resulted in our conclusion that for triangular subdomains Method I performs best and for square (can be

generalized for rectangular subdomains) subdomains, Method I performs best on the basis of numerical integration.

### A.3 Numerical Integration

For the evaluation of both the testing and the basis integrals on the associated subdomains 2-dimensional Gaussian quadrature (GQ) was used. An adaptive  $N$ -point Cartesian product GQ was implemented. Techniques to annihilate the singularity in the inner integral presented in the previous subsection produce non-singular integrands but these integrands are still not suitable for integration with an adaptive quadrature routine. They may have sharp variations for positions of the observation point near the edges of the basis subdomain when Method I of both triangular and square subdomains are used. The other methods also produce sharply varying integrands. Another disadvantage of adaptive quadrature is that the evaluated values of the integrand that does not satisfy the given error criteria are discarded, which results in loss of time. The adaptive quadrature implemented was observed to take impractically long time due to the sharp changes in the integrand. For those reasons, fixed point GQ was used for the evaluation of the matrix elements. The number of points to be used is input to the routine by an external file which provides user control on the process.

## REFERENCES

- [1] S. M. Rao, D. R. Wilton, and A. W. Glisson, "Electromagnetic scattering by surfaces of arbitrary shape," *IEEE Trans. on Antennas and Propagation*, vol. AP-30, pp. 409–418, May 1982.
- [2] J. M. Song and W. C. Chew, "Moment method solution using parametric geometry," *Journal of Electromagnetic Waves and Applications*, vol. 9, pp. 71–83, 1995.
- [3] W. A. Glisson and D. R. Wilton, "Simple and efficient numerical methods for problems of electromagnetic radiation and scattering from surfaces," *IEEE Trans. on Antennas and Propagation*, vol. AP-28, pp. 593–603, September 1980.
- [4] S. Wandzura, "Electric current basis functions for curved surfaces," *Electromagnetics*, vol. 12, pp. 77–91, 1992.
- [5] V. Rokhlin, "Rapid solution of integral equations of scattering theory in two dimensions," *Journal of Computational Physics*, vol. 1986, pp. 414–439, 1990.
- [6] N. Engheta, W. D. Murphy, V. Rokhlin, and M. S. Vassiliou, "The fast multipole method (FMM) for electromagnetic scattering problems," *IEEE Trans. on Antennas and Propagation*, vol. 40, pp. 634–641, June 1992.

- [7] R. Coifman, V. Rokhlin, and S. Wandzura, "The fast multipole method for the wave equation: A pedestrian prescription," *IEEE Antennas and Propagation Magazine*, vol. 35, pp. 7–12, June 1993.
- [8] R. F. Harrington, *Field Computation by Moment Methods*. Macmillan, 1968.
- [9] L. Gürel, K. Sertel, and İ. K. Şendur, "On the choice of basis functions to model surface electric current densities in computational electromagnetics," submitted to *IEEE Trans. Antennas and Propagat.*, June 1997.
- [10] J. M. Song and W. C. Chew, "Fast multipole method solution using parametric geometry," *Microwave and Optical Technology Letters*, vol. 7, pp. 760–765, November 1994.
- [11] M. Abramowitz and I. A. Stegun, *Handbook of Mathematical Functions*. National Bureau of Standards, 1972.
- [12] J. M. Song and W. C. Chew, "Fast multipole method solution of combined field integral equations," *ACES Conference Digest*, March 1995.
- [13] R. L. Wagner and C. W. Chew, "A ray-propagation fast multipole algorithm," *Microwave and Optical Technology Letters*, vol. 7, pp. 435–438, July 1994.
- [14] R. J. Burkholder and D. Kwon, "High-frequency asymptotic acceleration of the fast multipole method," *Radio Science*, vol. 31, pp. 1199–1206, September-October 1996.
- [15] C. Lu and W. C. Chew, "Fast far-field approximation for calculating the res of large objects," *Microwave and Optical Technology Letters*, vol. 8, pp. 238–241, April 1995.

- [16] D. F. Rogers and J. A. Adams, *Mathematical Elements for Computer Graphics*, McGraw Hill, 1989.
- [17] G. Farin, *Curves and Surfaces for Computer Aided Geometric Design*. Academic Press, 1990.
- [18] K. S. Kunz and R. J. Luebbers, *The Finite-Difference Time-Domain Method for Electrodynamics*. CRC Press, 1993.
- [19] S. M. Rao, T. K. Sarkar, P. Midya and A. R. Djordević, “Electromagnetic radiation and scattering from finite conducting and dielectric structures: Surface/surface formulation,” *IEEE Trans. on Antennas and Propagation*, vol. 39, pp. 1034–1037, July 1991.
- [20] T. Horng, W. E. McKinzie and G. Alexopoulos, “Full-wave spectral-domain analysis of compensation of microstrip discontinuities using triangular subdomain basis functions.” *IEEE Trans. on Microwave Theory and Techniques*, vol. 40, pp. 2137–2147, December 1992.
- [21] U. Jacobus and F. M. Landstorfer, “Novel basis function for the equivalent magnetic current in the method of moments solution of the dielectric scattering problems,” *Electronics Letters*, vol. 29, pp. 1272–1273, July 1993.
- [22] J. Sercu, N. Fache, and P. Lagasse, “First-order rooftop functions for the current discretization in the method of moments solution of planar structures,” *IEEE Trans. Antennas Propagat. Soc. Int. Symp.*, pp. 2170–2173, June 1994.
- [23] K. R. Aberegg, A. Taguchi, and A. F. Peterson, “Application of higher-order vector basis functions of surface integral equation formulations,”

*Radio Science*, vol. 31, pp. 1207–1213, September-October 1996.

- [24] A. F. Peterson and K. R. Aberegg, “Parametric mapping of vector basis functions for the surface integral equation formulations,” *Appl. Comp. Electromagn. Soc. J.*, vol. 10, pp. 107–115, 1995.
- [25] L. Gürel, İ. K. Şendur, and K. Sertel, “Quantitative comparison of rooftop and RWG basis functions,” *IEEE AP-S Conference Digest*, July 1997.
- [26] C. A. Balanis, *Advanced Engineering Electromagnetics*. Wiley, 1989.
- [27] B. D. Popović and B. M. Kolundžija, *Analysis of Metallic Antennas and Scatterers*. IEE Electromagnetic Wave Series 38, 1994.
- [28] J. Ma, V. Rokhlin, and S. Wandzura, “Generalized Gaussian quadrature rules for systems of arbitrary functions,” *Research Report YALEU/DCS/RR-990*, October 1993.
- [29] S. Kapur and V. Rokhlin, “High-order corrected trapezoidal rules for singular functions,” *Research Report YALEU/DCS/RR-1042*, August 1994.
- [30] D. R. Wilton, S. M. Rao, A. W. Glisson, D. H. Schaubert, O. M. Al-Bundak, and C. M. Butler, “Potential integrals of uniform and linear source distributions on polygonal and polyhedral domains,” *IEEE Trans. on Antennas and Propagation*, vol. AP-32, pp. 276–281, March 1984.
- [31] R. D. Graglia, “On the numerical integration of the linear shape functions times the 3-d green’s function or its gradient on a plane triangle.” *IEEE Trans. on Antennas and Propagation*, vol. 41, pp. 1448–1455, October 1993.